Doctoral Thesis

TWO-DIMENSIONAL CARBON-BASED LAYERED MATERIALS: SYNTHESIS AND MODIFICATION

Jeong-Min Seo

Department of Energy Engineering

Graduate School of UNIST

2018

TWO-DIMENSIONAL CARBON-BASED LAYERED MATERIALS: SYNTHESIS AND MODIFICATION

Jeong-Min Seo

Department of Energy Engineering

Graduate School of UNIST

TWO-DIMENSIONAL CARBON-BASED LAYERED MATERIALS: SYNTHESIS AND MODIFICATION

A thesis
submitted to the Graduate School of UNIST
in partial fulfillment of the
requirements for the degree of
Doctor of Philosophy

Jeong-Min Seo

01. 08. 2018 of submission

Approved by

Advisor
Jong-Beom Baek

TWO-DIMENSIONAL CARBON-BASED LAYERED MATERIALS: SYNTHESIS AND MODIFICATION

Jeong-Min Seo

This certifies that the thesis of Jeong-Min Seo is approved.

01. 08. 2018 of submission

signature

Advisor: Jong-Beom Baek

signature

Myoung Soo Lah: Thesis Committee Member #1

signature

Noejung Park: Thesis Committee Member #2

signature

Jung-Woo Yoo: Thesis Committee Member #3

signature

Hu Young Jeong: Thesis Committee Member #4;

Abstract

The synthetic modification of two-dimensional (2D) layered materials as well as its chemical production represents an attractive challenge which is driven by their potential applications. Synthetic modification can tailor the physical and chemical properties by introducing or changing the functionality into the materials, hence improve their processability and performance of practical applications. The development of chemical modification for 2D layered materials has generally lagged way behind compared with other 1D and 3D analogues. Therefore, synthetic modification of 2D layered materials can be considered as a challenge for synthetic chemists.

The focus of the thesis is on the synthesis and modification of 2D layered materials, which allow to enhance processability for practical applications. Before discussing my Ph.D. studies, I give a brief overview of progress on the development of 2D layered materials. Studies of this thesis is mainly divided into two kinds of materials; graphene and covalent organic framework (COF). In the first half of this thesis, I discuss postsynthetic modification of graphite into graphene nanoplatelets *via* solvent-free Diels-Alder reaction. The one-pot Diels-Alder reaction of pristine graphite enables to functionalize dienophiles at the edge of graphite, which facilitate to delaminate into graphene nanoplatelets by dispersing them into common organic solvent. The second half of this thesis focuses on synthesis and presynthetic modification of COFs. Firstly, I describe the presynthetic modification of imine-linked COF with high crystallinity and porosity. To improve the reactivity of COF, I designed small-pore crystalline COF using specific triamine building block including hydroxy groups. The resultant imine-linked COF showed high crystallinity and microporosity, and it exhibited high thermal stability. Secondly, I explore synthesis of imide-linked COF. Because of the irreversible second step imidization, the imide-linked COF shows high thermal and chemical stability along with the 1D polyimide analogues. The last part of this thesis, I briefly summarize my Ph.D. studies.

Contents

List of figures

constant flow of nitrogen.

Figure 5.5 | PXRD pattern of imide-linked COF. a, Experimental (black line), Pawley-refined PXRD pattern (orange line), Bragg position (green dot), the difference plot (olive line), simulated with the AA-staking model (red line) and AB-stacking model (blue line). **b**, Simulated unit cell structure of the AA-stacking mode (C, grey; N, blue; O, red; S, yellow; H, white). **c**, Simulated unit cell structure of the AB-stacking mode (C, grey; N, blue; O, red; S, yellow; H, white; cyan, a further layer).

Figure 5.6 | Porosity of imide-linked COF. a, Nitrogen sorption isotherms of TBT-PMDA-COF. Solid and open circles represent the adsorption and desorption branches, respectively. Inset is corresponding pore size distribution of TBT-PMDA-COF from fitting the NLDFT model to the adsorption data. **b**, Simulated BET surface area plot of TBT-PMDA-COF at 77 K using nitrogen as adsorbate. **c**, Nitrogen isotherm measured at 77 K used for NLDFT modeling and pore size distribution calculations. The calculated NLDFT isotherm (cylindrical pore model) is overlaid as open square and fitting error indicated.

Figure 5.7 | Chemical stability of imide-linked COF. a,**b**, (**a**) PXRD patterns and (**b**) Full IR spectra showing retention of crystallinity of TBT-PMDA-COF after treatment for 24 h in different chemical conditions.

List of schemes

List of tables

Nomenclature

2D	Two-dimensional
TMDs	Transition metal dichalcogenides
***h*-BN**	Hexagonal boron nitrides
3D	Three-dimensional
COFs	Covalent organic frameworks
CVD	Chemical vapor deposition
TMOs	Transition metal oxides
1D	One-dimensional
AFM	Atomic force microscopy
GO	Graphene oxide
rGO	Reduced graphene oxide
g-C_3N_4	Graphitic carbon nitrides
SLG	Single layer graphene
ME	Mechanical exfoliation
LPE	Liquid-phase exfoliation
NMP	*N*-methyl-pyrrolidone
GIC	Graphite intercalation compound
H_2SO_4	Sulfuric acid
$KMnO_4$	Potassium permanganate
Mn_2O_7	Dimanganese heptoxide
***R*s**	Sheet resistance
$(NH_4)_2MoS_4$	Ammonium thiomolybdates
CPs	Coordination polymers
GIWAXS	Grazing-incidence wide-angle X-ray scattering
TCNE	Tetracyanoethylene
MA	Maleic anhydride
CNTs	Carbon nanotubes
MI	Maleimide
EFGnPs	Edge-selectively functionalized graphene nanoplatelets
THF	Tetrahydrofuran
KBr	Potassium bromide
TGA	Thermogravimetric analysis

FT-IR	Fourier transform infrared
FE-SEM	Field-emission scanning electron microscopy
EA	Elemental analysis
XPS	X-ray photoelectron spectra
MA-GnPs	MA-functionalized graphene nanoplatelets
MI-GnPs	MI-functionalized graphene nanoplatelets
EDS	Energy dispersive spectrometer
DMF	Dimethylformamide
HR-TEM	High-resolution transmission electron microscopy
MAG	Maleic anhydride-functionalized graphene nanosheets
MIG	Maleimide-functionalized graphene nanosheets
TATHB	1,3,5-triamino-2,4,6-benzenetriol
TPA	Terephthaldehyde
BET	Brunauer-Emmett-Teller
NLDFT	Nonlocal density functional theory
PXRD	Powder X-ray diffraction
ODCB	1,2-dichlorobenzene
K_2CO_3	Potassium carbonate
TBT	2,5,8-triaminobenzo[1,2-d:3,4-d':5,6-d'']tris(thiazole)
PMDA	Pyromellitic dianhydride

Chapter 1 INTRODUCTION

Two-dimensional (2D) layered materials refer to a class of materials that possess sheet-like structures, in which the atoms are connected by covalent or ionic bonds along 2D (in-plane) directions to form atomically thin layers, while the layers are bonded together by weak van der Waals interactions along the three-dimensional (out-of-plane) direction. Such weak van der Waals interactions between adjacent layers make it possible to cleave the layered materials into individual few- or single- layers *via* micromechanical cleavage or liquid phase exfoliation methods. While these layered structures can exist in nature in the form of graphite or molybdenum disulfide, atomically thin 2D materials thought not to exist. Indeed, it was long believed that atomically thin 2D materials were thermodynamically unstable at any finite temperature, since thermal lattice fluctuations would be as large as the force binding the atoms together, causing the structure to fall apart.[2,3] The original discoveries in 2004 has shown that the existence of graphene in room temperature, hence booming a considerable number of studies. Graphene is the firstly reported 2D materials that has plenty of unprecedented electronic, physical, optical and thermal properties. For these reasons it holes potential to impact future emerging technologies. However, graphene itself possesses zero band gap, which is undesirable for high performance semiconductors that require bandgap.[3] That limitation inspired us to explore other 2D layered materials that possess versatile properties *via* micromechanical cleavage technique, such as transition metal dichalcogenides (TMDs), hexagonal boron nitrides (*h*-BN). Similar to graphene, these one atom thick materials exhibit a wide range of unique electrical, optical and mechanical properties that can never be seen in their three-dimensional (3D) bulk counterparts due to the dimensionality confinement effect.[1] Promising research on 2D layered materials further enriched the exploration of 2D family members composed of organic materials, such as covalent organic frameworks (COFs) and polymer derivatives.[4,5] (Figure 1.1)

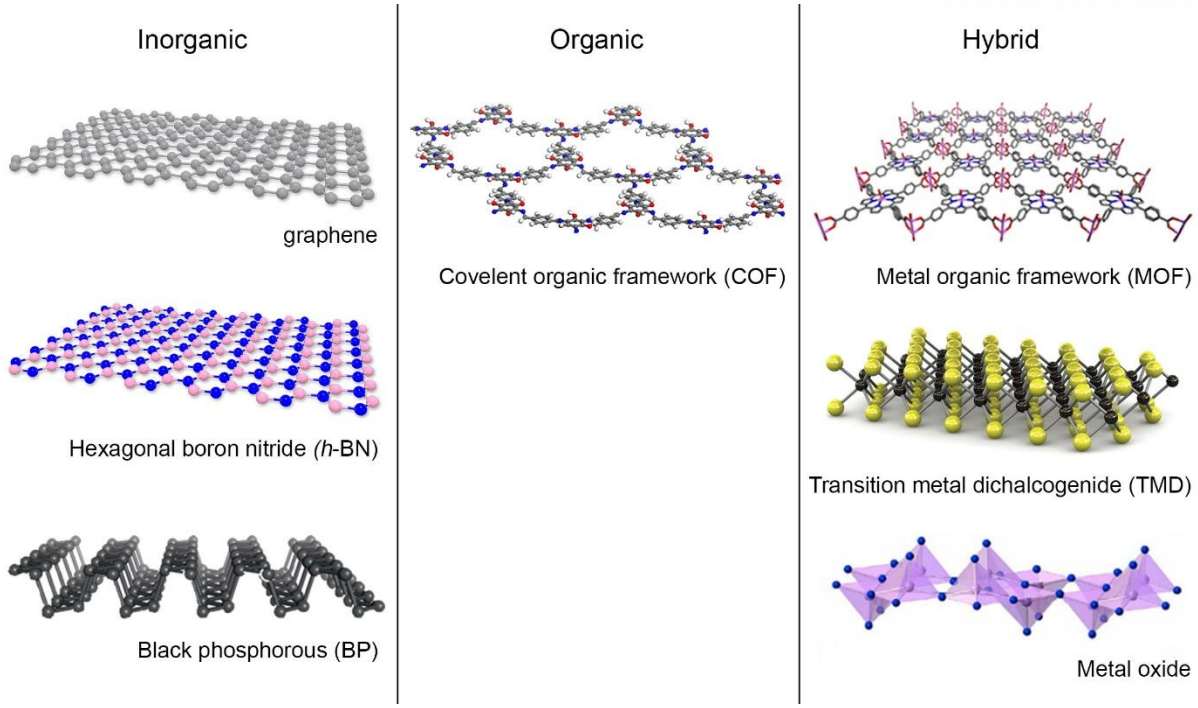

Figure 1.1 | Structure of two-dimensional (2D) layered materials. Selected examples for diverse assembly of building blocks for construction of 2D layered materials ranging from the inorganic, organic and hybrid chemical architectures. Reproduced with permission from ref.[4] Copyright 2013 The Royal Society of Chemistry

The unique properties of 2D layered materials strongly rely on their composition and number of layers due to the quantum confinement effects in the out-of-plane direction.[1] For example, the band structure of graphene changes with the number of layers as well as their stacking sequence. That phenomenon greatly stimulates the development of new synthetic routes to prepare 2D layered materials. So far, various methods such as the micromechanical cleavage, liquid-phase exfoliation, chemical vapor deposition (CVD) and wet-chemical syntheses have been reported and all the methods are categorized into two main strategies. One is top-down approaches, including exfoliation of layered bulk structures into individual 2D materials. Another is bottom-up approaches, based on chemical reaction of properly designed molecular building blocks to form 2D covalent network.[5,6] These well-known techniques have allowed the field of 2D layered materials to grow rapidly. The properties and quality of materials depend on the synthetic methods, which have a decisive effect on the performance of applications that can utilize it. Therefore, it is crucial to understand comprehensive study of synthetic methods to prepare high quality of 2D layered materials with large quantities. Given their unique structural and outstanding properties as well as promising applications, 2D layered materials have now became one of the hottest research topics in condensed matter physics, material science, chemistry, and nanotechnology.[5,7] In this chapter, I give an overview for development of various 2D layered materials *via* different synthetic methods and modification of these materials for potential applications. I briefly start to highlight the

unique advantage of 2D layered materials. After that I summarize the types of 2D layered materials which related to my Ph.D. studies. Typical synthetic methods for preparation of 2D layered materials are then discussed in detail. Further, I introduce synthetic modification of 2D layered materials, which point out postsynthetic modification related to my Ph.D. studies. Finally, I provide a research overview and objective of this thesis.

1.1 Family of 2D layered materials

1.1.1 Introduction of 2D layered materials

To date, new types of 2D layered materials have been explored in recent years, enriching the family of 2D layered materials. Even though the composition and crystal structures of 2D layered materials are different from each other, they all can be categorized into two forms: layered crystals and monolayer materials. For layered materials, the in-plane atoms or molecules are connected by periodic bonding in two orthogonal directions, while these layers are stacked together through the weak van der Waals interaction to form bulk crystals. Graphite is a typical example of layered crystals in which graphene layers are weakly stacked together, forming the bulk graphite crystal. In addition to graphite, many other layered crystals are introduced, such as *h*-BN, TMDs, g-C_3N_4 and transition metal oxides (TMOs).[8] Their weak bonding nature give them to be delaminated into 2D nanosheets *via* top-down approaches, such as micromechanical cleavage and liquid-phase exfoliation. In addition, other 2D layered materials can crystallize into layered structure *via* atomic or chemical bonding, especially for metal oxides, metal chalcogenides, and polymers.[9,10] In this section, I mainly introduce the carbon-based 2D layered materials based on the composition and crystal phase in detail.

1.1.2 Graphene

Graphene is one of the most famous two-dimensional carbon allotropes. It is composed of single-atom-thick sheet of sp^2-hybridized carbon atoms arrayed in a honeycomb patterns.[11] The fully conjugated π-electron systems in graphene can be considered as the basic building block of other allotropes.[12] (Figure 1.2) The hexagonally arranged carbon network give rise to some extraordinary thermal, mechanical, and electronic properties, which have influenced on exploring many other 2D materials.

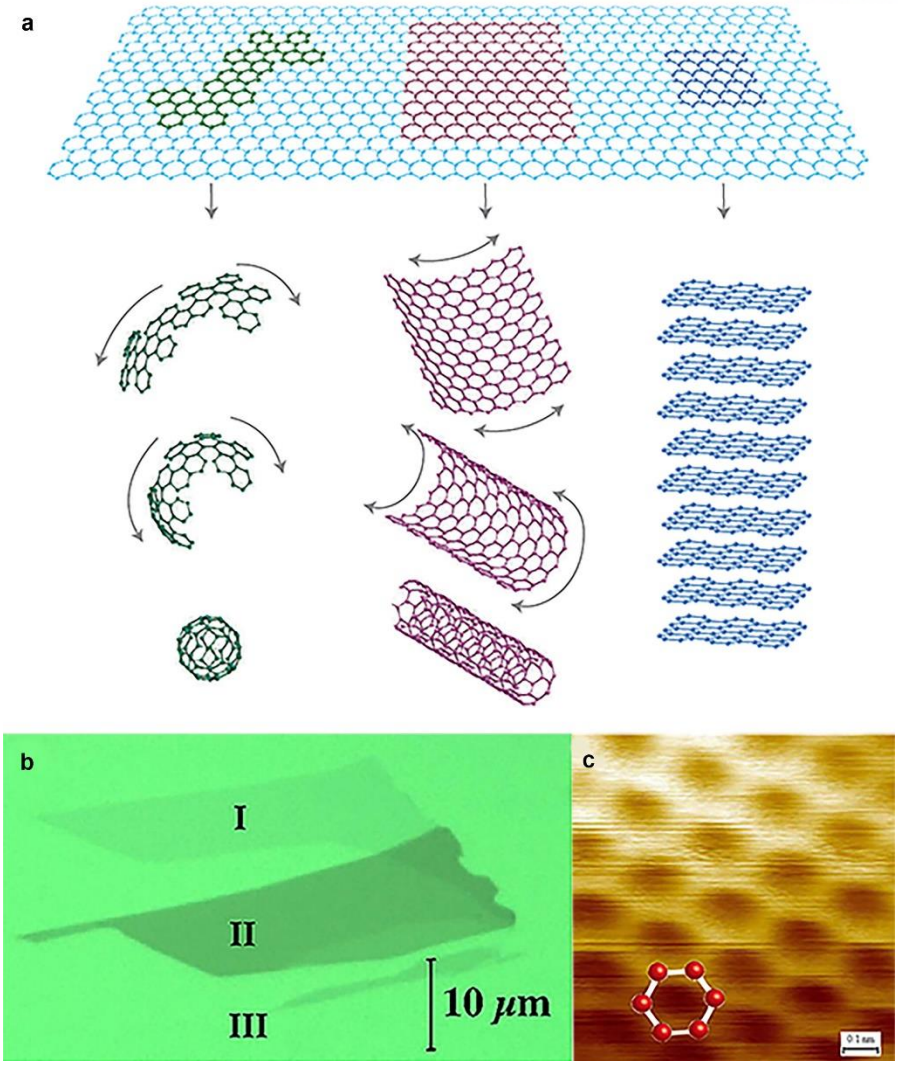

Figure 1.2 | **Mother of all graphitic forms**. **a**, Graphene is a 2D building block for carbon materials of all other dimensionalities. It can be wrapped up into 0D buckyballs, rolled into 1D nanotubes or stacked into 3D graphite. Reproduced with permission from ref.[3] Copyright 2007 Nature Publishing Group. **b**, Optical microscopy images of the sample before deposition of the electrode. Three regions with different optical densities can be identified: I, single-layer graphene; II, multilayer graphene; and III, the silicon-dioxide-coated substrate. **c**, STM topographic images from a single layer of graphene (region I of Figure 1.2b). Reproduced with permission from ref.[13] Copyright 2007 The National Academy of Sciences of the USA

Studies for exfoliation of layered compound to produce thin materials have been conducted by several groups. They have tried to exfoliate graphite by using an atomic force microscopy (AFM) tip, which possess at least 30 layers of graphite.[11] While these elegant methods produced 2D layered materials, Geim and co-workers firstly isolate graphene from graphite in 2004 by using Scotch tape, currently classified as the mechanochemical cleavage method.[14] This led to an explosion of interest especially in physics, because two-dimensional crystals were thought to be thermodynamically unstable

at finite temperatures.[2,3] The experimental isolation of single-layer graphene enabled us to observe some unique properties including ambipolar field effect, the quantum Hall effect at room temperature and extremely high carrier mobility (~200,000 $cm^2V^{-1}s^{-1}$). Graphene also exhibits other superior mechanical, optical, and thermal properties, such as high Young's modulus (~1 TPa), large specific surface area (2630 m^2g^{-1}), high transparency (~97.7%), and high thermal conductivity (above 3,000 W $m^{-1}K^{-1}$).[15] These unprecedented properties make graphene a promising candidate for a large variety of potential applications including electronics/optoelectronics (high-frequency transistors, solar cells, light-emitting devices, transparent electronics, photodetectors), energy-related devices (capacitors, fuel cells, batteries), catalysis, sensors and biomedical applications.[16] The market of graphene applications has required for progress in mass production of graphene with high quality for the specific application. Currently, a variety of synthetic methods have been developed to prepare graphene with various dimensions, shapes and quality. The commonly applied methods include the micromechanical exfoliation of graphite, liquid-phase exfoliation of graphite, chemical vapor deposition (CVD) growth, and chemical or thermal reduction of graphene oxide (GO).[17] Each production methods strongly affects the quality of graphene. For example, reduced graphene oxide (rGO) made by thermal or chemical reduction of GO has some hole defects and a minor number of functional groups. Therefore, it is suitable for use in composite materials, conductive paints.[18] Despite having outstanding properties for potential applications, it is worth mentioning that graphene itself possesses zero band gap as well as chemical inertness, which limits its applicability in the field of semiconductors. Covalent modification of graphene can address this issue. However, the process is highly aggressive and have resulted in uncontrollable functionalization that lower the intrinsic properties.[19] This quandary has led many researchers to explore other 2D materials possess similar layered structure such as TMDs, graphitic carbon nitrides (g-C_3N_4) and so on.

1.1.3 Covalent organic frameworks (COF) and 2D polymer

COFs are a class of 2D polymer that are obtained as microcrystalline powders whose backbone is composed of light elements, such as B, C, N, O. COFs are made by combination of molecular building blocks covalently linked into extended structures, based on reticular chemistry.[20]

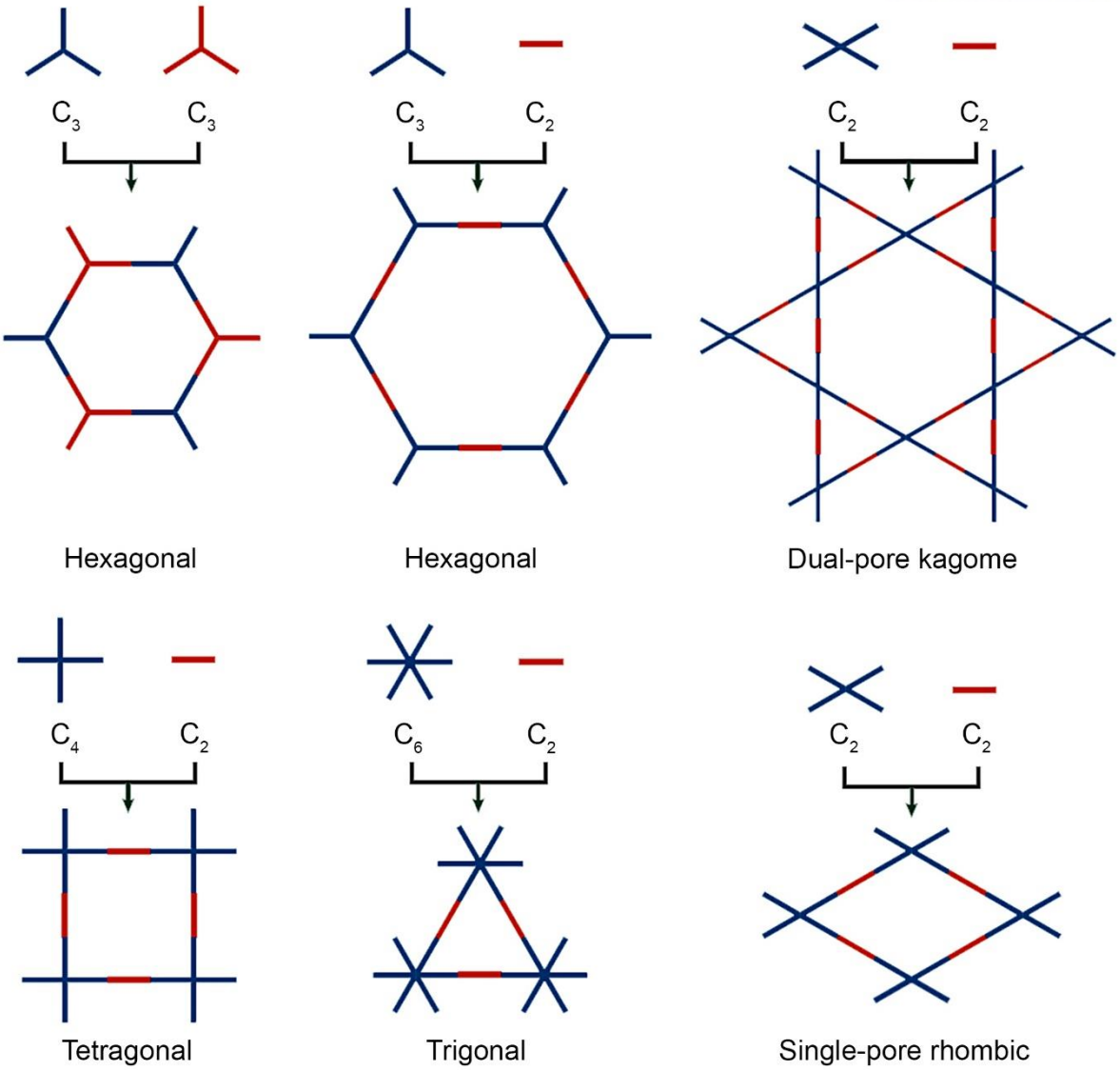

Figure 1.3 | **Topology diagrams for designing 2D COFs**. Topology diagrams represent the polygon skeletons of covalent organic frameworks (COFs), which can be realized by assembling rigid building blocks as vertices and edges. The COF shapes that have been developed thus far include hexagonal, tetragonal, rhombic, kagome and trigonal structures, and the building blocks can be classified as C_2-, C_3-, C_4- and C_6-symmetric units based on the directional symmetry of the reactive groups. Reproduced with permission from ref.[21] Copyright 2016 Nature Publishing Group.

One distinct feature of COFs is that a variety of topology is determined by the symmetry of molecular building blocks (Figure 1.3). For example, the combination of C_3-symmetric knots and C_2-symmetric linkers (C_3 + C_2) leads to the formation of hexagonal COFs, which is the typical topology of the 2D COFs. Given a few examples of the topological diagram described by Figure 1.3, various types of COFs with desired pores and shapes can be designed.[21] Generally, the polymeric materials can be readily synthesized by the linkage of the molecular building blocks with covalent bond. However, the formation

of these materials is dominated by kinetically controlled reaction, yielded disordered materials. In order to achieve an ordered structure, the connection of molecular building blocks should be progressed under thermodynamic controlled reaction, which known as dynamic covalent chemistry (DCC). DCC involves reversible bonding processes that the formation of products is in continuous equilibrium with "error-checking" and "proof-reading" characteristics. This process allows to form the most thermodynamically stable structures. Consequently, crystalline COFs would finally be produced with high thermodynamic stability.[22,23]

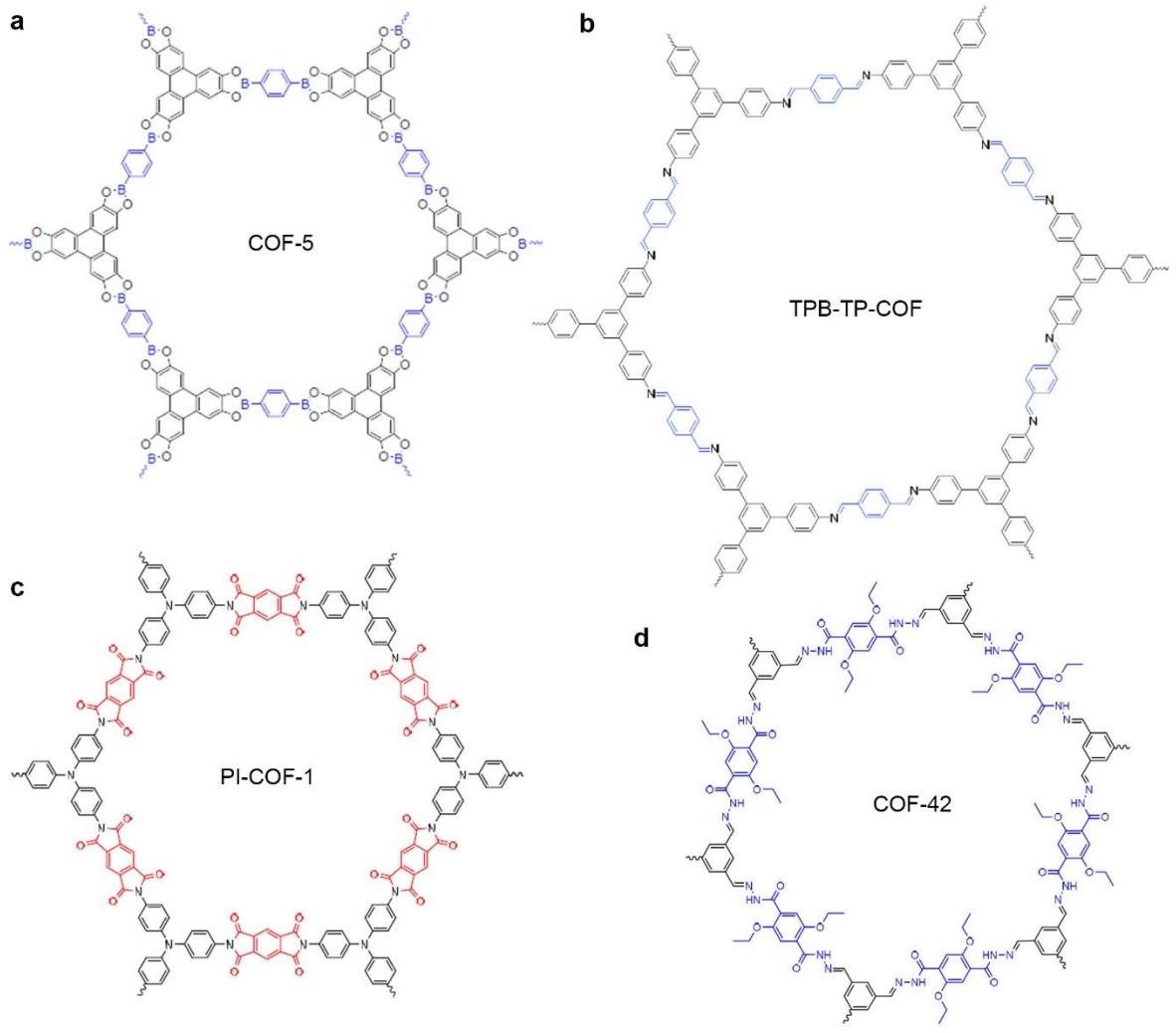

Figure 1.4 | Chemical structure of classic COFs. **a-d**, Schematic representation of COFs with different linkages: (**a**) Boron-containing COF (COF-5). (**b**) Imine-linked COFs (TPB-TP-COF). (**c**) Imide-linked COF (PI-COF-1). (**d**) Hydrazone-linked COF (COF-42).

The pioneering first work on COFs was reported in 2005 by the Yaghi group. The earliest documented COFs were synthesized by the self-condensation of boronic acids to produce boroxine anhydride-based linkages in the form of B_3O_3 rings and formation of boronate esters.[24] Apart from the aforementioned

boron-comprising COFs, other COFs, such as imine-linked COFs, hydrazone-linked COFs and imide-linked COFs were also reported in the past few years.[25](Figure 1.4) 2D COFs normally crystallize into randomly oriented, microcrystalline and layered structure. The organic units are linked into 2D atomic layers by covalent bond to form a single-layer COF nanosheets. Individual layers stack *via* π–π interactions to crystallize layered structures with periodically aligned channels parallel to the stacking direction. Therefore, strategies for synthesis of single-layered COFs are required to understand the unique properties of COFs caused by single-layered 2D orientation.

1.2 Synthetic methods of 2D layered material

The ability of the creation of synthetic 2D layered materials with desired composition, size, thickness, topology, defect is the major motive power for the development of various synthetic methods. By applying different methods for synthesis of 2D layered materials, different physical, chemical, electronic, and optical properties might be exhibited, and further, it has an influence on various potential application. For example, the value of physical properties of graphene, *i.e.* mobility or optical absorption coefficient, can be changed according to synthetic methods.[15]

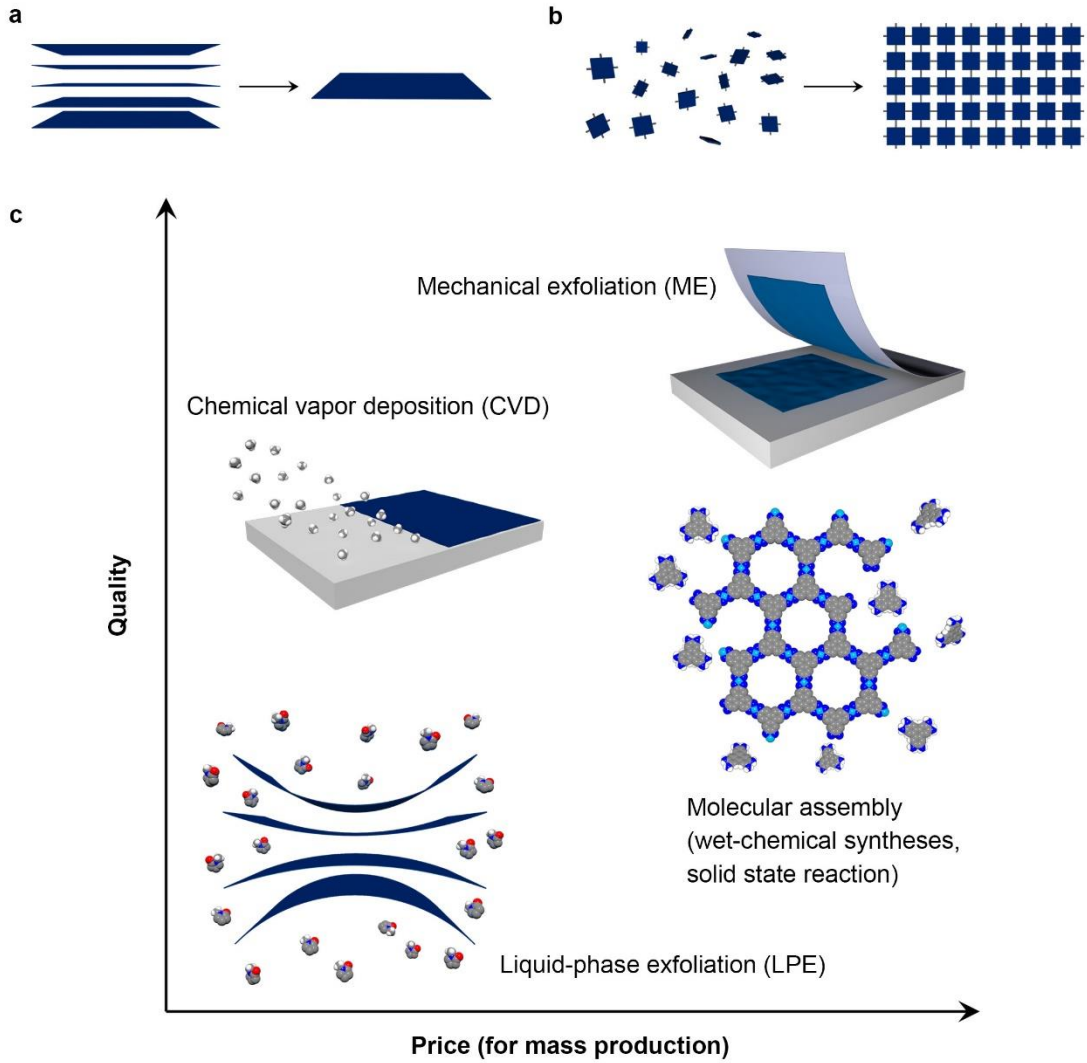

Figure 1.5 | Methods of 2D layered materials. **a**, **b**, Schematic representation of (**a**) top-down and (**b**) bottom-up approaches. **c**, Illustration of methods for production of 2D layered materials. Various methods allow a wide choice in terms of size, quality, and price for specific applications.

The well-established synthetic methods include the mechanical exfoliation, liquid-phase exfoliation, chemical vapor deposition (CVD), and wet-chemical syntheses. These methods can be classified into two categories: top-down and bottom-up approaches.[5,6](Figure 1.5) The major top-down approaches such mechanical exfoliation and liquid exfoliation, include the delamination of thin layered 2D crystals from their parent layered bulk crystals. Note that the top-down approaches are only correspond to those materials whose bulk crystals are layered compounds like graphite and layered transition metal dichalcogenides (TMDs) etc. Generally, these methods can produce 2D layered materials with high quality sheets, yet in limited quantities. On the other hand, CVD growth and wet-chemical synthesis belong to the bottom-up approaches, which are based on chemical reactions of certain precursors at

given experimental conditions. Most of the bottom-up approaches carry out in liquid media, which lead to producing limited grain size, since macromolecules become less soluble with increasing domain size, and subject to side reaction with increasing molecular weight. The growth on (catalytically active) solid surfaces makes it possible to avoid these issues.[6] Substrate-based growth can be accomplished by CVD, which based on the ability to proceed a narrow thermodynamic path. All types of 2D layered materials can be obtainable by bottom-up approaches because the precursors are limited to top-down approaches. Therefore, bottom-up approaches are more versatile in principle. In this section, I focus on the introduction of various well developed synthetic methods to produce 2D layered materials. The advances and limitations of each method are discussed along with addition of personal insights.

1.2.1 Mechanical exfoliation

The mechanical exfoliation (ME) technique is a prevalent method for scientists to fabricate thin sheets by splitting of layered bulk crystals, using Scotch tape.[26] In principle, the van der Waals interaction between the layers of bulk crystals is weaken by applying mechanical force *via* Scotch tape, hence the bulk crystals peel off single- or few-layers of 2D materials without breaking the in-plane covalent bonds of each layer.(Figure 1.6) In fact, it has been used for decades by material scientists whose are studying crystallography. In 1999, Lu et al. reported a controlled method of cleaving graphite, yielding films consisting of a few layers of graphene.[27] They also suggested that "more extensive rubbing of the graphite surface against other flat surfaces might be a way to get multiple or even single atomic layers of graphite plates." This was then firstly demonstrated in 2004, obtaining single layer graphene (SLG) using an Scotch tape by Novoselov, Geim, and co-workers,[14] as illustrated in Figure 1.6b. Later, the same group reported the extension of this technique to demonstrate the presence of other 2D materials, including *h*-BN, MoS_2 and $NbSe_2$, from their parent layered bulk crystals. Since then, MC has been widely used to exfoliate various 2D materials with varying layered bulk crystals by many other groups.[28]

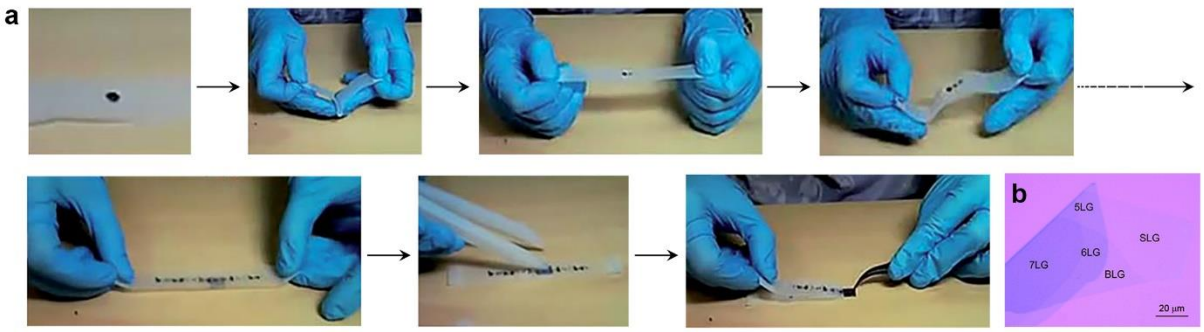

Figure 1.6 | Fabrication of graphene by mechanical exfoliation technique. a, Schematic representation of mechanical exfoliation. In a typical process, the bulk crystal (e.g., graphite) is first attached to the Scotch tape and then peeled it off by folding the tape right next to the flake. This process

can be repeated several times to cleave a thin flake. The freshly cleaved thin flake on the Scotch tape is then attached to a clean, flat target surface (e.g., SiO_2/Si), and rubbed using tools such as plastic tweezers to further cleave it. Finally, single- or few-layers of nanosheets left over on the substrate can be obtained by peeling off the Scotch tape. Reproduced with permission from ref.[26] Copyright 2015 The Royal Society of Chemistry. **b**, Optical micrograph of ME flake, consisting of regions of different thickness. Reproduced with permission from ref.[17] Copyright 2012 Elsevier Ltd.

The sizes of the flakes produced by ME (ME flakes) are approximately a few to tens of micrometers. (Figure 1.6b) Above all, ME flakes have very clean surface because no other chemicals or physical powers were introduced onto the surface during the exfoliation process. The relatively large grain size, clean surface, and excellent crystal quality make the ME flakes compelling candidates for the fundamental study of the intrinsic physical and electronic properties, as well as the demonstration of high performance electronic devices.[26]

It is believed that new types of 2D layered materials whose bulk crystals are layered compounds will be produced in this manner. This approach is still the best technique to fabricate 2D layered materials with perfect crystal quality from their layered bulk crystals by nondestructive method. However, there are still several disadvantages that restrict its practical application. First, the production yield of this technique is quite low, and thick flakes remain on the substrate along with the single- or few-layer nanosheets. Second, the production rate is rather slow. Both the low yield and the slow production rate make it difficult to fulfill the demands for various practical applications, high yield and large-scale production. Third, the size, the thickness, and the shape of the ME flakes are difficult to control because the exfoliation process is operated manually by hands, which lack the precision, controllability, or repeatability.[5] Although ME is impractical for large scale applications, it is still the method of choice for fundamental studies. Indeed, most of the basic results and prototype devices were achieved using ME flakes. Thus, ME remains ideal to investigate both new physics and new device concepts.

1.2.2 Liquid-phase exfoliation

Layered bulk crystals could also be exfoliated into 2D layered materials in liquid phase by applying ultrasounds to individual layers. The liquid-phase exfoliation (LPE) process generally involves three steps. Firstly, layered bulk crystals were dispersed in a specific solvent (*e.g.*, *N*-methyl-pyrrolidone (NMP)) before being treated with sonication at a certain time (Figure 1.7). After sonication, the suspension is needed to separate nanosheets from un-exfoliated flakes via centrifugation. The basic concept is same as sonochemistry; ultrasound can induce liquid cavitation during sonication.[29] The massive micrometer-sized bubbles or voids are formed, grown and collapsed in liquids due to pressure fluctuations. When these bubbles are collapsed, an intensive shear force will be generated on the layered bulk crystals, thus leading to the exfoliation of layered bulk crystals into thin layers of sheets. After

exfoliation, the solvent–graphene interaction needs to balance the inter-sheet attractive forces. The key role for achieving efficient exfoliation of layered bulk crystals is minimizing the interfacial tension [mN m^{-1}] between the solvents and 2D nanosheets. If the interfacial tension between layered bulk crystals and liquid is high, the flakes tend to agglomerate each other, result in poor dispersibility.[17,30] This method is simple and effective, which does not need any complicated equipment and expensive chemicals. It paves a new way for the high-yield and large-scale production of 2D nanosheets at low-cost in liquid phase.

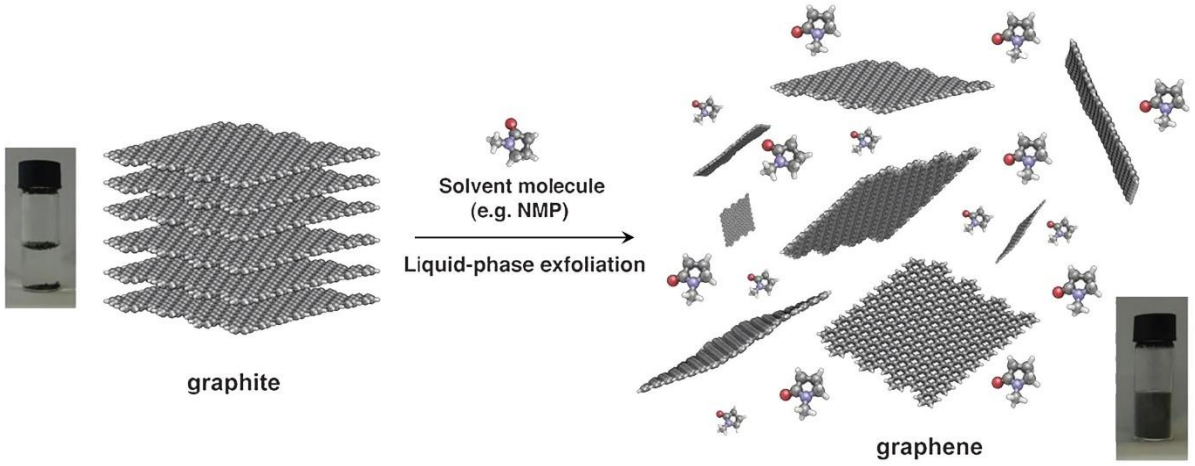

Figure 1.7 | Schematic illustration of liquid-phase exfoliation of graphite into graphene. Reproduced with permission from ref.[30] Copyright 2014 The Royal Society of Chemistry.

In 2008, Coleman's group firstly reported this technique by demonstrating the exfoliation of graphite into graphene.[31,32] Besides graphene, in 2011, Coleman and co-workers further extended this method for the exfoliation of layered bulk crystals into 2D nanosheets, including TMDs and *h*-BN.[33,34] In general, solvent is important in stabilizing the exfoliated nanosheets and prohibiting their restacking and aggregating. However, the lateral experimental and the theoretical results suggested that the appropriate surface tension between the layered crystals, not only the solvents choice, also plays a key factor for the efficient exfoliation.

Nowadays, the liquid-phase exfoliation has been widely utilized for exfoliation of numerous layered compounds into 2D nanosheets. The concentration, lateral size, in addition to thickness of the obtained nanosheets can be roughly tuned by controlling the sonication time, solvent system, polymers additive, ultrasonic power, sonication temperature, and the shape of vessels. Liquid-phase exfoliation is the simplest method for the high-yield and massive production of 2D layered materials in solution at low cost due to its facile process. Nevertheless, there are several disadvantages for the liquid-phase exfoliation. First, the yield of the single layer nanosheets in the exfoliation suspension is low. Most of the 2D flakes yield as a few-layered or multi-layered nanosheets. Technically speaking, these are hard

to justify 2D nanosheets. As known, some of the extraordinary properties of 2D layered materials only can be observed in its single-layer form. Second, the lateral size of the produced nanosheets is relatively small because the ultrasound breaks down the big nanosheets into small fragments.[5]

1.2.3 Liquid-phase exfoliation of graphene oxide (GO)

For the chemistry of graphene, there is another material by analogy to graphene, known as graphene oxide (GO). GO is a single layer of graphite oxide. The basic idea for producing graphite oxide is to use strong oxidizing agents to oxidize graphite to form graphite oxide by modified Hummers' method.[35,36] In a typical procedure, graphite is dispersed in sulfuric acid, leading to the formation of sulfuric acid-graphite intercalation compound (H_2SO_4-GIC, graphite sulfate). The intercalation is accompanied by increasing in the layer distance, which results in activation of the graphite. Subsequent oxygenation of H_2SO_4-GIC occurs on both sides of the basal plane in the presence of an oxidant such as potassium permanganate ($KMnO_4$). Currently, the identity of the specific oxidizing agent species attacking graphene layers is unclear. It was only assumed that either permanganate or *in situ* formed dimanganese heptoxide (Mn_2O_7) are the active oxidants.[37] As a consequence, the oxidation of graphite can generate abundant oxygen-containing functional groups on the basal plane of each graphene layer, which can remarkably expand the interlayer spacing of bulk graphite and spontaneously weaken the van der Waals interaction between adjacent layers. The solubilization of manganese–oxo species are accomplished by the addition of water and hydrogen peroxide. The resultant graphite oxide is purified by centrifugation and re-dispersion in water or by dialysis. Delamination of graphite oxide to GO in water can be facilitated by sonication. (Figure 1.8a) The size of deposited GO flakes typically varies between 10–100 nm and up to 100 μm.[18] Oxidation of graphite typically yields large amounts of GO nanosheets in the solution phase. However, the usage of hazardous chemicals such as strong acid or oxidizing agents in this process, can cause a safety and environmental problem. Moreover, it is hard to further extend this method to other layered materials, though it is very effective for the preparation of GO nanosheets.

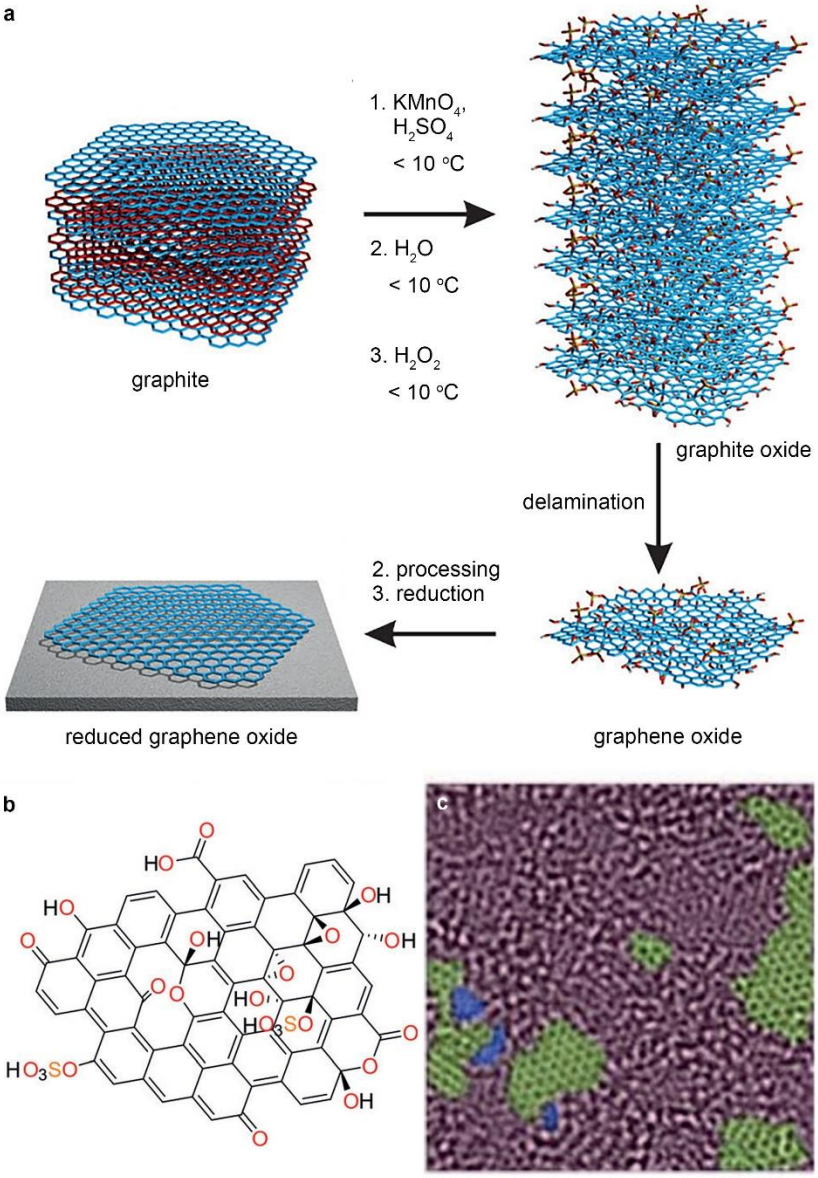

Figure 1.8 | Formation of graphene oxide (GO) and reduced graphene oxide (rGO) a, Schematic illustration of GO and reduced GO (rGO), starting from graphite in sulfuric acid with potassium permanganate as the oxidant. **b**, Structural model of GO. **c**, HRTEM image of GO displaying the preserved regions (green) of graphene (1–2 nm), holes (blue), and heavily oxidized regions (red). Reproduced with permission from ref.[18] Copyright 2014 Wiley-VCH Verlag GmbH & Co.

One of the main feature of GO is having abundant oxygen-containing functional groups, such as carboxyl, epoxy, and hydroxyl groups as described in Figure 1.8b. These oxygen-containing groups on GO nanosheets can be partially removed after reduction from GO to rGO nanosheets. The production of rGO to can be achieved by various reduction strategies, such as chemical reduction *via* reducing agents, thermal annealing. The simplest way is thermal annealing, which causes disproportionation of GO into CO_2 and graphene. Although this method is attractive due to its simplicity, perfect graphene is

not obtained, even at temperatures up to 1100 °C.[18]

The presence of abundant functional groups on GO nanosheets allow them to be easily modified with organic or polymeric molecules *via* covalent functionalization. The physical, chemical and electrical properties of GO nanosheets can be easily tuned by controlling the number of functional groups on its surface. Although GO has high processability comparing with other 2D materials, GO is only defective material lowering the quality of graphene. For example, graphene has an excellent electrical conductivity, while GO nanosheet is electrically insulating, with sheet resistance (R_S) ~ 10^{12} Ω sq^{-1}, or higher. Even after reduction back to its rGO form, the electrical conductivity of rGO sheets is still not as good as those obtained from mechanical exfoliation or CVD-grown.[38] Besides, GO nanosheet is amphiphilic and even is well dispersed in water, while graphene is highly hydrophobic. Because of their distinctive properties from graphene, GO and rGO were defined as graphene derivatives rather than graphene, although graphene has been widely used to name rGO nanosheets in many published papers.

1.2.4 Chemical vapor deposition (CVD)

CVD is a traditional technique for the preparation of high purity materials by deposing or growing thin films or crystals from solid, liquid or gaseous precursors of many materials. Over the past decades, CVD has been a breakthrough for development of graphene research as it enables to produce large-area and high-quality graphene. Synthesis of graphene by CVD firstly reported in 2009 by Ruoff and co-workers, who demonstrated the growth of large-area single-layer graphene film up to 0.5 mm on copper foil by the CVD method by using methane and hydrogen as gas sources.[39] By optimizing those experimental parameters such as precursors, substrates, catalysts, temperature, and atmospheres, the controlled growth of graphene with tunable layer number, crystallinity, and lateral size can be achieved on different substrates with different precursors by the CVD technique.[40] Likewise, CVD can be extended for the growth of many other 2D nanosheets on various substrates, such as *h*-BN and TMDs.[10] (Figure 1.9)

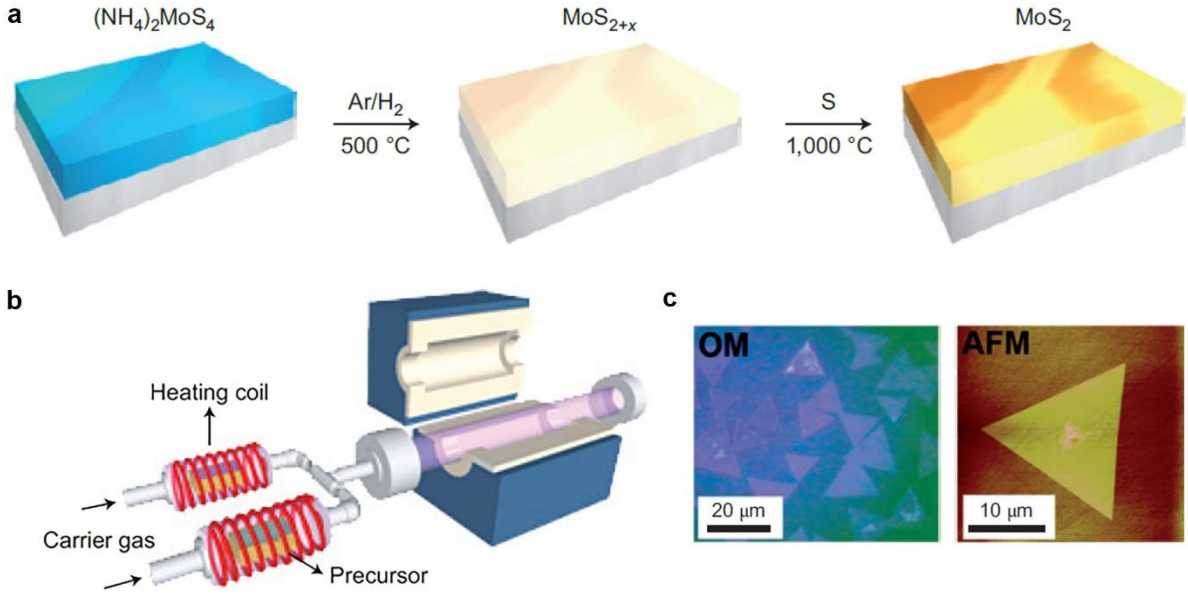

Figure 1.9 | Schematic illustration of CVD. In a typical process, the preselected substrates are put in a furnace chamber, and one or more gas/vapor precursors are pass through the chamber, in which the precursors can react and/or decompose on the surface of substrates. For growth of graphene, metal substrate works as a catalyst to lower the energy barrier of the reaction. **a**, Schematic of MoS_2 layer deposited by two-step thermolysis. **b**, CVD of ultrathin TMDs by vaporization and decomposition of metal and chalcogen precursors in solid forms. **c**, Optical micrograph and atomic force microscopic images of the MoS_2 triangular nanosheets. Reproduced with permission from ref.[10] Copyright 2013 Nature Publishing Group.

Most of the current CVD research has focused on MoS_2. From now on, several approaches for synthesis of MoS_2 has been demonstrated since 2012. The first report was a two-step thermolysis process; insulating substrate was dip-coated in ammonium thiomolybdates [$(NH_4)_2MoS_4$] and directly coverted to MoS_2 by annealing at 500 °C followed by sulfurization at 1,000 °C in sulfur vapor. (Figure 1.9a)[41] Another strategy for the deposition of few-layer MoS_2 nanosheets was achieved by sulfurization of Mo metal film. Transition metal oxides and transition metal chlorides (e.g., MoO_3 and $MoCl_5$) can alternative for the Mo sources to produce MoS_2 nanosheets by gas-phase reaction.[42,43] Up to now, many 2D nanosheets of TMDs have been grown by the CVD technique by changing experimental parameters including precursors, temperatures, types of substrate and reaction atmospheres.[10]

The CVD yields best quality to prepare 2D materials with high crystal quality, high purity, and limited defects on certain substrates with scalable size and controllable thickness. Significantly, the electronic properties of 2D materials, such as graphene and TMDs, are quite similar to those of mechanically exfoliated thin layers. Furthermore, they can be produced in industry scale unlike the microchemical cleavage method. Therefore, it is believed that CVD is a promising method to produce 2D materials in

industry applications for electronics and optoelectronics. The CVD method still has some disadvantages at its current form. 2D materials grown by the CVD technique are always deposited on the substrates, needing to be transferred to other substrates for further investigation and applications. The CVD technique normally needs high temperature and inert atmosphere, leading to relatively high cost of production as compared to the solution-based methods.

1.2.5 Wet-chemical syntheses

Wet-chemical syntheses represent the synthetic approaches that rely on the chemical reactions conducted in solution phase. They have been considered as a class of facile and reproducible strategies for the preparation of 2D layered materials because of their controllability. Particularly, wet chemical syntheses have been widely used for preparing various non layer structured 2D materials because they are unable to be prepared by those top-down methods.[44] In this section, I focus on the introduction of these typical wet-chemical protocols for the syntheses of 2D layered materials. The advances and limitations of each synthetic route are also discussed.

1.2.5.1 Hydro/Solvothermal Synthesis

The hydro/solvothermal synthesis is a typical wet-chemical synthesis strategy for preparing a variety of materials such as metals, semiconductors and polymers. The process involves the use of a solvent under moderate to high pressure (typically between 1 atm and 10,000 atm) and temperature (typically between 100 °C and 1000 °C) in a sealed vessel that facilitates the interaction of precursors during synthesis. If water is used as the solvent, the method is called "hydrothermal synthesis."[45] When the reaction temperature of the closed system is heated above the boiling point of the solvent system, the pressure will be generated to promote the reaction and improve the crystallinity of the as-synthesized nanocrystals. The crystallinity of this process is controlled by manipulating the selection of the solvent, chemical composition of the precursors and reaction mechanism. This method has been widely used to prepare thermodynamically stable 2D nanomaterials that cannot be easily formed from other synthetic routes, *i.e.* inorganic materials.[44] As a typical member of TMDs, the MoS_2 nanosheet can also be synthesized by a facile hydrothermal method. Xie and co-workers reported the preparation of few-layer defect-rich MoS_2 nanosheet with the assistance of excess thiourea.[46] In addition to TMDs, a lot of 2D materials of covalent organic frameworks have also been synthesized by this method. Since Yaghi and co-workers demonstrated the synthesis of the first crystalline COF, this method has become a popular approach for the formation of layered organic crystals.[4] Such layered crystals typically exist in bulk powder due to strong interlayer interactions, most commonly π–π interactions, which can limit the access to individual layers.

The hydro/solvothermal synthesis is a simple and scalable method for the synthesis of 2D layered

materials in high yield and low cost. The hydro/solvothermal synthesis is quite sensitive to the experimental conditions, such as the concentration of precursors, solvent systems, used surfactants or polymers, and temperature, making it difficult to precisely control the structure in different batches and laboratories. Most of the 2D nanosheets synthesized by the hydro/solvothermal synthesis method were few-layer rather than single-layer.

1.2.5.2 Thermodynamic and kinetic control in wet-chemical synthesis

The crystalline or amorphous nature of a 2D layered material produced by wet-chemical synthesis depends on how the monomer assembly is controlled before or during reaction. Growth direction should be controlled by two directions, x and y, not one direction; otherwise, crosslinked, hyperbranching networks are obtained. Two strategies provide such control for chemical synthesis. One is thermodynamic control, rely on the reaction pathway moving from the initial state to the most stable product state. Another is kinetic control, concerned with lowering energy barriers in certain pathways.[47]

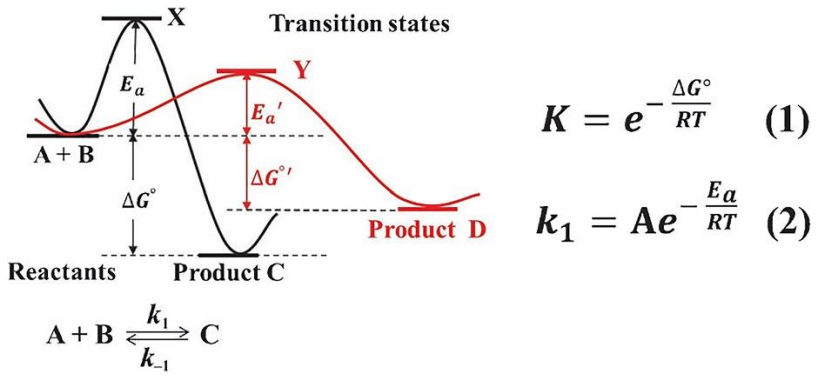

Figure 1.10 | Simple energy landscape illustrating the choice between the thermodynamically (black line) and kinetically (red line) controlled products. C is the thermodynamically favored product and D is the kinetically favored one. Reproduced with permission from ref.[47] Copyright 2015 Wiley-VCH Verlag GmbH & Co.

As described in Figure 1.10, the activation energy in red pathway (E_a') is lower than black one (E_a). Therefore, the reaction corresponding to the kinetic pathway is significantly faster than thermodynamic pathway and leads to D as the main product at initial stage. That's why most of the product made by wet-chemical syntheses form amorphous products with the random arrangement at the beginning of the reaction. On the other hand, if an equilibrium is established, the reaction will follow the thermodynamic pathway to form the most stable product, thus making C as the main product. It is common in wet-chemical syntheses that amorphous products are initially obtained (kinetically favored reaction) until the synthetic conditions are optimized by varying the crystallization times, reaction temperatures, reaction solvents, and catalysts (such as acids, bases, and metal salts acting as Lewis acids,

thermodynamically favored reaction).[47,48,49] Hence, the atoms or molecules has to connect with weak bond such as coordination bond or reverse bond (dynamic covalent chemistry) to form a 2D materials with organized assemblies.

1.2.5.3 Interfacial syntheses

Interfacial syntheses are another typical bottom-up route for the synthesis of 2D layered materials, especially for metal coordination polymers (CPs) and polymers. This method simply defined as the reaction of immiscible reactants at the interface of two liquids or gases/liquids. The confinement of two reactants at the interface to prepare free-standing few-layer 2D nanosheets with large lateral dimensions.[50] The presence of the liquid/liquid interface can accelerate the reaction, or a phase-transfer catalyst is employed to draw the reaction in one phase of choice. Transfer of the 2D nanosheets usually achieved by Langmuir-Schäfer method. As an interesting example, Nishihara and co-workers reported the synthesis of a single-layer nickel bis(dithiolene) nanosheet at the gas/liquid interface.[51,52] In their case, the single-layer 2D CP nanosheet was synthesized in a gas/liquid interface by spraying an ethyl acetate solution of benzenehexathiol onto an aqueous solution of nickel (II) acetate. Later, Zhu and co-worker further extended this method for the synthesis of a series of 2D CP nanosheet, copper bis(dithiolene) at liquid/liquid interface.[53]

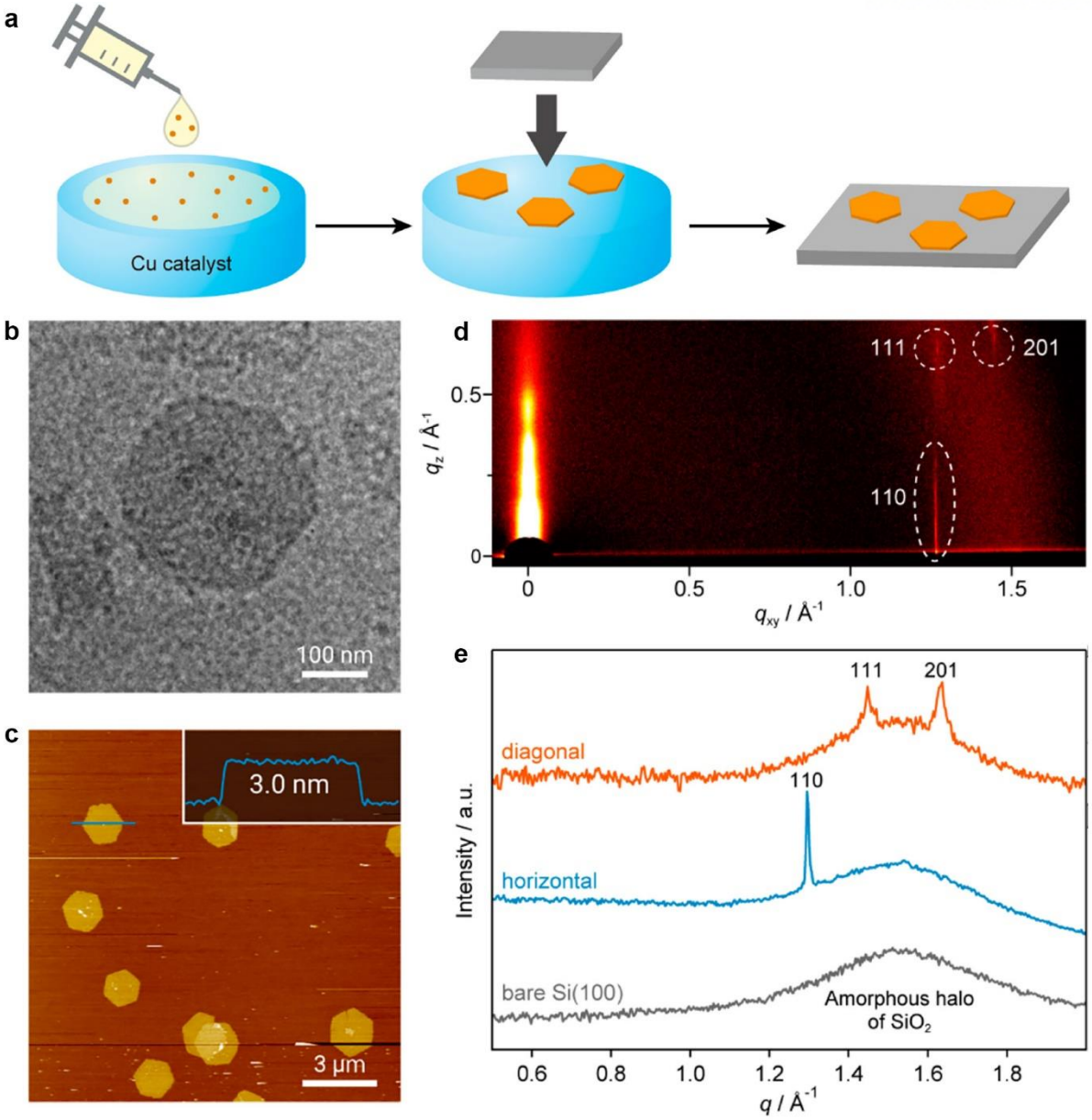

Figure 1.11 | Gas/liquid interfacial synthesis and microscopic observations of few-layer graphdiyne. a, Schematic illustration of the gas/liquid interfacial synthesis and transfer process. **b**, TEM micrograph on an elastic carbon grid. **c**, AFM topographic image on HMDS/Si(100) and its cross-sectional analysis along the blue line. **d**, 2D GIWAXS pattern on Si(100). **e**, Horizontal (blue) and diagonal (orange) plots from the 2D GIWAXS pattern shown in panel **d**. Numerical values denote Miller indices. Reproduced with permission from ref.[54] Copyright 2017 American Chemical Society.

In addition to CPs, 2D COF[55] or graphdiyne[54] nanosheets have also been prepared by the interfacial synthesis. Nishihara group firstly demonstrated the synthesis of 2D graphdiyne nanosheets by liquid/liquid or gas/liquid interfacial reaction.[54](Figure 1.11) The lateral size and thickness of few-layer graphdiyne is 1.5 μm and ~3 nm, respectively. Interfacial syntheses could be promising method for

producing few-layer 2D nanosheets ranging from coordination polymer to covalent-bonded polymer which is alternative to wet-chemical syntheses.

1.2.6 Solid state reaction

As mentioned in Section 1.2.5.1, most of bottom-up routs are often prepared under thermodyanamic approaches, rely on reversible bond-forming conditions. In a different approach, two distinct groups independently reported an ordered 2D polymer with internal periodicity by the crystal-to-crystal photopolymerization. The basis of this approach is solid state reaction; monomer should be prepared in single crystals with preorganized shape. This precise placement of the monomer in single crystals inhibits undesirable molecular motion and enables a lateral polymerization. It should be noted that the reaction is controlled by kinetic approaches which the reaction is progressed under irreversible bond-forming conditions. Therefore, the preparation of monomer with exact packing is critical for the solid state reaction; otherwise, aperiodic, hyperbranching network are obtained.[48]

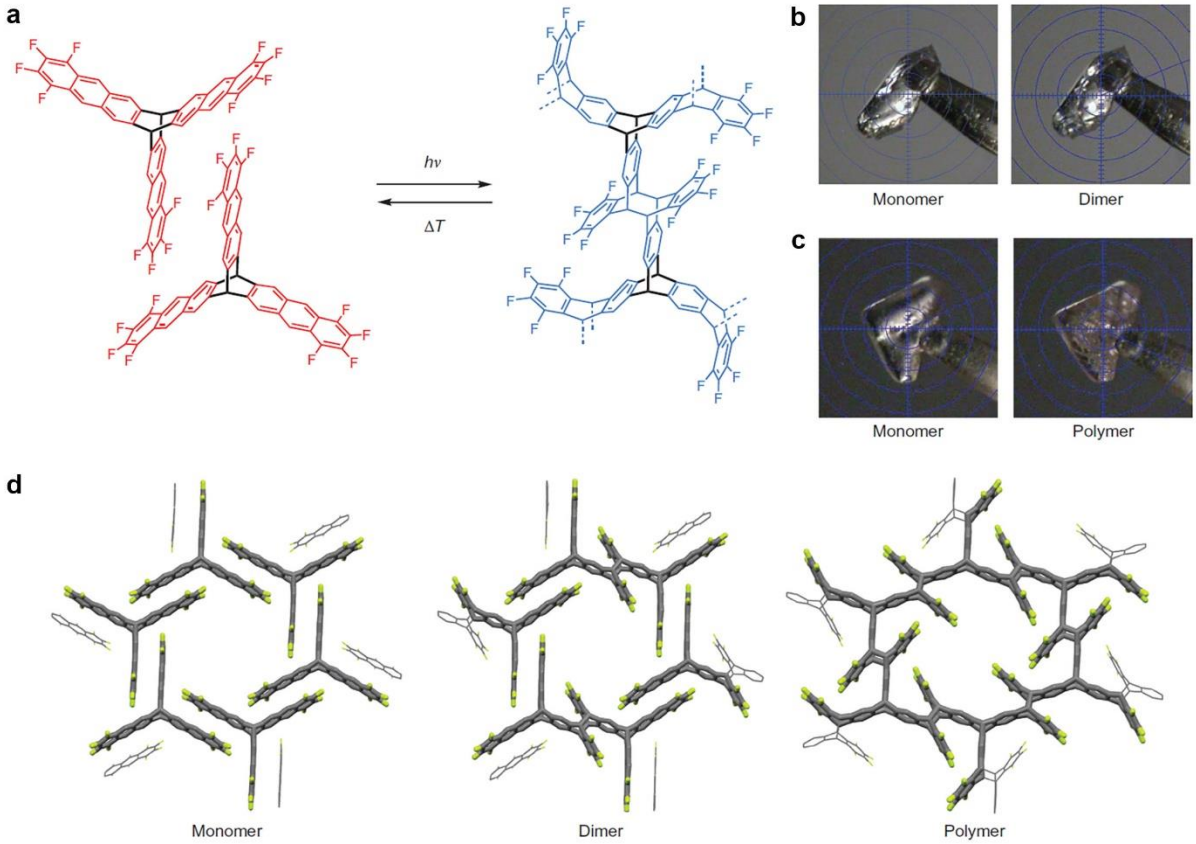

Figure 1.12 | Overview of the crystal-to-crystal photopolymerization. **a**, Chemical structure of the monomer fantrip (left) and the corresponding 2DP, poly(fantrip) (right). **b**, Single crystal of the fantrip monomer before and after irradiation (223 K, 460 nm, 80 min). **c**, Single crystal of the fantrip monomer before and after irradiation (223 K, 460 nm, 150 min) followed by a second irradiation (223 K, 400 nm,

70 min). **d**, X-ray crystal structures of the fantrip monomer, fantrip dimer and poly(fantrip). The monomer and polymer structures correspond to the crystals shown in c and the dimer corresponds to the crystal shown in **b**. Reproduced with permission from ref.[56] Copyright 2014 Nature Publishing Group.

In 2013, King and co-worker studied formation of triptycene-based 2D polymer nanosheet in the solid state[57] and later they further extended study by using fluorinated triptycene-based single-crystalline monomer (fantrip).[56](Figure 1.12) Photopolymerization of the triptycene-based single-crystalline monomer by [4+4] cycloaddition was conducted by irradiation of these crystals with 400 nm UV light under N_2 atmosphere and it was confirmed that the monomer polymerization occurs by dimerization at its medial positions and thus the polymer's microstructure could be established. The obtained polymer bulk crystal was then exfoliated into single- or few layer nanosheet by rotating them in NMP at 50 °C for several days. Concurrently, Sakamoto and co-workers demonstrated the preparation of chiral 2D polymer crystal by photopolymerization of a single crystal of an enantiomorphic monomer, and Schlüter and co-workers further studied using similar enantiomorphic monomer.[58,59] This is a particularly interesting property that cannot be normally achieved by molecular and supramolecular systems.

1.3 Modification of 2D layered materials

Considering specific applications of 2D layered materials, the band gap, dispersibility, and processability of the materials can be customized by postsynthetic modification of 2D layered materials with organic and inorganic molecules. The postsynthetic modification of 2D layered materials involves modification of initially prepared 2D layered materials. The postsynthetic modification offers an effective route for the incorporation of several functional groups in 2D layered materials. This process allows to tailor the chemical environment of the materials, thus making the materials worthier for advanced applications.[25] In this section, I provide an overview on the well-known postsynthetic modification of 2D layered materials, including functionalization of 2D layered materials *via* addition or substitution reaction. I will discuss suitable reaction for functionalization of 2D layered materials especially in covalent functionalization.

1.3.1 Cycloaddition reaction

A cycloaddition reaction is one in which two unsaturated molecules add to one another, yielding a cyclic product. It is a simple protocol for introducing sp^3 defects in aromatic framework. Consequently, this offers the potential to improve the processability of 2D layered materials. However, the reaction alters the intrinsic electronic properties of materials. It is therefore a challenge to develop a reaction to control

the functionality.[19] The most famous reaction of cycloaddition is Diels-Alder reaction, a pericyclic process that takes place between a diene (four π electrons) and a dienophile (two π electrons) to yield a cyclohexene product. Diels-Alder reaction on graphene changes the hybridization of an aromatic rings from sp^2 to sp^3, leads to an efficient opening of a bandgap on the carbon materials.[60] Haddon and co-workers studied the reactivity of exfoliated graphene on Si substrates in Diels-Alder reaction. Graphene is used as diene and some adducts such as tetracyanoethylene (TCNE) or maleic anhydride (MA) are used as dienophile respectively, and the reaction was monitored by Raman spectroscopy.[61]

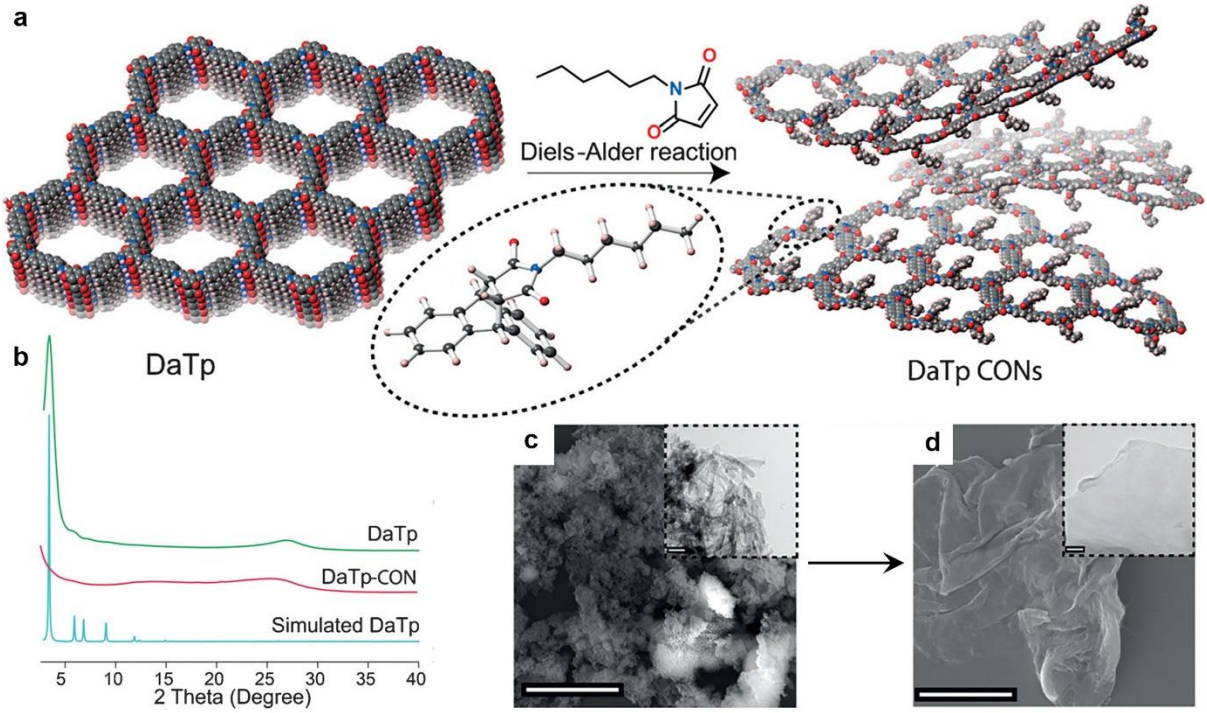

Figure 1.13 | Chemical exfoliation of *N*-hexylmaleimide-functionalized CONs. a, Schematic representation of the exfoliation process. **b**, Experimental PXRD patterns of DaTp and DaTp-CONs and simulated PXRD pattern of DaTp in eclipsed mode. **c**, SEM image (5 μm) of DaTp. Inset in **c**: TEM image (100 nm) of DaTp. **d**, SEM image (5 μm) of DaTp-CONs. Inset in **d**: TEM image (100 nm) of DaTp-CONs. Reproduced with permission from ref.[62] Copyright 2016 Wiley-VCH Verlag GmbH & Co.

In addition to graphene, anthracene-functionalized COF also synthesized *via* Diels-Alder reaction. (Figure 1.13) The introduction of N-hexylmaleimide within the COF backbone disturbs the van der Walls interactions and the planarity of the individual layers, which results in exfoliation to prepare N-hexylmaleimide-functionalized covalent organic nanosheets.[62]

1.3.2 Oxidation

Oxidation has traditionally been the most common postsynthetic method in the field of 2D layered

materials. Oxidized 2D layered materials can be easily prepared by aggressive acid treatment, as for example with the Hummers method (see Section 1.2.3).[18,37] However, this method is too corrosive, causing the structural defects of 2D layered materials. The direct oxidation in the presence of oxygen can be an alternative approach for oxidizing this kind of 2D layered materials. In contrast with graphene or carbon nitride, this method is not applicable in TMDs. It should be noted that the single-layer TMDs are exhibit poor long-term stability in air. After room-temperature exposure to the environment for several months, monolayers of TMDs undergo dramatic aging effects including extensive cracking, changes in morphology.[63] Not all the oxidations are harmful to 2D layered materials, as one might think that oxidation may impair the structure of 2D layered materials. As an example, Yaghi and co-workers demonstrated chemical conversion of linkages in COFs by direct oxidation from imine moieties to amide moieties without the loss of their crystallinity and permanent porosity. Through the oxidation, the amide COFs show improved chemical stability under aqueous acidic and basic conditions relative to their corresponding imine-linked framework.[64]

1.4 Research overview and objective

The past two decades have seen unprecedented increase in research progress on 2D layered materials in the field of materials science after the discovery of graphene in 2004 by mechanical exfoliation of graphite. The unique class of materials has demonstrated outstanding intrinsic properties and thus is being explored for various potential applications. However, these properties might be reflected sometimes as an "undesirable" properties in terms of processability, hence they disrupt the development of specific applications. To overcome the limitation, synthetic modification has been an alternative to improve the processability. Synthetic modification can tailor the physical and chemical properties by introducing or changing the functionality into the 2D materials. Ultimately, it might enhance the processability for practical applications. The development of chemical modification for 2D layered materials has generally lagged considerably behind compared with other 1D and 3D analogues. Therefore, it represents an attractive challenge for synthetic chemists.

The focus of the thesis is on the synthesis and modification of 2D layered materials, which allow to enhance processability for practical applications. In the first half of this thesis, I discuss postsynthetic modification of graphite into graphene nanoplatelets *via* solvent-free Diels-Alder reaction. The one-pot Diels-Alder reaction of pristine graphite enables to functionalize dienophiles at the edge of graphite, which facilitate to delaminate into graphene nanoplatelets by dispersing them into common organic solvent. The organic functionality acts as a stabilizer of solvent-dispersed graphene nanoplatelets, which finally hinders to reaggregate them in solution to get a better processability. Moreover, chemical properties can be tuned by changing the dienophiles. To demonstrate the reactivity depending on synthetic approaches, two approaches were selected. The one is Diels-Alder reaction of graphite *via* mechanochemical approach which described in chapter 2, the other is solvothermal approach discussed

in chapter 3. The resultant product made by mechanochemical approach has higher degree of functionalization than the other one produced by solvothermal approach, hence mechanochemical approaches is more powerful than solvothermal approaches in graphene chemistry. The second half of this thesis focuses on synthesis and presynthetic modification of COF. Firstly, the synthesis of imine-linked COF with high crystallinity and porosity is discussed in chapter 4. To improve the reactivity of COF, I designed small-pore crystalline COF using specific triamine building block including hydroxy groups. The resultant imine-linked COF showed high crystallinity and microporosity, and it exhibited high thermal stability. To improve the stability of COF, I explore synthesis of imide-linked COF in chapter 5. Typically, synthesis of imide linkage proceeded two step reactions, including formation of amic acid linkage and subsequent imidization of imide linkage. The first step is reversible; however, the second step is irreversible. Hence the linkage is more stable than other common reported COF linkage. Because of the irreversible second step imidization, the imide-linked COF showed high thermal stability along with the 1D polyimide analogues. The last part of this thesis, I briefly summarize my Ph.D. studies.

Chapter 2 MECHANOCHEMICALLY DRIVEN SOLVENT-FREE DIELS-ALDER REACTION OF GRAPHITE INTO GRAPHENE NANOPLATELETS†

2.1 Introduction

Over the past few decades, highly ordered graphitic materials, including carbon nanotubes (CNTs)[65] and graphene[14], have been the subject of many studies in academia and industry because of unprecedented properties that arise from all-sp^2-hybridization.[12] One of the fundamental properties that results from the exotic conjugated π-electron system is chemical inertness. Graphitic materials remain intact under ambient conditions and after exposure to most caustic chemicals, therefore they can be subjected to most processing and characterization methods without the need to take any precautions.[66] However, it should be noted that chemical inertness is not always helpful in processing these graphitic materials. Due to issues regarding processability and dispersibility, there are still challenges to face in various applications, particularly energy-related applications, catalyst support, and reinforcement of composites. Covalent modification of the graphitic materials is certainly a key to addressing these issues. The ability to modify the surface of graphitic materials by functionalization leads to improvement of dispersibility and processability. In addition, covalent functionalization allows tailoring and tuning of their electronic and mechanical properties.[67,68]

Hitherto, various methods for the functionalization of graphitic materials have been devised including radical addition,[69,70] cycloaddition,[71,72] hydrogenation,[73,74] and fluorination.[75,76] In almost all instances, the reaction sites can become rehybridized from sp^2 carbon to sp^3 carbon atoms. This alters the exceptional physical properties of the graphitic materials. For instance, the mobility of the charge carriers and the conductivity of the graphitic material are reduced after covalent functionalization.[6,60] Therefore, the development of effective protocol for edge-selective functionalization is needed to preserve the intrinsic properties of graphitic materials.

Diels-Alder reaction, *i.e*., [4 + 2] cycloaddition, is attractive and versatile alternative used in various graphitic materials, because a wide variety of functional groups can be introduced. In contrast to fullerene and carbon nanotubes, which always act as the dienophile in [4 + 2] cycloaddition due to their curvatures,[77,78] 2-dimensional graphene and its derivatives are able to behave as both diene and dienophile.[61,79] Based on this hypothesis, Haddon, *et al*., reported the Diels-Alder reaction of graphene on its basal plane by heating of graphite and dienophile.[79] For thermal reaction in solution, a rather large amount of solvent is usually required due to the poor solubility of graphite in common organic solvents. Consequently, solution-based Diels-Alder reaction results in a low degree of functionalization with poor yield.[80] As an alternative method for solution-based synthesis, solvent-free synthesis of graphitic materials has been proposed to overcome this difficulty.[81] On the basis of our previous works on the

mechanochemical modifications of graphite *via* dry ball-milling in the presence of dry ice[82] and reactive gases,[83] here, for the first time, we report solid-state [4 + 2] cycloaddition between graphite and dienophile. Graphite was selected as a diene, and maleic anhydride (MA) and maleimide (MI) were chosen as dienophiles to ensure feasibility. Compared with many previous methods, the approach applied in this work is simple but efficient to produce edge-selectively functionalized graphene nanoplatelets (EFGnPs). The resultant EFGnPs are highly dispersible in various polar solvents, including water. Furthermore, each EFGnP shows different dispersibility depending on the nature of the functional groups.

2.2 Experimental

2.2.1 Materials

Graphite (natural, 100 mesh, <150 mm, 99.9995% metal basis, Lot no. 14375) was obtained from Alfa Aesar. Maleic anhydride (MW = 98.06) and maleimide (MW = 97.07) were purchased from Sigma-Aldrich Chemical Inc. and used as received. Solvents were used as received.

2.2.2 Synthesis of MA-GnPs and MI‑GnPs by ball‑milling

In a typical procedure, pristine graphite (5 g) and maleic anhydride (10 g, 0.102 mol) or maleimide (10 g, 0.103 mol) were placed into a stainless steel container with stainless steel balls (500 g, 5 mm in diameter). The container was sealed and degassed with argon using 5 evacuate-refill cycles. The container was then fixed in the planetary ball-mill machine (Pulverisette 6, Fritsch, Germany) and agitated at 500 rpm for 48 h. Thereafter the resultant products were stirred with 1 M aqueous HCl solution to completely acidify the residual active species and to remove metallic impurities, if any. Further Soxhlet extractions were conducted with tetrahydrofuran (THF) and water for 72 h and 48 h, respectively, and freeze-dried at −120 °C under a reduced pressure (0.05 mmHg) for 48 h to yield 6.45 g of MA-GnPs and 7.09 g of MI-GnPs as a dark-black powder. Found for MA-GnPs: C: 86.10%; H: 1.07%; O: 10.10%. Found for MI-GnPs: 84.97%; H: 1.21%; O: 8.91%; N: 3.06%.

2.2.3 Physical characterization

Fourier transform infrared (FT-IR) spectra were recorded on a Perkin-Elmer Spectrum 100 using KBr pellets. Thermogravimetric analysis (TGA) measurements were performed on a TA Instrument Q200 Thermogravimetric Analyzer. The samples were heated from 50 to 900 °C under an air or a nitrogen at a heating rate of 10 °C min^{-1}. The morphology of the as-prepared samples was examined by field-emission scanning electron microscopy equipped with an energy dispersive spectrometer (FE-SEM, FEI Nanonova 230). Samples were deposited onto a conductive carbon tape without coating and imaged at 10 kV without tilting. Elemental analysis (EA) was conducted on a Thermo Scientific

Flash 2000. X-ray photoelectron spectra (XPS) were recorded on a Thermo Fisher K-alpha XPS spectrometer. Raman spectra were recorded using an Alpha 300S confocal Raman spectrometer (WITec, Germany) with a 532 nm He-Ne laser. Contact angle measurements were conducted on a Krüss DSA 100 contact angle analyzer. Samples were dissolved in NMP at a concentration of 10 mg ml^{-1} and sonicated 1 min. Then the solutions were dip coated on a silicon (Si) wafer and dried under vacuum oven at 70 °C.

2.3 Results and Discussion

2.3.1 Synthesis of edge‑selectively functionalized graphene nanoplatelets (EFGnPs)

MA- (MA-GnPs) and MI-functionalized graphene nanoplatelets (MI-GnPs) were synthesized by [4 + 2] cycloaddition *via* ball-milling of graphite in the presence of MA or MI, respectively, as a corresponding dienophile (Figure 2.1a). Large pieces of pristine graphite flake (100 mesh, >150 mm, Figure 2.1b) were readily crushed into small grain sizes of graphene nanoplatelets (GnPs) (Figure 2.1c and d), suggesting that the mechanochemically driven reaction by ball-milling should lead to changes in the morphologies of the resultant edge-selectively functionalized GnPs (EFGnPs). The grain sizes of the resultant EFGnPs were dramatically reduced to the range of 0.1-1 μm, compared with pristine graphite. This result implies that mechanochemical ball milling effectively promotes C–C bond breaking, functionalization, and subsequent delamination of graphite into GnPs.

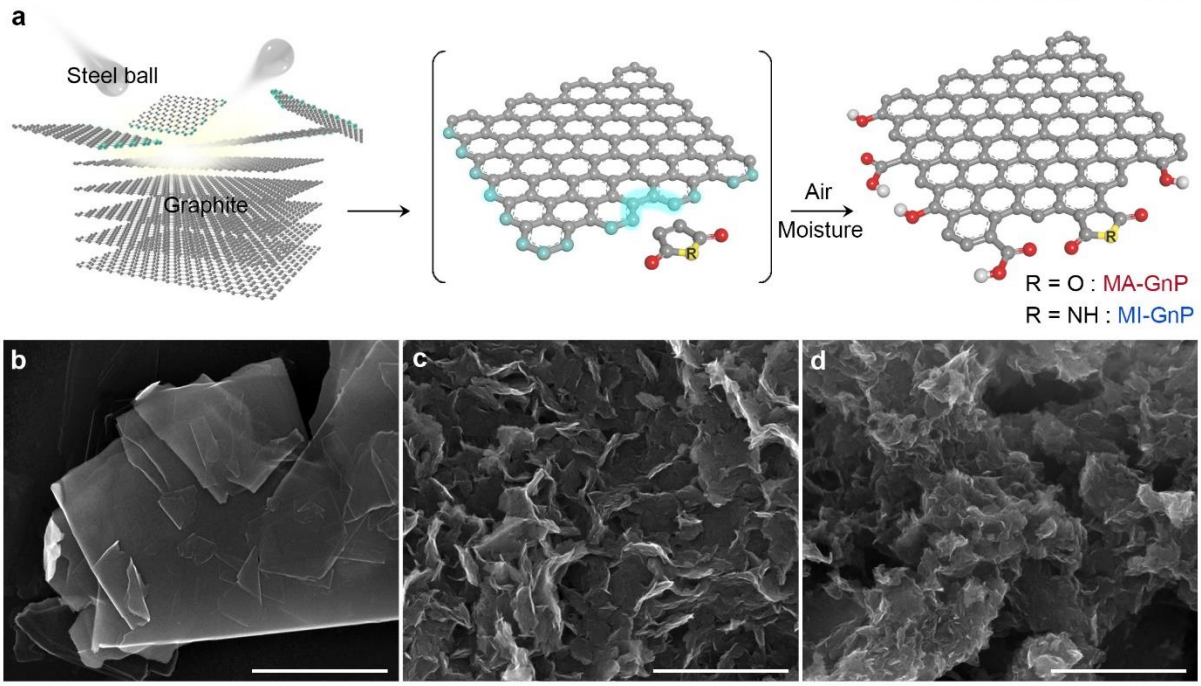

Figure 2.1 | Solvent-free Diels-Alder reaction of graphite into graphene nanoplatelets *via* mechanochemical approach. a, Schematic representation of the mechanochemically driven solid-state Diels-Alder reaction between *in situ* generated active carbon species by ball milling in the presence of a specific dienophile, maleic anhydride (MA) or maleimide (MI). Active carbon species along the broken edges would more efficiently promote [4 + 2] cycloaddition, and the remnant should be terminated by subsequent exposure to air moisture, forming oxygenated groups. The anhydride moieties at the edges of MA-GnPs could be hydrolyzed into carboxylic acids during acid-mediated work-up procedures. **b-d**, SEM images: (**b**) pristine graphite; (**c**) MA-GnPs; (**d**) MI-GnPs. The morphologies of MA-GnPs and MI-GnPs show more fluffy than pristine graphite, indicating that the graphitic layer could be delaminated into a graphene nanoplatelets without solvent system. Scale bars are 1 μm.

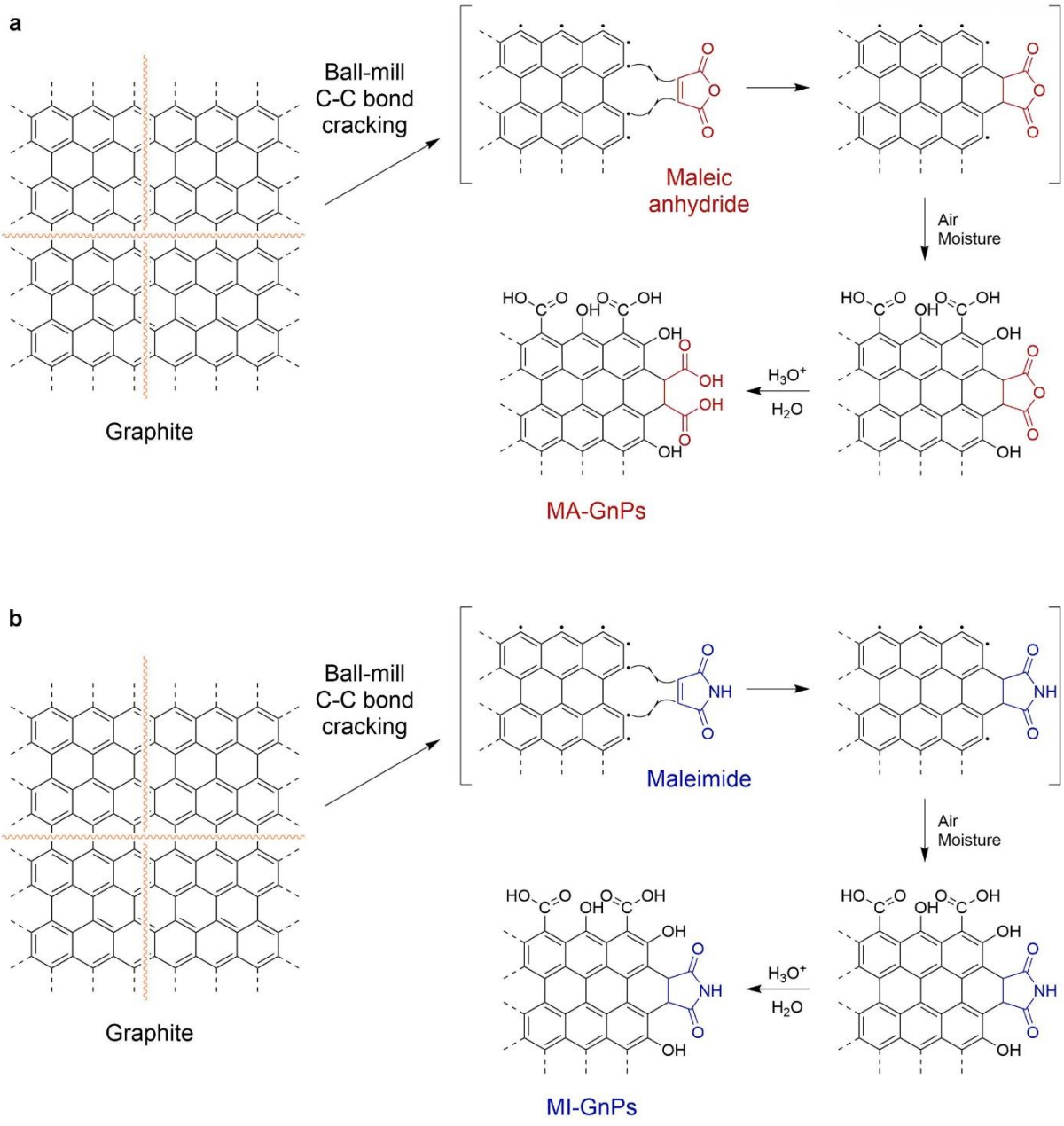

Figure 2.2 | Synthetic mechanism of the EFGnPs. Proposed mechanism for the edge-selective functionalization of graphite by mechanochemical cracking of graphitic C–C bonds in the presence of maleic anhydride (MA) or maleimide (MI) to yield: **a**, MA-GnPs; **b**, MI-GnPs, respectively. The graphitic structure is simplified and idealized for clarity.

The kinetic energy of high-speed steel balls cracks the graphitic C–C bonds and generates reactive carbon species. It is known that reactive carbon species are mostly radicals due to hemolytic cleavages and ions (cations and anions) due to heterolytic cleavages along the broken edges,[82] which may lead to efficient promotion of [4 + 2] cycloaddition. Based on perylene as a miniature model compound for graphite, it is known that [4 + 2] cycloaddition occurs at the bay region of perylene, which, in turn, implies that [4 + 2] cycloaddition reacts at the armchair edges of graphite.[84] Therefore, cycloaddition is

expected to occur more along armchair edges rather than zigzag edges and the graphitic basal plane in the presence of MA or MI as dienophile (see Figure 2.1a and Figure 2.2). The rest of the remnant active carbon species at the armchair and zigzag edges could be terminated by exposure to air moisture. As a result, some oxygenated groups, such as hydroxyl (–OH) and carboxylic (–COOH) groups should also be introduced at the cracked edges of the resultant EFGnPs (Figure 2.1a).[83]

The weight increased in both MA-GnPs and MI-GnPs after mechanochemical ball-milling, and complete work-up procedures showed evidence of the weight gaining functionalization *via* solid-state Diels-Alder reaction (see Experimental section). Elemental analysis (EA) showed that MA-GnPs and MI-GnPs have the carbon contents of 86.10% and 84.97%, respectively, and oxygen contents of 10.10% and 8.91%, respectively (Table 2.1), while pristine graphite has carbon and oxygen contents of 97.71% and below the detection limit, respectively. Furthermore, only MI-GnPs have a nitrogen content of 3.06%. The results indicate that new elements were introduced to the GnPs.

Table 2.1 | EA data of the pristine **graphite**, **MA-GnPs** and **MI-GnPs**

Sample	C (%)	H (%)	O (%)	N (%)	C/H	C/O	C/N
Graphite	97.71	BDL[a]	BDL	NA[b]	NA	NA	NA
MA-GnPs	86.10	1.07	10.10	NA	6.71	11.37	NA
MI-GnPs	84.97	1.21	8.91	3.06	5.85	12.72	32.40

a. BDL = Below detection limit.

b. NA = Not applicable.

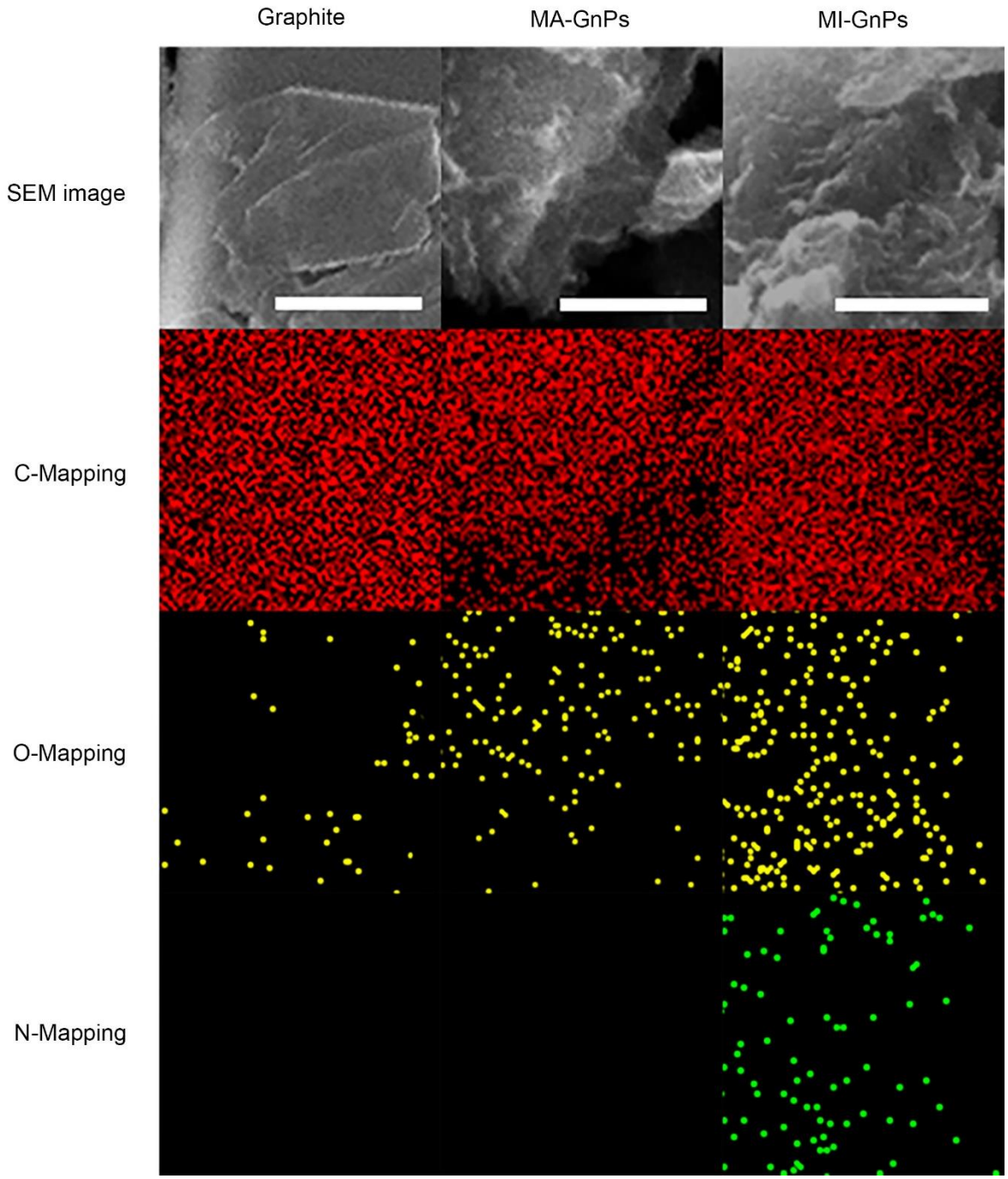

Figure 2.3 | Energy dispersive spectrometer (EDS) of pristine graphite, MA-GnPs and MI-GnPs. SEM images and their corresponding carbon, oxygen and nitrogen mappings in that order: Scale bars are 1 μm. Nitrogen was only observed in MI-GnPs.

Table 2.2 | XPS and EDS data of the pristine **graphite**, **MA-GnPs** and **MI-GnPs**

Sample		C (%)	O (%)	N (%)	C/O	C/N
Graphite	XPS (at%)	98.68	1.32	NA[a]	99.68	NA
	EDS (at%)	99.00	1.00	NA	132	NA
MA-GnPs	XPS (at%)	89.47	10.53	NA	11.33	NA
	EDS (at%)	91.14	8.86	NA	13.72	NA
MI-GnPs	XPS (at%)	87.99	9.05	2.96	12.96	34.68
	EDS (at%)	88.22	5.18	6.59	22.71	15.62

The sole presence of nitrogen in MI-GnPs was further confirmed by SEM element mapping with an energy dispersive spectrometer (EDS) of the samples (Figure 2.3 and Table 2.2). Although MA and MI have similar structures (Figure 2.2), the resultant MA-GnPs and MI-GnPs are expected to possess different properties owing to the differences in the chemical nature of the final structures. After stirring in 1 M aq. HCl solution to eliminate residual metallic impurities, if any, and further Soxhlet extraction with water (see Experimental section), the anhydride moieties at the edges of MA-GnPs were expected to be hydrolyzed into carboxylic acids, while the imide rings of MI-GnPs are relatively stable and thus remain intact.[85,86] Consequently, the difference in polarity between open shaped carboxylic acids and close-shaped imide rings should display different dispersibility in polar solvents (*vide infra*).

2.3.2 Characterization of MA-GnPs and MI-GnPs

To further quantitatively and qualitatively identify Diels-Alder reaction adducts, thermogravimetric analysis (TGA), Fourier transform infrared (FT-IR) and X-ray photoelectron spectroscopy (XPS) were used.

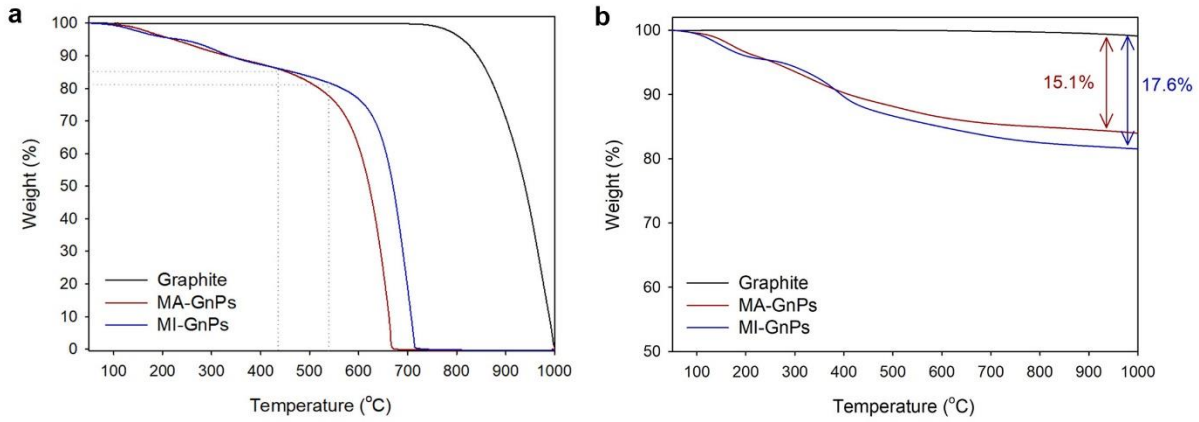

Figure 2.4 | TGA thermograms of MA-GnPs and MI-GnPs. The samples were heated at 10 °C min^{-1} in **a**, air; **b**, nitrogen.

Compared with pristine graphite, the TGA thermograms of MA-GnPs and MI-GnPs obtained show that gradual weight loss started from the beginning and the measured values were approximately 14% and 18% at around 435 °C and 540 °C in air, respectively (Figure 2.4a). The char yields of MA-GnPs and MI-GnPs were 15.1% and 17.6%, respectively, at 1000 °C in nitrogen (Figure 2.4b). The early gradual weight loss of EFGnPs is attributed to the thermal decomposition of edge functional groups.[82] Based on the results, we can simply assume the amount of functional groups at the edge of graphene nanoplatelets by measuring the char yield at nitrogen atmosphere. However, these values are slightly lower than the weight loss estimation of MA-GnPs and MI-GnPs; MA-GnPs (1.45/6.45 × 100% = 22%), MI-GnPs (2.09/7.09 × 100% = 29%). The main reason is due to the regeneration of graphitic structure during pyrolysis. Edge-dienenophile moieties (*i.e.*, MA- and MI-) cannot be cleanly stripped off by heat-treatment, because some portions are pyrolyzed into graphitic char under inert nitrogen condition. As a result, higher char yields at 1000 °C than theoretical ones are expected. Although some other minor reasons cannot be ruled out, we believe that the reason is major contributions to the gap between weight gains by the reaction and weight losses by TGA.

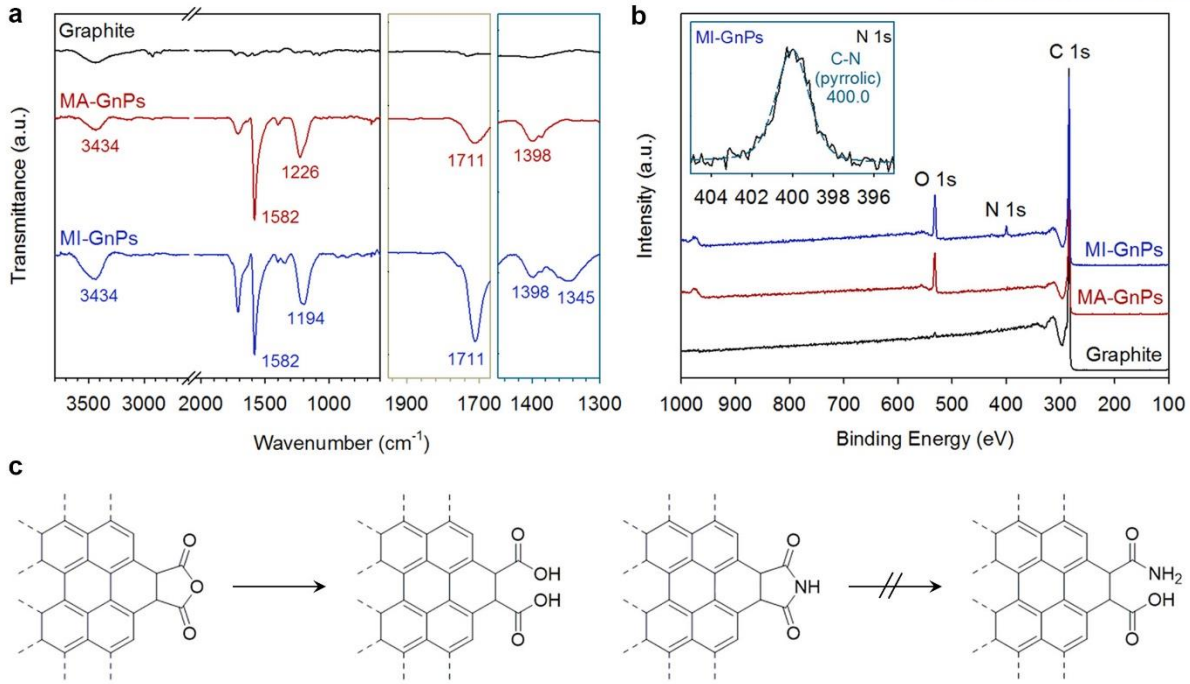

Figure 2.5 | Structural characterization of MA-GnPs and MI-GnPs. **a**, Full FT-IR spectra (KBr pellets) (left); magnification of the fingerprint region between 1650 cm^{-1} and 1950 cm^{-1} showing the signals of the characteristic C=O stretching vibration (middle); magnification of the fingerprint region between 1300 cm^{-1} and 1470 cm^{-1} showing the signals of the characteristic C–N stretching vibration (right). **b**, XPS survey spectra. Inset: high-resolution XPS N 1s spectrum of MI-GnPs. **c**, schematic representation of the edge moieties of MA-GnPs (left) and MI-GnPs (right) after acid-mediated work-up procedures. Anhydride groups on MA-GnPs are prone to hydrolyze into carboxylic acid groups because of the water. However, the maleimide rings on MI-GnPs remain intact. Imide groups tend to hydrolyze into amic acid groups at basic media.

The types of functional groups at the edges of the resultant EFGnPs can be confirmed by FT-IR spectroscopy and XPS. While pristine graphite shows an almost featureless FT-IR spectrum (Figure 2.5a), MA-GnPs and MI-GnPs display a strong band at 1580 cm^{-1}, which is attributable to the C=C stretching band at the edges of EFGnPs. Both samples also exhibit similar bands at around 1200 and 3400 cm^{-1}, respectively, corresponding to C–O and O–H stretching attributed to carboxylic or hydroxyl groups at the edges. In the case of MI-GnPs, overlapping between O–H and N–H stretching may occur at around 3400 cm^{-1}. MA-GnPs and MI-GnPs have the same band, which appears at 1711 cm^{-1} and is attributed to C=O stretching. N–H bending overlapped with C=O stretching. In addition, MI-GnPs display a small band at 1345 cm^{-1}, which is attributed to C–N stretching from maleimide ring moieties at the edges. The results suggest that anhydride groups (mostly C=O stretching in anhydride appears at 1830 cm^{-1}) on MA-GnPs are hydrolyzed into carboxylic acids,[87] whereas the maleimide rings on MI-GnPs remain intact during acid-mediated work-up procedures.[85,86](Figure 2.5c)

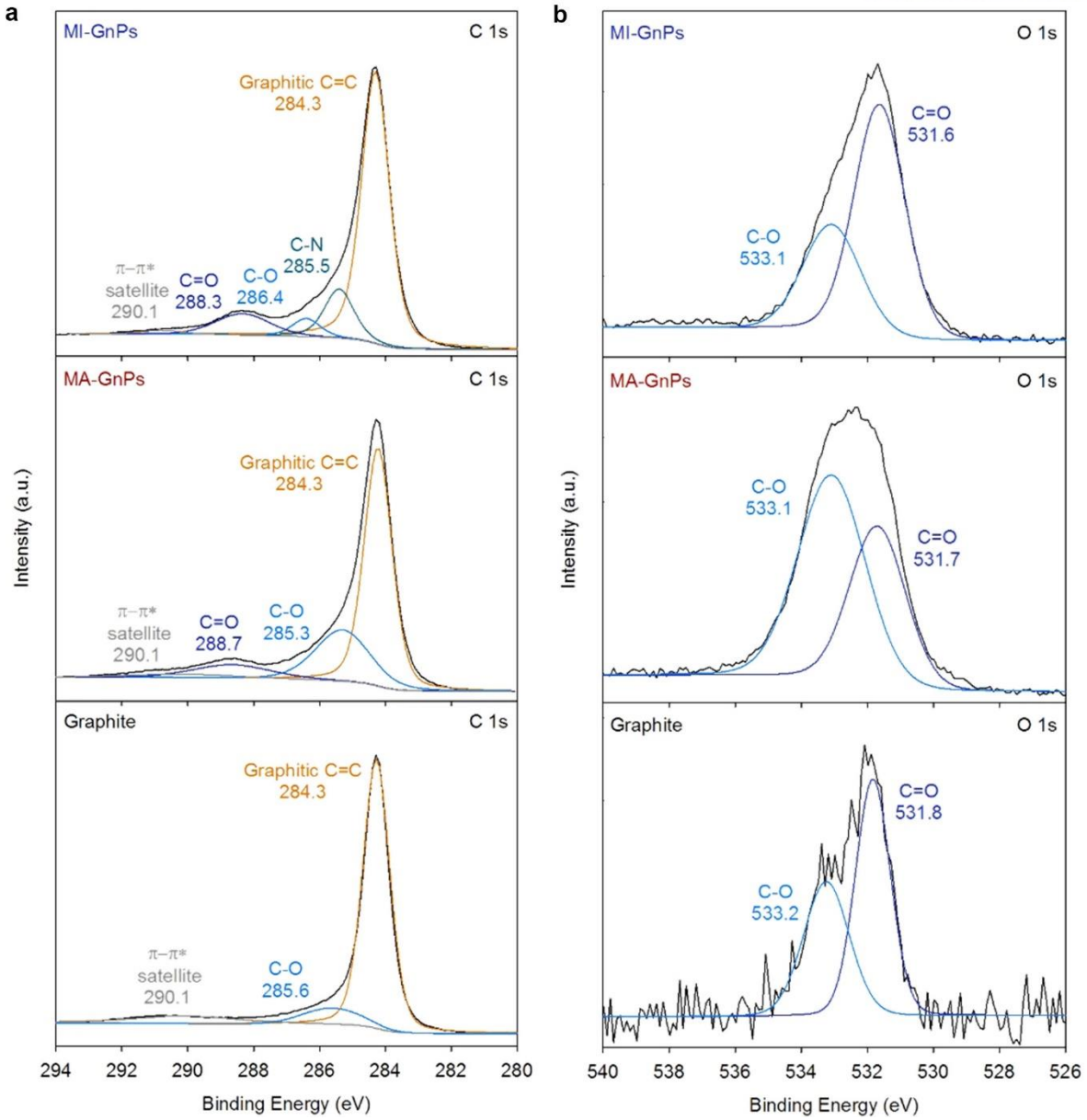

Figure 2.6 | High resolution XPS spectra. **a**, C 1s spectra of pristine graphite, MA-GnPs and MI-GnPs. **b**, O 1s spectra of pristine graphite, MA-GnPs and MI-GnPs.

For more detailed analysis, both EFGnPs were further examined by XPS (Figure 2.6 and Table 2.2). While pristine graphite shows a very minor O 1s peak at 532 eV relative to the C 1s peak at 284 eV due to physically adsorbed oxygen,[88,89] MA-GnPs and MI-GnPs display relative strong O 1s peaks owing to the edge functional groups (Figure 2.5b). The high-resolution XPS surveys with curve fitting of O 1s spectra of both MA-GnPs and MI-GnPs reveal that the O element is assignable to C–O and C=O bonding (Figure 2.6), which are associated with C–OH, O=C–OH, and O=C–N–C=O moieties. Once again, the N 1s peak at 400 eV, which corresponds to pyrrolic-N of the imide ring (inset, Figure 2.5b),[90,91] was only observed with MI-GnPs.

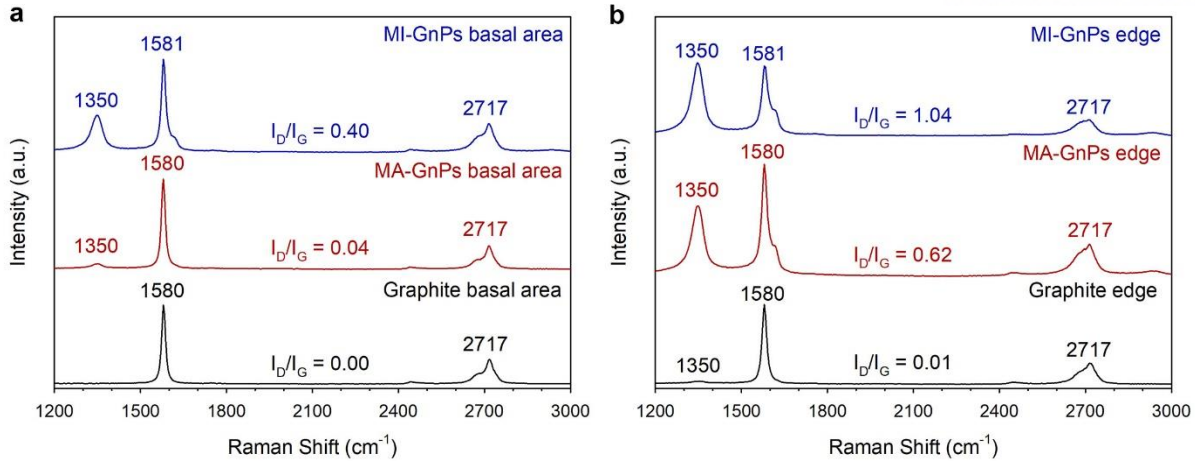

Figure 2.7 | **Raman spectra obtained by a focused laser**: **a**, edge area and **b**, basal area.

The Raman spectra of edge-selective [4 + 2] cycloadditions via ball-milling graphite in the presence of dienophile which exclusively occurred at the edges were obtained from the edges and basal areas of samples with a focused laser beam. The Raman spectrum obtained from the edge area of pristine graphite shows a strong G band at 1580 cm^{-1} and a 2D band at 2717 cm^{-1} with a very weak D band at 1350 cm^{-1} (Figure 2.7a), indicating a highly ordered structure with low defects. Pristine graphite has the ratio of the D- to G-band intensities (I_D/I_G) of only 0.01. However, MA-GnPs and MI-GnPs have much stronger D-bands at 1350 cm^{-1}, stemming from a high degree of edge distortion by functionalization along with size reduction. As a result, the I_D/I_G ratios of MA-GnPs and MI-GnPs are 0.62 and 1.04, respectively. The Raman spectrum obtained from the basal area of the starting graphite shows strong G and 2D peaks without a detectable D peak, whereas those of MA-GnPs and MI-GnPs have detectable D peaks.[92] (Figure 2.7b). However, the I_D/I_G ratios of MA-GnPs and MI-GnPs were 0.04 and 0.40, respectively, which are relatively much lower than those obtained from edge areas. Note that the grain sizes of both EFGnPs are significantly smaller than pristine graphite as seen in Figure 2.1b-d. The relatively smaller D-bands from MA-GnPs and MI-GnPs are most likely contributed by edges, because the wavelength (532 nm) of the Raman laser is similar to the grain sizes of EFGnPs.[93] Thus, the Raman results indicate that the [4 + 2] cycloadditions almost exclusively occurred at the edges of EFGnPs.

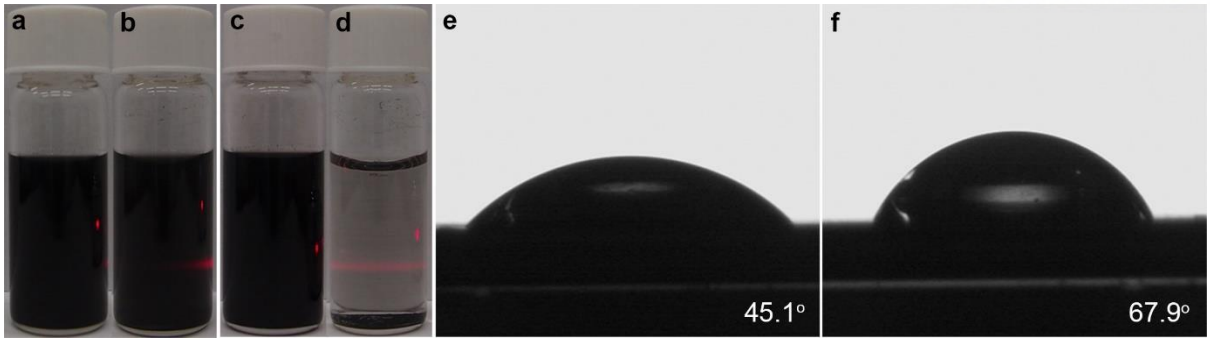

Figure 2.8 | Dispersibility of MA-GnPs and MI-GnPs. **a**, **b**, Photographs of sample dispersion in ethanol after 3 months standing under normal laboratory conditions: (**a**) MA-GnPs and (**b**) MI-GnPs. Concentration is 0.3 mg ml^{-1}. **c**, **d**, Photographs of sample dispersion in water after 3 months standing under normal laboratory conditions: (**c**) MA-GnPs and (**d**) MI-GnPs. Concentration is 0.3 mg ml^{-1}. **e**, **f**, Contact angle images of samples: (**e**) MA-GnPs and **(f)** MI-GnPs.

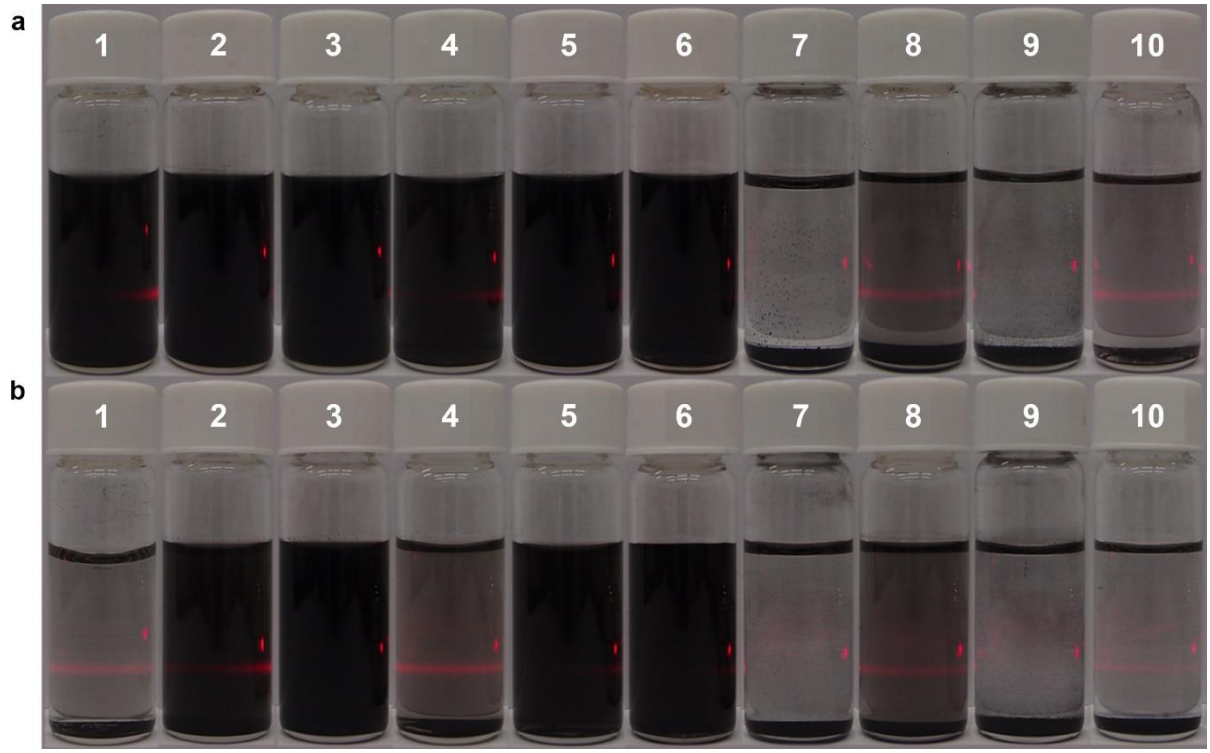

Figure 2.9 | Photographs of EFGnPs dispersed solution in various solvents after 3 months standing on bench top in a normal laboratory conditions: **a**, MA-GnPs; **b**, MI-GnPs: (1) DI-water; (2) methanol; (3) ethanol; (4) acetone; (5) dimethylformamide; (6) 1-methyl-2-pyrrolidone; (7) toluene; (8) 1,2-dichlorobenzene; (9) hexane; (10) dichloromethane. Concentrations are 0.3 mg ml^{-1}.

Table 2.3 | Contact angles of **MA-GnPs** and **MI-GnPs**

No.	MA-GnPs	MI-GnPs
1	44.1	66.4
2	45.0	67.2
3	45.1	67.9
4	45.3	68.5
5	45.9	68.7
Average	45.08	67.74

The edge-functionalization of GnPs is expected to lead to improved dispersibility due to the edge functionality (enthalpic gains) and size reduction (entropic gains), which should provide the thermodynamic driving force for dispersion in various solvents. Thus, EFGnPs can disperse well in most protic and polar aprotic solvents, including neutral water.[83] For example, both EFGnPs show good dispersibility in ethanol (Figure 2.8a and b) and other protic and polar aprotic solvents (Figure 2.9). However, they display clearly different dispersion stability in H_2O, as shown in Figure 2.8c and d, indicating that MA-GnPs have better dispersion stability than MI-GnPs in water. It is likely due to the hydrogen bonding between water molecules and carboxylic acid groups at the edges of MA-GnPs. The variation in dispersibility supports the hydrolysis of anhydride into carboxylic acids in MA-GnPs. For further evidence, contact angle measurements could distinguish the differences between the surface polarities of MA-GnPs and MI-GnPs, which were performed by placing droplets of de-ionized water on EFGnP-coated silicon substrates. MA-GnPs show a lower water contact angle (45.1°) (Figure 2.9e) than MI-GnPs (67.9°) (Figure 2.9f), indicating the higher surface polarity of MA-GnPs (Table 2.3).

2.4 Conclusion

In summary, for the first time, we have demonstrated the solid-state Diels-Alder reaction of graphite. Mechanochemical ball-milling breaks the graphitic C–C bonds and generates active carbon species (mostly carboradicals, carboanions and carbocations), which couple with a dienophile, such as maleic anhydride or maleimide. Owing to the acid-mediated work up process, the anhydride moieties on MA-GnPs are hydrolyzed into carboxylic acid, while the imide moieties on MI-GnPs remain intact. The resultant edge-selectively functionalized graphene nanoplatelets were readily dispersible in various solvents. Hence, considering the availability of dienophiles, the Diels-Alder reaction *via* ball-milling graphite could be a general method for the chemical modification of graphite into graphene nanoplatelets.

Chapter 3 A SOLVENT-FREE DIELS-ALDER REACTION OF GRAPHITE INTO FUNCTIONALIZED GRAPHENE NANOSHEETS †

† Chapter III is reproduced in part with permission of "Seo, J.-M. and J.-B. *Chem. Commun..,* **2014**, 50, 14651". Copyright 2014 The Royal Society of Chemistry

3.1 Introduction

Since the advent of new carbon materials, various attempts to manipulate their properties are constantly conceived. One of the most viable methods is chemical modification, which is the incorporation of functional group(s) by means of covalent or non-covalent bonds. By tuning their intrinsic properties using chemical modification methods, carbon nanomaterials offer a great number of potential applications.[19,94] However, given the chemical inertness arising from their fully conjugated aromatic network structure, carbon nanomaterials are known to be difficult for functionalization.[95] Thus, highly reactive chemical species or harsh reaction conditions are required to overcome the large reaction barrier, such as oxidation using a strong acid[35,96] or the addition of radicals.[97,98]

To date, several chemical approaches have been developed for modifications of carbon nanomaterials. A promising approach is cycloaddition[99] owing to the flexibility of the reaction procedure involved and it yields a variety of desirable functional groups. Therefore, numerous studies have been reported on the cycloaddition of fullerenes,[100] carbon nanotubes,[101] and the more recently graphene.[19] Among them, the Diels-Alder reaction, *i.e.*, [4 + 2] cycloaddition on graphene, was experimentally demonstrated by Haddon's group based on the concept of the dual behaviour of graphene as either a diene or a dienophile.[61,79] Following their experimental results, Houk[102] and Denis[103] computationally predicted the reaction sites of graphene for Diels-Alder reactions. Regarding the chemistry involved, it is commonly acceptable that organic solvents are necessary to dissolve all the reactants, allowing them to collide and then react with each other.[104] However, this principle does not apply for the chemistry of carbon nanomaterials. Most carbon nanomaterials are known to be thermodynamically insoluble in common organic solvents, whereas they form kinetically stable suspensions in amide solvents such as dimethylformamide (DMF) or N-methyl-2-pyrrolidone (NMP). Also solvent dispersed graphene tends to reaggregate to form thermodynamically stable layered structure. In other words, solvents are not always helpful for the functionalization of carbon nanomaterials. Hence, to explore their reactivity in the absence of a solvent is highly challenging.[105,106]

In this communication, we demonstrate a solvent-free Diels-Alder reaction of graphite into functionalized graphene nanosheets using two different dienophiles as an alternative to the solvent-assisted approach. To increase the reaction feasibility conceptually, maleic anhydride (MA) and maleimide (MI) were chosen as the dienophiles for use in this study, whereas graphite was chosen as a diene. In contrast to our previous work in which a mechanochemical approach was used,[107]

thermodynamically preferred reaction products are obtained here, as the reaction is conducted at a relatively high temperature (160-220 °C) in a sealed glass ampoule of argon. We expected that the resultant maleic anhydride-functionalized graphene nanosheets (MAG) and maleimide-functionalized graphene nanosheets (MIG) could be dispersed well in a polar solvent. Furthermore, the functionalization process induces the delamination of the graphite into graphene nanosheets by dispersing the resultant MAG or MIG in a common organic solvent.

3.2 Experimental

3.2.1 Materials

Graphite (99.9% purity, stock no. 1250HT, CAS no. 7782-42-5, Lot no. 1250-100907) was obtained from Nanostructured & Amorphous Materials Inc., USA, and used as received. Maleic anhydride (FW = 98.06) and maleimide (FW = 97.07) were purchased from Sigma-Aldrich Chemical Inc. and used as received. Solvents were used as received.

3.2.2 Solvent‐free Diels‐Alder reaction of MAG and MIG

A Pyrex glass ampoule was charged with pristine graphite (0.5 g) and maleic anhydride (5 g, 50.98 mmol) or maleimide (5 g, 51.50 mmol). After removing residual air through several vacuum purging/argon refill cycles, the reagents are sealed and allowed to react at 220 °C (MAG) or 160 °C (MIG) for 12 h. The resultant products were collected by filtration using Nylon membrane (0.2 μm), washed with tetrahydrofuran (THF) and further Soxhlet extracted with THF for 24 h. The solvent was removed under a reduced pressure (0.5 mmHg) at −120 °C for 72 h to give 0.502 g of MAG and 0.501 g of MIG as a dark-black powder.

3.2.3 Physical characterization

The morphology of the samples was examined by field-emission scanning electron microscopy equipped with an energy dispersive spectrometer (FE-SEM, FEI Nanonova 230). Samples were deposited onto a conductive carbon tape without coating and imaged at 10 kV without tilting. High-resolution transmission electron microscopy (HR-TEM) was carried out on a JEOL JEM-2100F microscope operating at 200 kV. The samples were suspended in N-methyl-2-pyrrolidone and drop-cast onto a lacey carbon film. Themogravimetric analysis (TGA) was conducted on a TA Q600 (TA Instrument) under air at a heating rate of 10 °C min^{-1}. Raman spectra were recorded using an Alpha 300S confocal Raman spectrometer (WITec, Germany) with a 532 nm He-Ne laser. Fourier transform infrared (FT-IR) spectra were recorded on a Perkin-Elmer Spectrum 100 using KBr pellets. X-ray photoelectron spectra (XPS) were recorded on a Thermo Fisher K-alpha XPS spectrometer.

3.3 Results and Discussion

3.3.1 Solvent-free Diels-Alder reaction of graphite in closed system

The solvent-free Diels-Alder reactions were performed in a closed and sealed system using a glass ampoule of argon (Scheme 3.1).

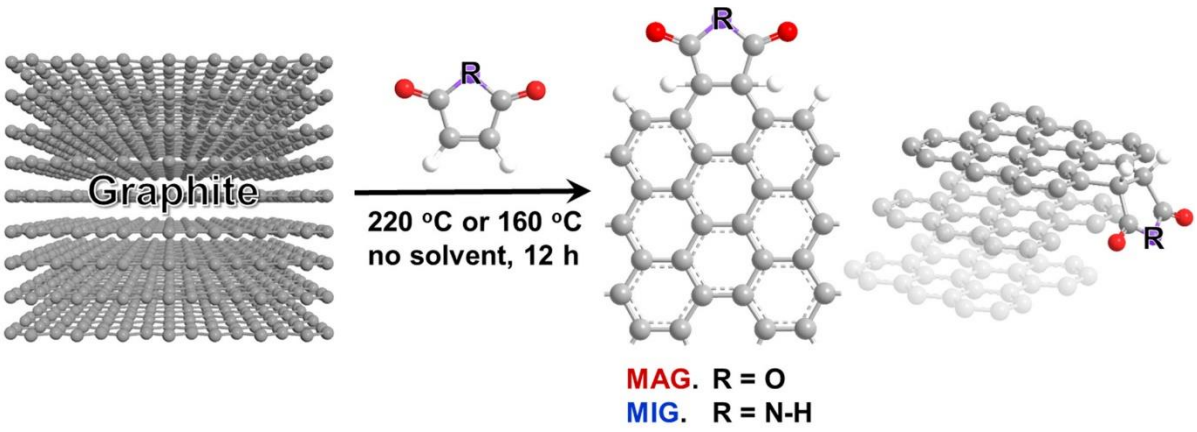

Scheme 3.1 | Schematic representation of the solvent-free Diels-Alder reaction of graphite in the presence of a specific dienophile, maleic anhydride (MA) or maleimide (MI). Each dienophile can act both as a solvent as well as a reactant at an appropriated temperature. The red spheres denote the oxygen.

It should be noted that graphite is a stable material, which, in turn, implies that it has poor reactivity. To facilitate the Diels-Alder reaction, we carried out the reaction at a relatively high temperature (160-220 °C). While conducting the reaction in an open process, MA or MI melted and evaporated, and condensed above the heated zone thus lowering the reactivity and the reaction yield. Therefore, we utilized a solvent-free procedure using a sealed tube. After the reaction was complete, the products were Soxhlet-extracted with tetrahydrofuran (THF) to remove the unreacted dienophile completely, after which the resultant products were freeze-dried at a reduced pressure and characterized. In both cases, the mass of the product was greater than the mass of the starting graphite (Experimental details).

3.3.2 Morphology and functionalization density characterization

The functionalization of graphene is expected to improve the dispersibility due to the polar functional groups. This prediction is easily confirmed by dispersing the functionalized graphene nanosheets in a polar solvent. For example, MAG and MIG show good dispersibility in NMP, while graphite completely settled down after one month under the same conditions (insets in Figure 3.1a-c). Upon exposure to a laser beam, the Tyndall scattering effect was observed for both MAG and MIG. This phenomenon indicates that both MAG and MIG have effective functional group which is able to be dispersed in NMP,

so that leads to delamination from functionalized graphite to functionalized graphene nanosheets.

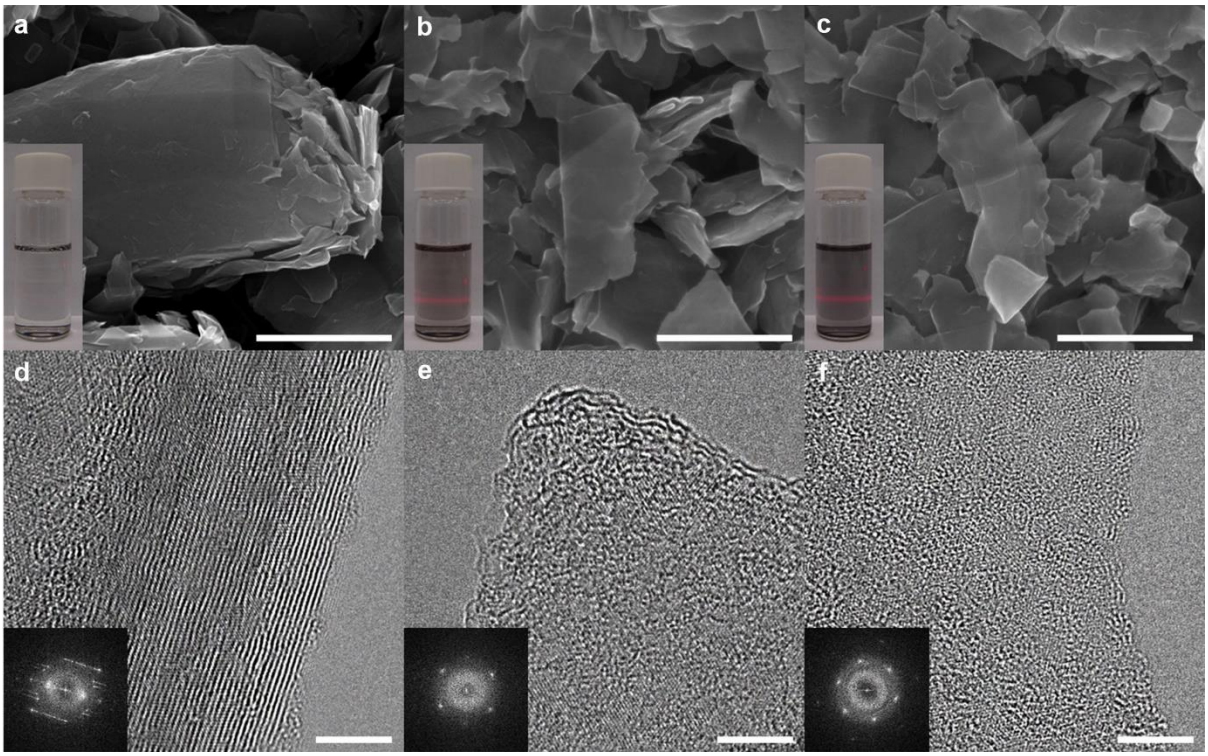

Figure 3.1 | **Morphologies of functionalized graphene nanosheets**. **a-c**, SEM images: (**a**) pristine graphite, (**b**) MAG, and (**c**) MIG. Scale bars are 1 μm. Insets in each case are photographs of the sample dispersion in NMP after standing for 1 month under normal laboratory conditions. The concentration is 0.5 mg ml^{-1}. **d-f**, HR-TEM images: (**d**) pristine graphite, (**e**) MAG, and (**f**) MIG. Scale bars are 5 nm. Insets are SAED patterns of each respective sample.

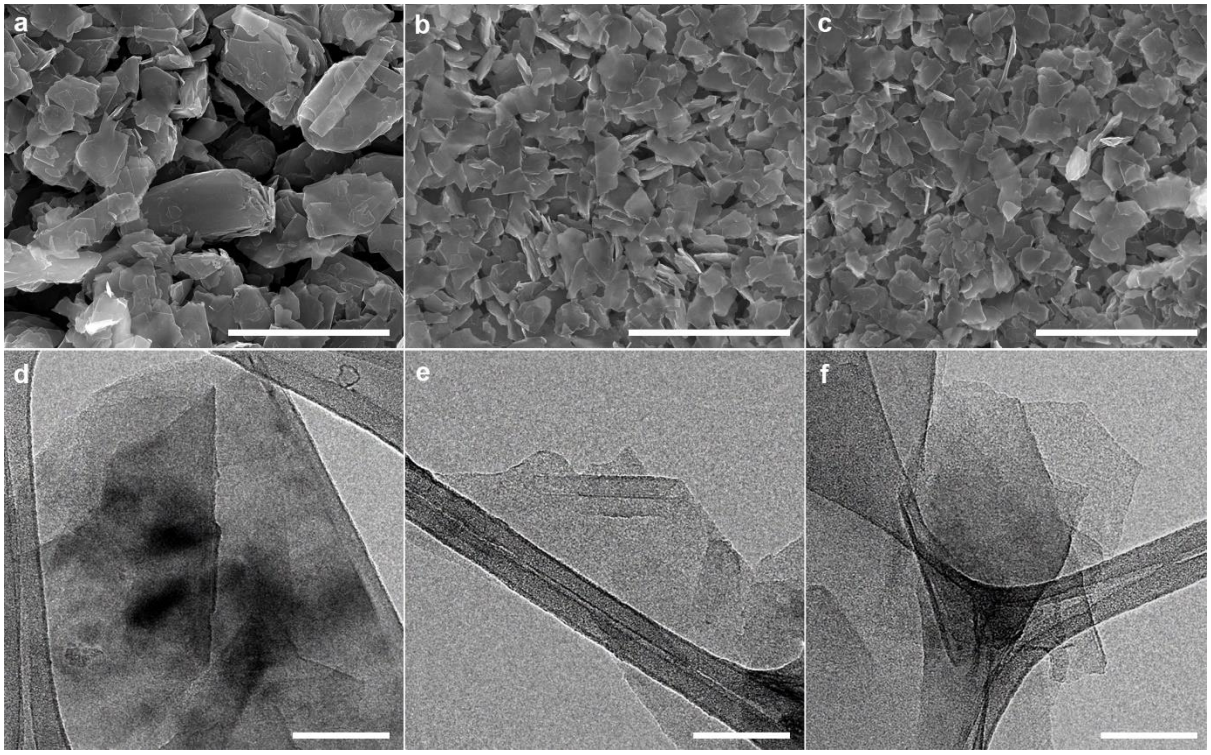

Figure 3.2 | **Microscopy images of functionalized graphene nanosheets. a-c**, Low- magnification SEM image: (**a**) pristine graphite, (**b**) MAG, and (**c**) MIG. Scale bars are 2 μm. **d-f**, Low-magnification HR-TEM images: (**d**) pristine graphite, (**e**) MAG, and (**f**) MIG. Scale bars are 100 nm.

The morphologies of the dispersed solutions were compared by means of scanning electron microscopy (SEM) and transmission electron microscopy (TEM). As shown in Figure 3.1 and Figure 3.2, the grain size is reduced to approximately 1 μm compared to pristine graphite. Unlike the graphite (Figure 3.1a), the morphologies of MAG and MIG show two-dimensional transparent sheets stacked onto each other (Figure 3.1b and c), indicating the efficient functionalization and exfoliation of graphite into a few layers of graphene nanosheets. The exfoliation was further confirmed by TEM analysis (Figure 3.1 and 3.2). Compared to pristine graphite (Figure 3.1d), MAG (Figure 3.1e) and MIG (Figure 3.1f) clearly show a few layers of sheets. These results indicate that functionalization induces further delamination of MAG and MIG in a solution to form fewer graphitic layers. Furthermore both MAG and MIG show clear six-fold selected area electron diffraction (SAED) pattern, implying the functionalization take place not at the basal position but at the edge position of functionalized graphene nanosheets.

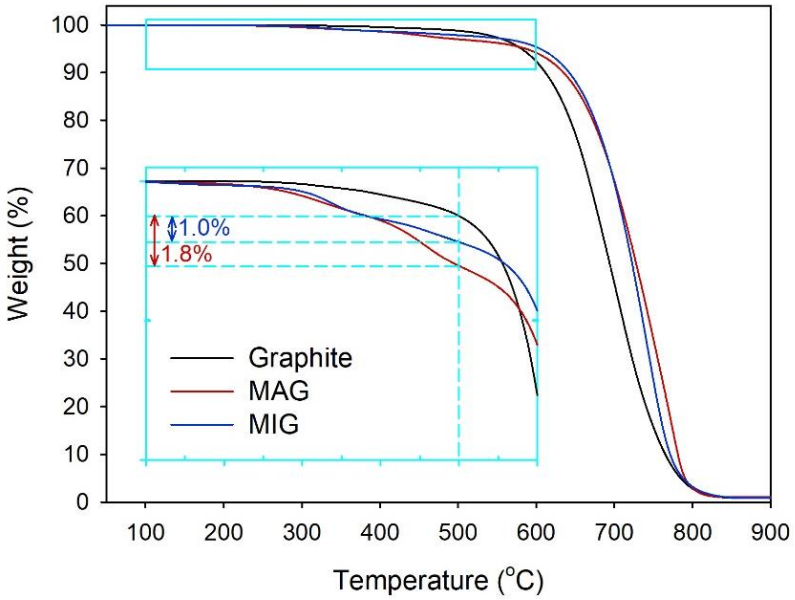

Figure 3.3 | TGA thermograms obtained from the heating rate of 10 °C min^{-1} in air. Inset is magnified thermograms range from 100 to 600 °C.

It has been reported that graphene can function as either a diene or a dienophile in a Diels-Alder reaction.[79] Because we use two dienophiles (MA and MI) as the 2p component here, graphite should function as a 4p component. Therefore, the reaction is expected to occur at the basal plane and the peripheral positions, especially at the armchair edges. According to the computational prediction reported by Houk's group,[102] the basal plane of graphene cannot be functionalized, and functionalization occurs only at the armchair edges. The limited number of functionalization sites, therefore, could influence the degree of functionalization. Thus, we performed thermogravimetric analysis (TGA) to identify the degree of functionalization by thermally stripping off the MA and MI moieties from MAG and MIG, respectively. Compared to pristine graphite, the TGA thermograms of MAG and MIG (Figure 3.3) obtained in an air atmosphere displays a gradual weight loss starting at approximately 200 °C, with the weight losses of MAG and MIG being approximately 2 and 1 wt%, respectively, at around 500 °C in air. The degree of functionalization is way too little compared with our previous reports (see Figure 2.4 in Chapter 2) although all reaction proceeded same mechanism. These results provide that mechanochemical approach by ball-milling is more powerful solvent-free Diels-Alder reaction than common thermodynamically preferred reaction.

3.3.3 Structural characterization

To investigate the structural information of MAG and MIG further, the Raman spectra (Figure 3.4) were obtained from powdered samples. While pristine graphite has the D- to G-band intensity level (I_D/I_G) ratio of 0.20, MAG and MIG have stronger intensity ratios of 0.54 and 0.52, respectively, which is

indicative of a structural defect induced by covalent functionalization.

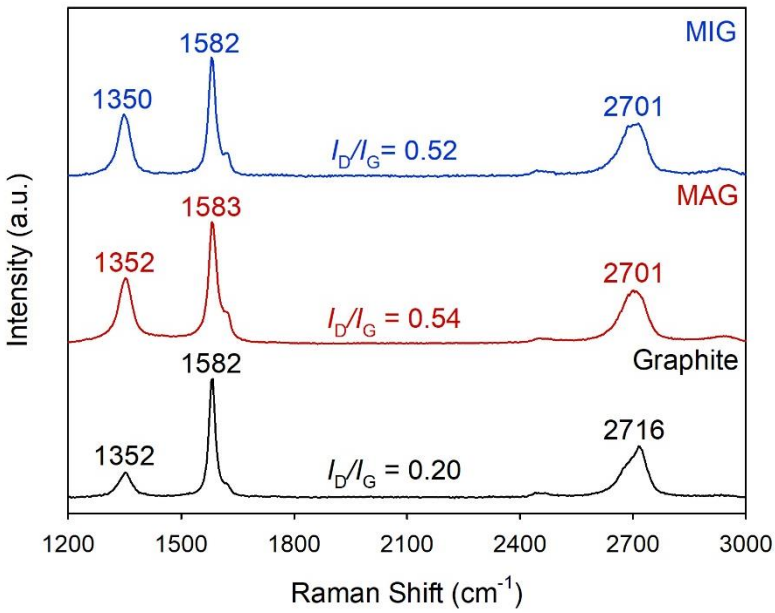

Figure 3.4 | Raman spectra obtained by a focused laser.

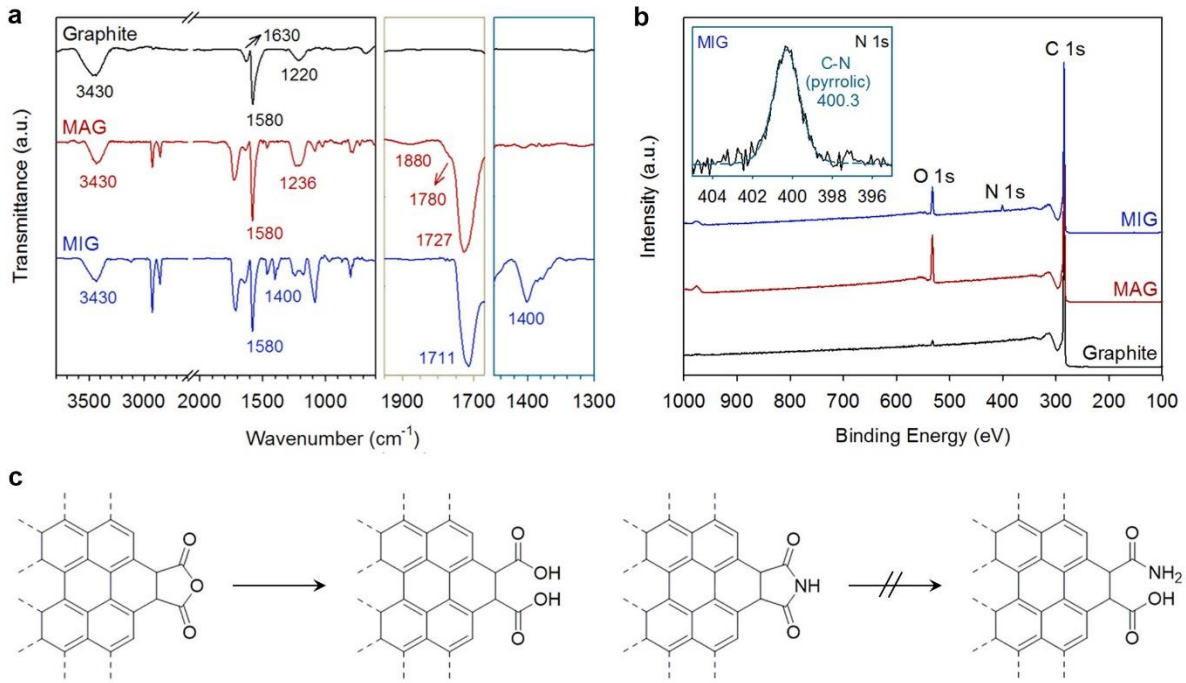

Figure 3.5 | **Structural characterization of MAG and MIG. a**, Full FT-IR spectra (KBr pellets) (left); magnification of the fingerprint region between 1650 cm^{-1} and 1950 cm^{-1} showing the signals of the characteristic C=O stretching vibration (middle); magnification of the fingerprint region between 1300 cm^{-1} and 1470 cm^{-1} showing the signals of the characteristic C–N stretching vibration (right). **b**, XPS survey spectra. Inset: high-resolution XPS N 1s spectrum of MIG. **c**, schematic representation of the edge moieties of MAG (left) and MIG (right) after work-up procedures. Anhydride groups on MAG are

prone to hydrolyze into carboxylic acid groups because of the small amount of water in THF. However, the maleimide rings on MIG remain intact. Imide groups tend to hydrolyze into amic acid groups at basic media.

The types of functional groups of the resultant MAG and MIG can be confirmed by Fourier transform infrared (FT-IR) spectroscopy and X-ray photoelectron spectroscopy (XPS). Pristine graphite shows a strong C=C stretching band at 1580 cm^{-1} and shows other minor bands as well due to the physically adsorbed oxygen (1220 cm^{-1}) and moisture (1630, 3430 cm^{-1}).[108] On the other hand, MAG and MIG display a decisive difference from the graphite. The first is the presence of strong bands at approximately 2800 and 2900 cm^{-1}, corresponding to sp^3 C–H stretching attributed to the Diels-Alder reaction.[79] The second difference results from the carbonyl (C=O) functionality of MAG and MIG. MAG exhibits a strong C=O band at around 1730 cm^{-1}, corresponding to the carboxylic acid moieties, and a weak band at 1780 and 1880 cm^{-1}, which is attributed to the anhydride moieties (Figure 3.5, middle) (mostly the anhydrides show two stretching bands for C=O groups; the results are from the asymmetrical (1860 cm^{-1}) and symmetrical (1780 cm^{-1}) C=O stretching modes.[109]). These results suggest that anhydride groups on MAG are mostly hydrolyzed into carboxylic acid. MIG also has strong C=O stretching or overlapped N–H bending from the imide ring moieties at 1711 cm^{-1}, with a weak C–N band at 1400 cm^{-1}, which is identical to that in maleimide. As a result, the functionality of MIG retains its maleimide moieties compared to the MAG functionalities, which were mostly hydrolyzed into carboxylic acid.

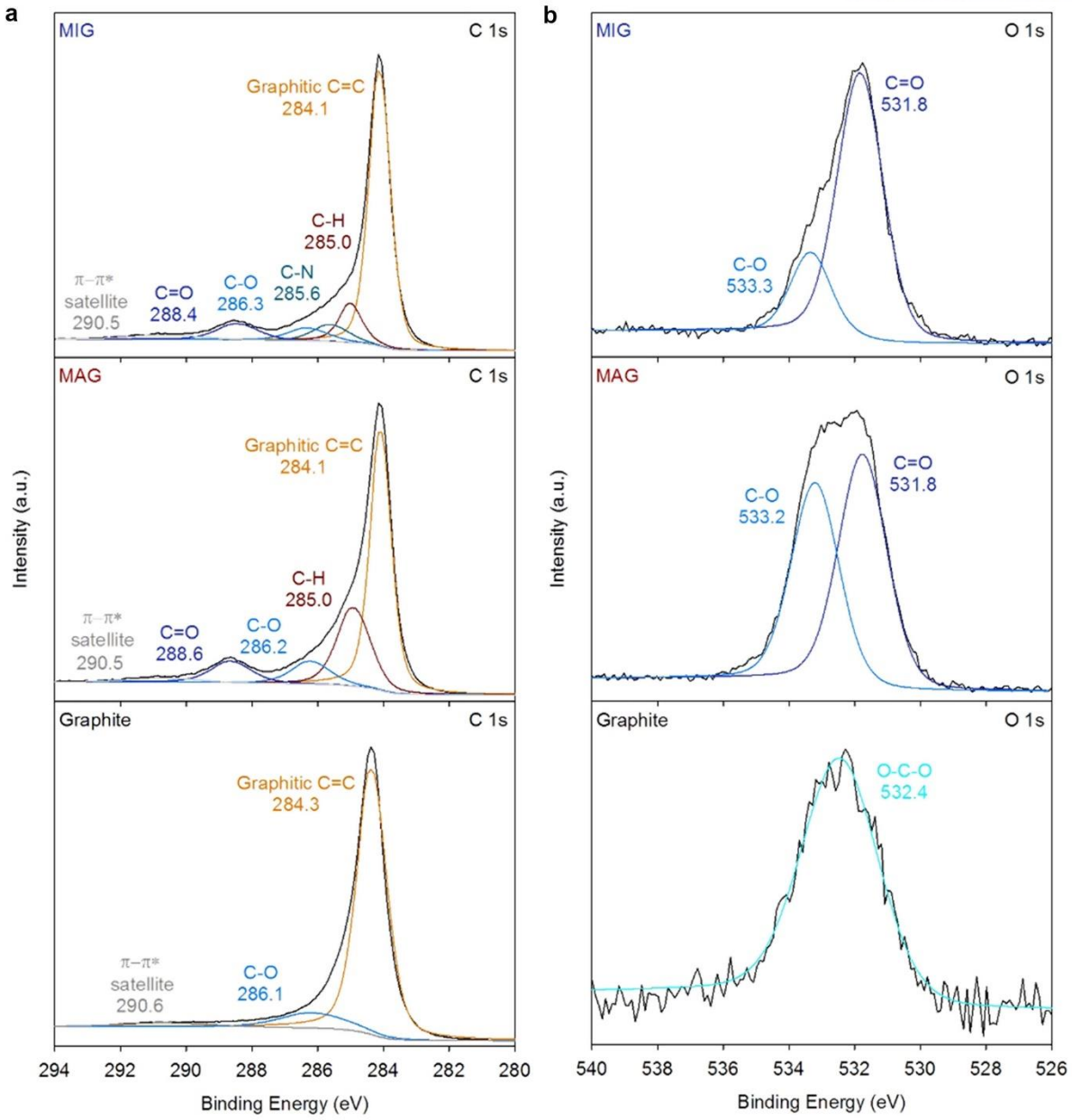

Figure 3.6 | **High resolution XPS spectra**. **a**, C 1s spectra of pristine graphite, MAG and MIG. **b**, O 1s spectra of pristine graphite, MAG and MIG.

Table 3.1 | XPS elemental composition of pristine **graphite**, **MAG** and **MIG**

	C (at.%)	O (at.%)	N (at.%)	C/O	C/N	Total
Graphite	98.16	1.84	NA[a]	53.35	NA	100
MAG	88.16	11.84	NA	7.45	NA	100
MIG	90.96	6.98	2.05	13.03	44.37	100

For more detailed information into the characteristics of the bonds, both MAG and MIG were further examined by XPS. Pristine graphite exhibits a very minor O 1s peak at 532 eV relative to the C 1s peak at 284 eV due to the physically adsorbed oxygen.[108] MAG and MIG display much stronger O 1s peaks than pristine graphite owing to the MA and MI functional groups (Figure 3.5b and Table 3.1). The deconvoluted high-resolution XPS spectra in the C 1s region of MIG (Figure 3.6) show one distinctive peak at 285.6 eV, which is attributed to C–N bonding of MI moieties. In the case of the O 1s region, MAG (Figure 3.6) shows one broad peak at around 532 eV, which is assignable to C–O and C=O bonding of the MA moieties. MIG also shows two oxygen peaks. Based on the general structure of MI, a single oxygen signal is expected for the carbonyl groups in the imide ring. Beside the main carbonyl peak located at 531.8 eV, an additional oxygen peak at 533.3 eV in the range of the C–O bond (Figure 3.6) was noted. Similar phenomena have been reported in imide-functionalized carbon materials.[110] While peak asymmetry was observed in the O 1s envelope, a single N 1s signal was observed only at 400.3 eV, which corresponds to the pyrrolic-N of the imide ring (Figure 3.5b, inset). Thus, we can conclude that, once again, the MI rings on MIG remain intact during work-up procedures.

3.4 Conclusion

We have, for the first time, demonstrated a solvent-free Diels-Alder reaction of graphite using two different dienophiles, maleic anhydride and maleimide. After Soxhlet extracted work-up process, the anhydride moieties on MAG are mostly hydrolyzed into carboxylic acid because of the water in THF, while the imide moieties on MIG remain intact. The covalent functionalization of graphite could be a driving force for its delamination into graphene nanosheets through dispersion in a polar solvent such as DMF or NMP. Therefore, the solvent-free covalent functionalization of graphite *via* the Diels-Alder reaction is not only a simple but an efficient approach for the scalable preparation of graphene nanosheets.

Chapter 4 A CRYSTALLINE IMINE-LINKED 2D COVALENT ORGANIC FRAMEWORK

4.1 Introduction

Covalent organic framework (COFs) are a new class of porous crystalline materials composed of lightweight elements such as boron, carbon, nitrogen and oxygen.[24] COFs are made by combination of molecular building blocks covalently linked into extended structures, based on reticular chemistry, which makes them low dense and robust materials. To date, COFs containing boronate ester, boroxine, borazine, triazine, imine, hydrazine, azine and imide linkages have been developed.[20,21] Although COFs constructed from B-O linkage have been well developed, their weak chemical stability leads to rapid decomposition upon exposure to moisture and limits their effective usage in gas storage material under ambient conditions.[111,112] The recently developed COFs composed of the C-N linkage have overcome this limitation and are found to have enhanced chemical stability.[113] However, the reported imine-linked COFs typically possess moderate specific surface areas and mesoporous pores due to its relatively large pore beyond micropores. Therefore, the design for new COFs with excellent porosity, high specific surface area and small pore size for gas storage is highly desired.

Here we introduce a new imine-linked covalent organic framework, which has been synthesized *via* a condensation reaction between 1,3,5-triamino-2,4,6-benzenetriol (TATHB) and terephthaldehyde (TPA). To enhance its reactivity and crystallinity, we used specific triamine building block by incorporating hydroxy groups. The resultant COF has high crystallinity and microporosity. The COF is thermally stable up to 500 °C.

4.2 Experimental

4.2.1 Materials

Unless stated otherwise, all reactions were performed in oven dried glassware under ambient atmosphere. 1,3,5-Triamino-2,4,6-benzenetriol was synthesized according to published methods.[114,115] Palladium on carbon (10 wt%), terephthaldehyde, benzaldehyde, 1,4-dioxane, 1-butanol and ethyl alcohol were purchased from Sigma-Aldrich and used as received. 1,2-Dichlorobenzene was purchased from Alfa Aesar. 2-Aminophenol was purchased from Acros Organics and used as received. 1,3,5-Trimethylbenzene was purchased from TCI Chemical. Methyl alcohol was purchased from Honeywell International Inc. Acetic acid was purchased from OCI chemicals.

4.2.2 Synthesis of 1,3,5-triamino-2,4,6-benzenetriol trihydrochloride

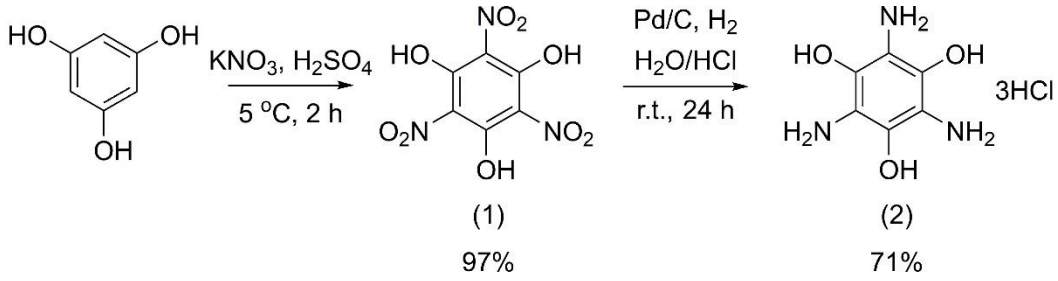

(1) 97%

(2) 71%

Scheme 4.1 | Schematic illustration of synthetic route for 1,3,5-triamino-2,4,6-benzenetriol trihydrochloride (TATHB)

4.2.2.1 Synthesis of 1,3,5-trinitro-2,4,6-benzenetriol (1)[114]

A round-bottom flask was charged with sulfuric acid (98%, 300 ml) and cooled to approximately 5 °C. Potassium nitrate (32.07 g, 0.317 mol) was added slowly with stirring to avoid increase in the temperature. After complete addition of potassium nitrate, the reaction mixture was stirred for 15 min and phloroglucinol (10 g, 0.079 mol) was added at a rate such that the temperature did not exceed 10 °C. Vigorous stirring was maintained to prevent concentrating the solid in the center. After complete phloroglucinol addition, the reaction mixture was stirred for 15 min and the cooling bath was removed. The reaction was stirred for an additional 30 min at room temperature. The heterogeneous yellow mixture was added in one portion to crushed ice (1000 g) and was stirred gently until all the ice had melted. The resulting precipitate was isolated by filtration, washed with cold 10% HCl. The resultant yellow solid was air dried to afford 1,3,5-trinitro-2,4,6-benzenetriol (20.08 g, 96.9%). ^{1}H NMR (400 MHz, DMSO-d_6) δ 6.59 (s, 1H, O*H*); ^{13}C NMR (100 MHz, DMSO-d_6) δ 153.92 ($Ar_{2,4,6}$-*C*), 122.14 ($Ar_{1,3,5}$-*C*).

4.2.2.2 Synthesis of 1,3,5-triamino-2,4,6-benzenetriol trihydrochloride (2)[115]

A batch reaction vessel (Parr Co.) was charged with 1,3,5-trinitro-2,4,6-benzenetriol (5.00 g, 19.150 mmol) containing 10% Pd/C (0.25 g), and 1M aqueous HCl (100 mL). The hydrogenation was carried at r.t. and a hydrogen pressure of 60 psi for 24 hr. The reaction mixture was filtered into concentrated HCl (200 ml) under reduced pressure over Celite to remove catalyst. The colorless precipitate was then placed in the freezer for 10 days, then isolated by filtration, washed with conc. HCl and ethyl ether. The solid was dried in vacuum over at 40 °C to provide 3.812 g (70.960%) of the 1,3,5-triamino-2,4,6-benzenetriol trihydrochloride as a white crystalline solid. ^{1}H NMR (400 MHz, DMSO-d_6) δ 10.01 (br, s, O*H*); ^{13}C NMR (100 MHz, DMSO-d_6) δ 144.60 ($Ar_{2,4,6}$-*C*), 104.29 ($Ar_{1,3,5}$-*C*).

4.2.3 Synthesis of TATHB-TPA-imine

4.2.3.1 General synthetic procedures

Transfer of all reagents was performed in an ambient air atmosphere with no precautions taken to exclude oxygen or atmospheric moisture. Pyrex glass ampoule charged with reagents and freeze-vacuum-thaw cycle with LN_2 were evacuated using a Schlenk line by fitting the short length of standard butyl rubber horse and further affixed to a ground glass tap and another short length of standard butyl rubber horse which could be closed to isolate this assembly from the dynamic vacuum when the desired internal pressure was reached. Ampoule was then sealed under this desired vacuum using a propane torch.[24]

4.2.3.2 TATHB-TPA-imine

A 50 mL glass ampoule was charged with 1,3,5-triamino-2,4,6-benzenetriol trihydrochloride (TATHB) (0.128 g, 0.4 mmol). The ampoule was degassed with argon using 3 evacuate-refill cycles. After filling with argon, methyl alcohol (4 mL) and pyridine (0.113 mL, 1.2 mmol) were added to neutralize the hydrochloride salt. The mixture was sonicated for 3 min to get a homogeneous dispersion. Subsequently, 1,3,5-trimethylbenzene (4 mL) solution of terephthaldehyde (TPA) (0.080 g, 0.6 mmol) and aqueous acetic acid (0.8 mL, 3M) were added. The ampoule was degassed through three freeze-vacuum-thaw cycles, flash frozen at 77 K (liquid N_2 bath) evacuated to an internal pressure of 300 mTorr and flame sealed. The reaction was heated at 120 °C for 72 h without disturbing. The yielded brown precipitate was isolated by filtration and washed with acetone. The collected powder was then activated by solvent exchange with acetone for 24 h and dried at 80 °C under vacuum overnight to give a light brown power with 84% isolated yield.

4.2.4 Synthesis of model compound

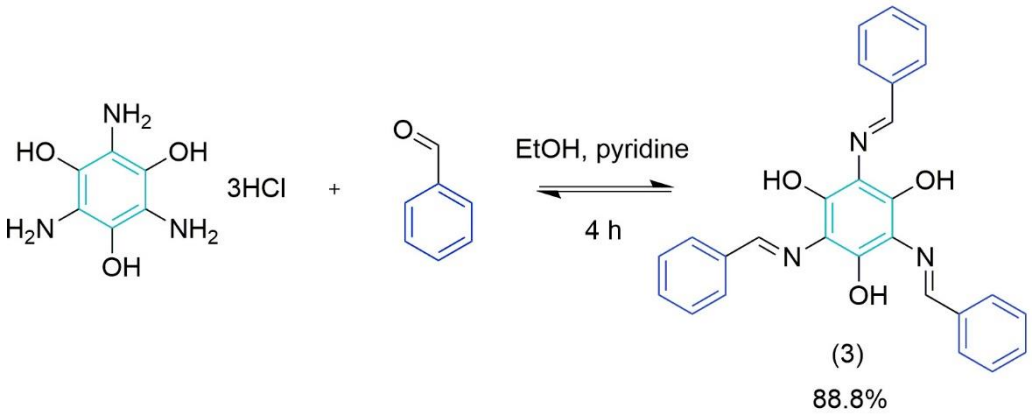

Scheme 4.2 | Schematic illustration of synthetic route for 2,4,6-tris(((E)-benzylidene)amino)benzene-

1,3,5-triol

4.2.4.1 Synthesis of 2,4,6-tris(((E)-benzylidene)amino)benzene-1,3,5-triol (3)

To a 250 mL Schlenk flask was added 1,3,5-triamino-2,4,6-benzenetriol trihydrochloride (0.560 g, 2 mmol, 1 equiv). The flask was degassed with argon using 3 evacuate-refill cycles. After filling with argon, ethyl alcohol (20 mL) and pyridine (0.645 mL, 8 mmol, 4 equiv) were added to neutralize the hydrochloride salt. The mixture was sonicated for 3 min to get a homogeneous dispersion. Subsequently, benzaldehyde (0.711 mL, 7 mmol, 3.5 equiv) was added and the mixture was refluxed for 4 h. The resultant light-yellow precipitate was collected by hot filtration, washed with cold ethanol and dried under vacuum to give a yellow solid in 88.85% yield (0.773 g). ^{1}H NMR (400 MHz, $CDCl_3$) δ 9.53 (s, 1H, O*H*), 7.87 (d, 2H, aromatic-*H*), 7.46 (m, 3H, aromatic-*H*); ^{13}C NMR (100 MHz, $CDCl_3$) δ 157.81, 148.53, 137.59, 130.88, 128.88, 128.08, 113.87.

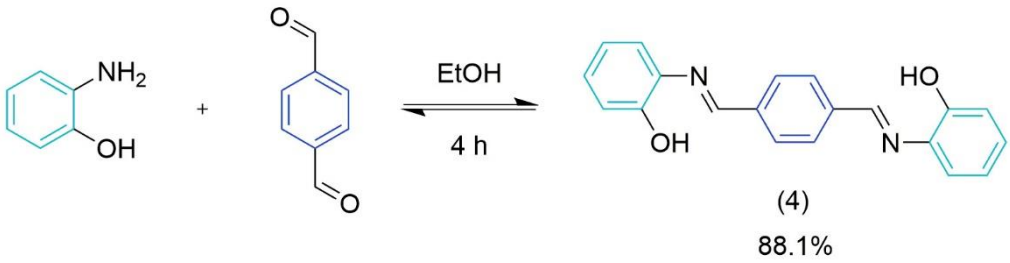

Scheme 4.3 | Schematic illustration of synthetic route form 2,2'-diphenol(((1E,1'E)-1,4 phenylenebis(methanylylidene))bis (azanylylidene))

4.2.4.2 Synthesis of 2,2'-diphenol(((1E,1'E)-1,4 phenylenebis(methanylylidene))bis (azanylylidene)) (4)

To a 250 mL Schlenk flask was added terephthaldehyde (0.402 g, 3 mmol, 1 equiv), 2-Aminophenol (0.680 g, 6.2 mmol, 2.1 equiv). The flask was degassed with argon using 3 evacuate-refill cycles. After filling with argon, ethyl alcohol (20 mL) was added and the mixture was refluxed for 4 h. The resultant reddish brown precipitate was collected by hot filtration, washed with cold ethanol and dried under vacuum to give a reddish brown solid in 88.1 % yield (0.835 g). ^{1}H NMR (400 MHz, Acetone-d_6) δ 8.93 (s, 1H, *H*C=N), 8.20 (s, 2H, aromatic-*H*), 8.12 (s, 1H, *OH*), 7.45 (d, 1H, aromatic-*H*), 7.21 (t, 1H, aromatic-*H*), 6.97 (d, 1H, aromatic-*H*), 6.91 (t, 1H, aromatic-*H*); ^{13}C NMR (100 MHz, Acetone-d_6) δ 157.21, 152.78, 138.5, 136.38, 129.20, 128.74, 119.82, 117.01, 115.50.

4.2.5 Physical characterization

Fourier transform infrared (FT-IR) spectra were recorded on a Perkin-Elmer Spectrum 100 in

transmission with KBr pellets. Thermogravimetric analysis (TGA) measurements was conducted on a TA Q600 (TA Instrument). The samples were heated from room temperature to 900 °C under air and nitrogen atmosphere at a heating rate of 10 °C min^{-1}. Powder X-ray diffraction data were collected using a Rigaku D/Max 2500 rotating anode X-ray powder diffractometer using Cu Kα radiation (λ = 1.5406 Å) operated at 1600 W (40 kV, 40 mA) power and equipped with a position sensitive detector with at 10.0 mm radiation entrance slit. Samples were mounted on zero background sample holders by dropping powders from a spatula and then fixed the samples onto holders with a glass slit. Data were collected in the range of 2θ = 2 to 50° with a step size 0.02° and a scan speed of 1° min^{-1}. Model structures for samples were generated in BIOVIA Materials Studio 7.0 (Accelrys Inc.) Pawley refinement was performed to optimize the lattice parameter iteratively. The Pseudo-Voigt function was used for whole profile fitting and Berrar-Baldinozzi function was used for asymmetry correction during the refinement processes until the R_p and R_{wp} values converge. SEM images were obtained by field-emission scanning electron microscopy (FE-SEM, FEI Nanonova 230) with accelerating voltage of 10 kV with a working distance of 5 mm equipped with an energy dispersive spectrometer. Samples were deposited onto a conductive carbon tape and treated through Pt sputtering before observation. Elemental analysis (EA) was conducted on a Thermo Scientific Flash 2000. The nitrogen sorption isotherms were recorded on a BELSORP-max at 77 K in a pressure range from $P/P_0 = 10^{-6}$ to 0.99. Prior to the measurement of the sorption isotherm the samples were degassed for 24 h at 150 °C under high vacuum. For the evaluation of the surface area the Brunauer-Emmett-Teller (BET) model was applied between 0.005 and 0.05 P/P_0. The calculations of the pore size distribution were performed using the nonlocal density functional theory (NLDFT) adsorption model with a carbon kernel for cylindrical pores.

4.3 Results and discussion

4.3.1 Synthesis of imine-linked COF

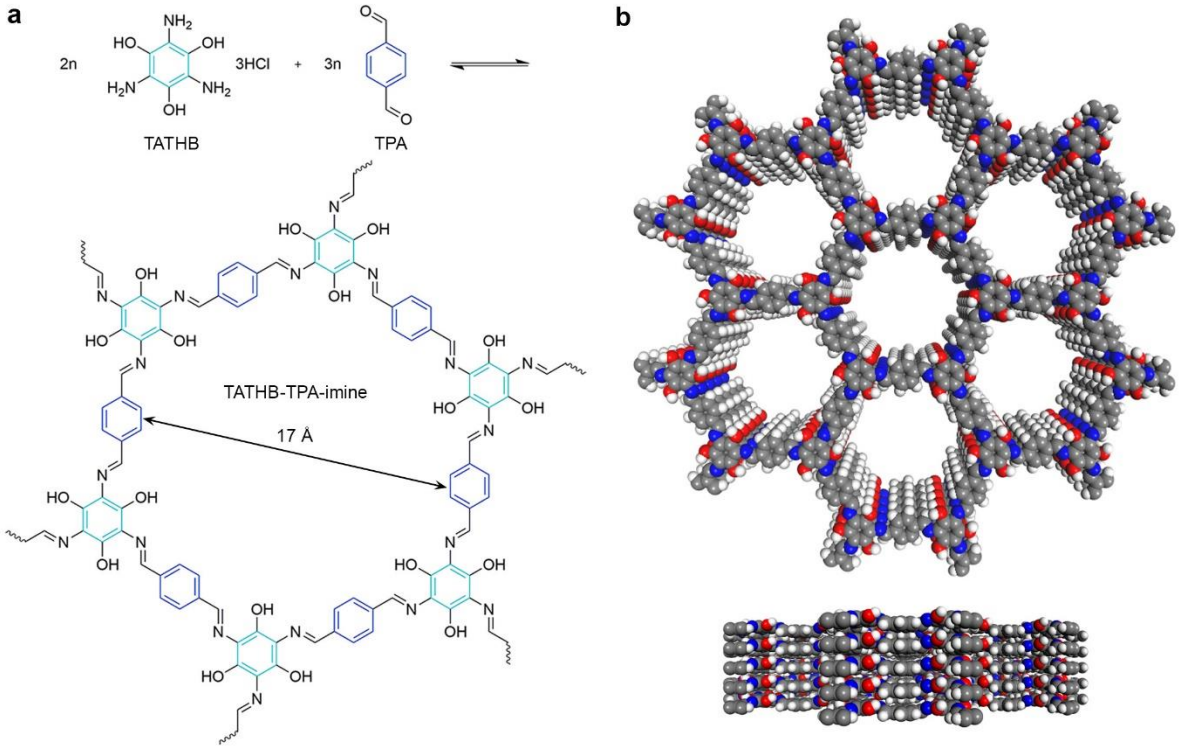

Scheme 4.4 | Strategy for preparing imine-linked COF. a, Schematic representation of the synthesis of the crystalline porous imine-linked COF (TATHB-TPA-imine) with extended triangular triamine and extended linear dialdehyde. **b**, Space filling diagram of TATHB-TPA-imine. Carbon, nitrogen, oxygen and hydrogen atoms are represented as grey, blue, red and white spheres, respectively.

The corresponding TATHB-TPA-imine COF was obtained from 1,3,5-triamino-2,4,6-benzenetriol trihydrochloride (TATHB) and terephthaldehyde (TPA) by solvothermal synthesis in methyl alcohol and 1,3,5-trimethylbenzene at 120 °C for 3 days. (Scheme 4.2, see the experimental, 4.2.3.2) The COF is insoluble in water or common organic solvents, such as hexane, acetone, tetrahydrofuran and *N*-methyl-2-pyrrolidone (NMP). It should be noted that the neutralization process is necessary for imine formation due to the hydrochloride salt in TATHB. (The rate of imine formation depends strongly on the *p*H. The reaction will be slow if not enough acid is present (that is, at high *p*H). On the other hand, if too much acid is present (low *p*H) the basic amine nucleophile is completely protonated, so the initial nucleophilic addition step can't occur.)[116] Indeed, hydrochloride salt of TATHB prohibits the rate of imine formation because the acidity is too strong. Therefore, the neutralization step is necessary before imine formation to run a reaction efficiently.

Table 4.1 | Synthesis of **TATHB-TPA-imine** under variable solvothermal conditions

Name	Condition	Temperature (°C)	Reaction time (day)	Yield (%)	BET surface area ($cm^3\ g^{-1}$)
TATHB-TPA-4M4M	Methanol (4 mL)/Mesitylene (4 mL)/ pyridine (0.11 mL)/3M Acetic acid (0.8 mL)	120	3	84.0	1581
TATHB-TPA-4M4M-1	Methanol (4 mL)/Mesitylene (4 mL)/triethylamine (0.17 mL)/3M Acetic acid (0.8 mL)	120	3	80.9	1134
TATHB-TPA-4E4M	Ethanol (4 mL)/Mesitylene (4 mL)/pyridine (0.11 mL)/3M Acetic acid (0.8 mL)	120	3	77.9	1061
TATHB-TPA-4B4O	Butanol (4 mL)/ODCB (4 mL)/pyridine (0.11 mL)/3M Acetic acid (0.8 mL)	120	3	75.5	684

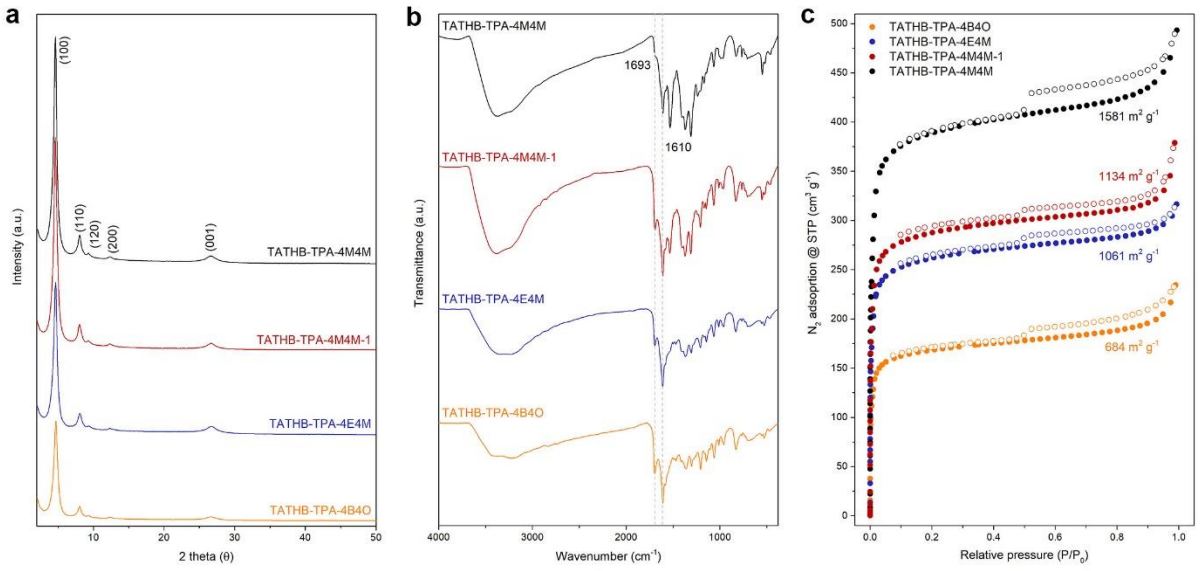

Figure 4.1 | **Optimization of imine-linked COF. a**, FT-IR spectra of TATHB-TPA-imine synthesized at different solvent ratio. **b**, PXRD pattern of TATHB-TPA-imine synthesized at different solvent ratio. **c**, Nitrogen sorption isotherms of TATHB-TPA-imine. Solid and open circles represent the adsorption and desorption branches, respectively.

Optimal COF growth conditions were established by characterizing the effect of the types of neutralizer and solvent ratio. (Figure 4.1) At first, we compared the crystallinity by using triethylamine or pyridine as a neutralizer, respectively. As seen in Figure 4.1, adding pyridine (pK_a = 4.7) as a neutralizer afforded a greater degree of crystallinity as well as increased surface area than adding triethylamine (pK_a = 10). It indicates that pyridine is more suitable neutralizer for synthesis of imine-linked COF. We then optimized the crystallinity by changing the solvent ratio. In the Fourier transform infrared (FT-IR) spectra, the obtained TATHB-TPA-imine displays similar characteristic peaks, indicating the formation of the imine linkages in the skeleton (Figure 4.1b). However, the polymerization conditions such as solubility strongly influence their crystallinity and specific surface area. For instance, solvent such as methanol/mesitylene and ethanol/mesitylene in the presence of aqueous acetic acid catalyst give crystalline polymers, while the obtained polymers exhibit a weak orderliness when the butanol/ODCB used as a reaction solvent (Figure 4.1a). Among the conditions, condensation reaction in mixture of methanol/mesitylene (1:1 v/v) produced crystalline TATHB-TPA-imine with relatively high specific surface area of over 1580 $m\,g^{-1}$. (Figure 4.1) These observations illustrate the importance of optimizing synthetic conditions for increased imine reversibility.

4.3.2 Crystallinity

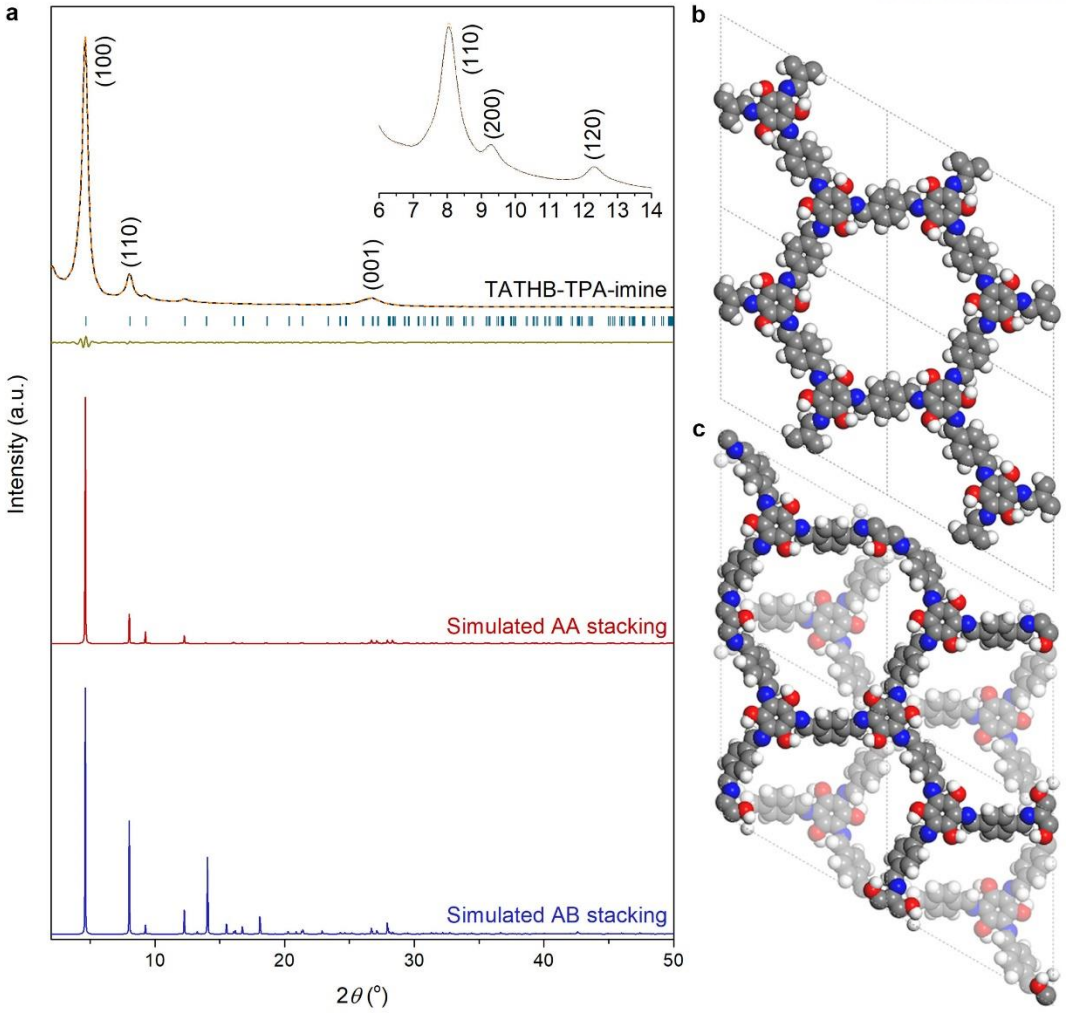

Figure 4.2 | PXRD pattern of imine-linked COF. a, Experimental (black line), Pawley-refined PXRD pattern (orange line), Bragg position (green dot), the difference plot (olive line), simulated with the AA-staking model (red line) and AB-stacking model (blue line). **b**, Simulated unit cell structure of the AA-stacking mode (C, grey; N, blue; O, red; H, white). **c**, Simulated unit cell structure of the AB-stacking mode (C, grey; N, blue; O, red; H, white; cyan, a further layer).

The crystallinity of imine material was measured by powder X-ray diffraction (PXRD). The PXRD pattern of TATHB-TPA-imine shows an intensive reflection at 4.6° corresponding to the (100) plane. The reflection at 8.0, 9.3, 12.3 and 26.6 are attributed to the (110), (120), (200) and (001) planes, respectively (Figure 4.2a, inset). Extended structure based on a hexagonal lattice in the space group *P*6 (No. 168) were modeled for TATHB-TPA-imine by using the Materials Studio software package. After a geometrical energy minimization by using the universal force field, the unit cell parameters and simulated PXRD patterns of TATHB-TPA-imine were obtained ($a = b = 22.20$ Å, $c = 3.34$ Å, $\alpha = \beta = 90°$ and $\gamma = 120°$). The obtained powder pattern for TATHB-TPA-imine is in good agreement with the energetically most favorable AA-stacking model (Figure 4.2a, red line). On the other hand, the AB-

stacking model gives an PXRD pattern that largely deviates from the experimentally observed profile. The Pawley-refined PXRD pattern (Figure 4.2a, orange dot) reproduces the experimentally observed curve with negligible differences (wR_p = 2.96%, R_p = 4.67%) (Figure 4.2a, olive line). Table 4.2 summarize the atomistic coordinates generated by Pawley refinements. As a result, the construction of COF shows an extended 2D hexagon lattice along the *x* and *y* directions (Scheme 4.4b, top view). The presence of the (001) plane at 26.7° suggests the structural ordering with 3.34 Å separation in the *z* axis perpendicular to the 2D lattice (Scheme 4.4b, side view).

4.3.3 Structural characterization

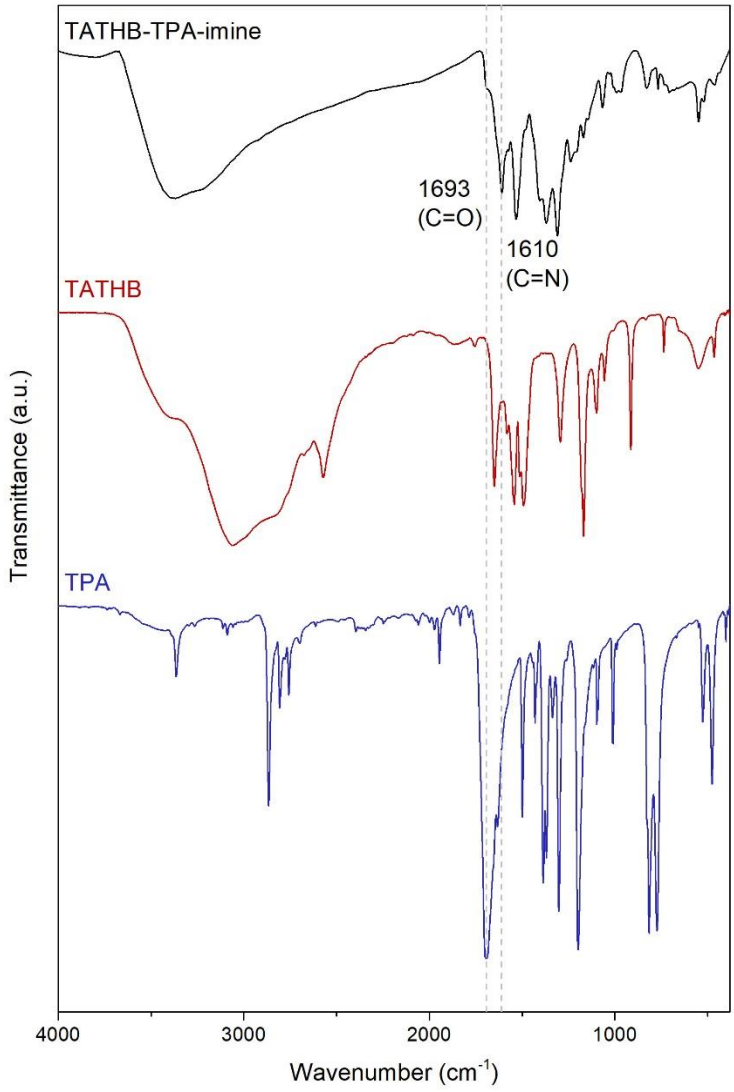

Figure 4.3 | FT-IR spectra of imine-linked COF.

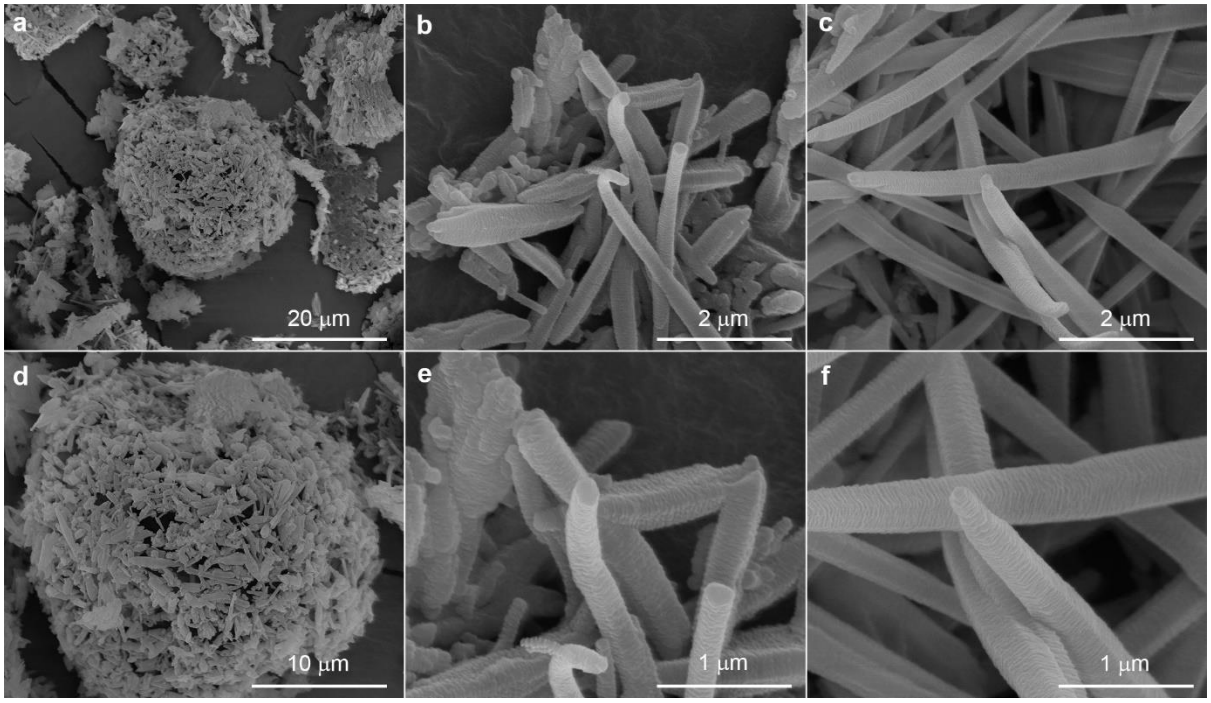

Figure 4.4 | **Morphologies of imine-linked COF. a-c**, SEM images of TATHB-TPA-imine. **d-f**, Magnified SEM images of **(a-c)**.

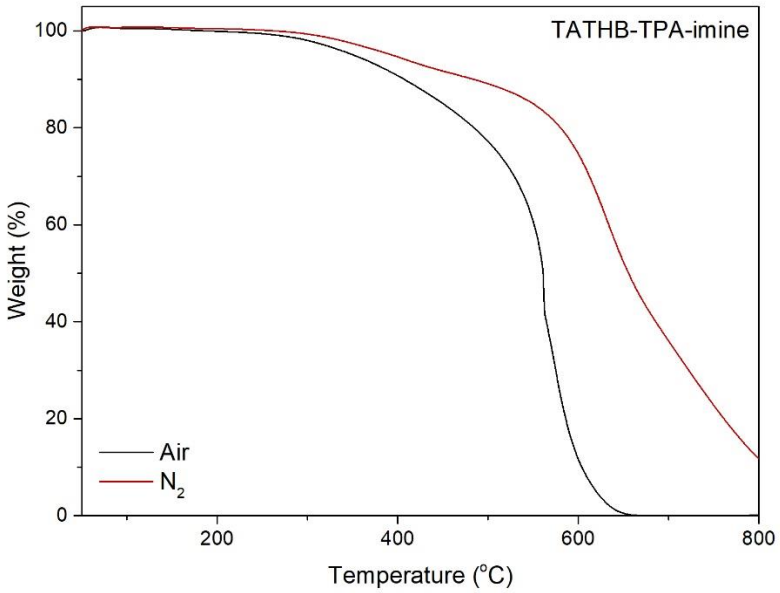

Figure 4.5 | **TGA thermograms of TATHB-TPA-imine.** The samples were heated at 10 °C in a constant flow of nitrogen.

The chemical structure of TATHB-TPA-imine was characterized by various analytical methods (see physical characterization 4.2.6) FT-IR revealed that the absorption at 1610 cm^{-1} assigned to the C=N stretching vibration band of the imine structure. The model compound also exhibited the C=N vibration

band at 1620 cm^{-1}. Field-emission scanning electron microscopy (FE-SEM) micrographs of TATHB-TPA-imine show spherical particles of ~10 μm in diameter that are encircled by thin rods. These thin rods are also composed of layered structure which the grain size of one layer is ~500 nm. Thermogravimetric analysis (TGA) indicates that TATHB-TPA-imine is stable up to 500 °C under nitrogen.

4.3.4 Porosity

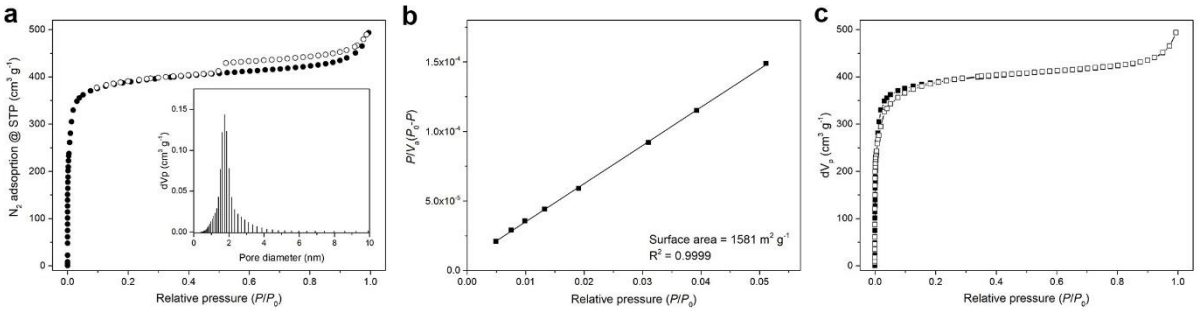

Figure 4.6 | Porosity of imine-linked COF. a, Nitrogen sorption isotherms of TATHB-TPA-imine. Solid and open circles represent the adsorption and desorption branches, respectively. Inset is corresponding pore size distribution of TATHB-TPA-imine from fitting the NLDFT model to the adsorption data. **b**, Simulated BET surface area plot of TATHB-TPA-imine at 77 K using nitrogen as adsorbate. **c**, Nitrogen isotherm measured at 77 K used for NLDFT modeling and pore size distribution calculations. The calculated NLDFT isotherm (cylindrical pore model) is overlaid as open square and fitting error indicated.

Permanent porosity of the materials was confirmed by N_2 sorption at 77 K (Figure 4.6). The sorption curve of the TATHB-TPA-imine is classified as typical type I isotherm characterized by a sharp uptake under low relative pressures in the range of P/P_0 = 0.005-0.05 (Figure 4.6a), a signature feature of microporous materials. The lack of hysteresis indicates that permanent microporous nature of imine-linked COF.[117] The BET surface area and pore volume were estimated to be 1581 $m^2\ g^{-1}$ and 0.75 $cm^3\ g^{-1}$ (P/P_0 = 0.99), respectively (Figure 4.6b). On the basis of nonlocal density-functional theory calculation from the sorption curve, the pore size of TATHB-TPA-imine was estimated to be 1.74 nm (inset in Figure 4.6a) with a low fitting error (Figure 4.6c), which is very good agreement with the theoretical pore size (1.75 nm, see Scheme 4.4).

4.4 Conclusion

In summary, a 2D imine-linked covalent organic framework (TATHB-TPA-imine) was successfully designed and synthesized under mild conditions. The new COF has excellent crystallinity and porosity with a high BET surface area of over 1500 $m^2\ g^{-1}$ and a relative small pore size. Currently, the design

and construction of new functionalized COFs for energy and catalyst related applications are undergoing in our laboratory.

Chapter 5 BENZOTHIAZOLE-BASED CRYSTALLINE POLYIMIDE COVALENT ORGANIC FRAMEWORK

5.1 Introduction

The chemistry of making molecular building blocks by covalent bond into extended structure, which is one of the oldest methodology in the field of material science, has yielded hyperbranched polymer as well as linear analogues.[118] Hyperbranched polymers are synthesized in a highly conjugated and porous form, thus it could be exploited in potential applications including gas storage and separations. However, they typically generate amorphous, disordered structure, which is difficult to ascertain the precise structure.[25]

Covalent organic frameworks (COFs) are a new class of crystalline polymers that the long-range ordered network is composed of covalent bond. Since the pioneering work in 2005, several types of COFs have been well documented.[20,21,24] The challenge in controlling crystallinity of COFs is the degree of chemical reversibility of linkage during polymerization; otherwise, amorphous hyperbranched polymers are obtained. Such linkages are limited in only a few organic reaction, including boronic acid trimerization, boronate ester formation, Schiff base reaction and nitrile trimerization.[49] Recently, Fang and coworkers demonstrated imide-linked COF *via* condensation polymerization of aromatic amines with anhydrides in mixed solvent such as *N*-methyl-2-pyrrolidone (NMP)/mesitylene mixture.[119,120] Aromatic polyimides are well known as an engineering polymers due to their excellent thermal and chemical stability. While many hyperbranched aromatic polyimide possessing amorphous structure and microporosity have been reported so far, there are a few crystalline imide-linked COFs made by a limited building block.[121,122,123] Therefore, the ability to develop strategies for controlling reaction is a challenge to enhance the degree of chemical reversibility in imide-linked COFs.

Here, we present a design and synthesis of new two-dimensional (2D) crystalline imide-linked COF (denoted as TBT-PMDA-COF). Benzothiazole-contained imide-linked COF is utilized *via* reversible amic acid reaction subsequent to chemical imidization. The imide-linked COF shows good crystallinity and mesoporosity. Also, it exhibits good thermal and chemical stability.

5.2 Experimental

5.2.1 Materials

Unless stated otherwise, all reactions were performed in oven dried glassware under ambient atmosphere. 1,3,5-Triaminobenzene and 2,5,8-triaminobenzo[1,2-d:3,4-d':5,6-d"]tris(thiazole) were synthesized according to published methods, respectively.[124,125,126] Pyromellitic dianhydride (PMDA) was purchased from Alfa Aesar and purified *via* sublimation at 180 °C (200 mtorr). N-methyl-2-pyrrolidone (NMP), 1,2-dichlorobenzene (ODCB), 3,5-dinitrobenzoic acid, potassium carbonate

(K_2CO_3) were purchased from Alfa Aesar. 1,3,5-Trimethylbenzene and isoquinoline was purchased from TCI Chemical. Palladium on carbon (10wt%), sodium azide and oleum were purchased from Sigma-Aldrich. Concentrated sulfuric acid, chloroform, ethyl acetate, celite and methanol were purchased from Samchun chemicals. Bromine was purchased from Junsei.

5.2.2 Synthesis of 2,5,8-triaminobenzo[1,2-d:3,4-d':5,6-d'']tris(thiazole)

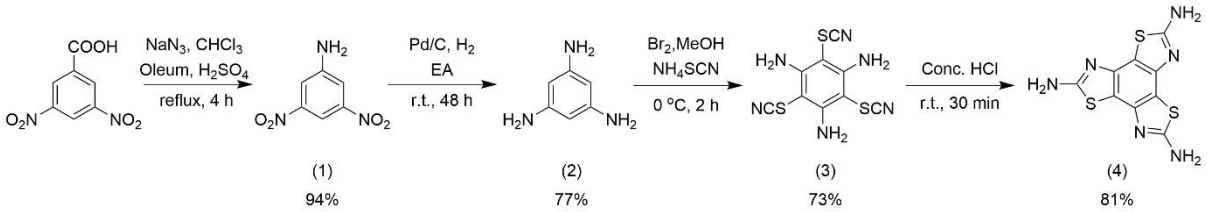

Scheme 5.1 | Schematic illustration of synthetic route for 2,5,8-triaminobenzo[1,2-d:3,4-d':5,6-d'']tris(thiazole) (TBT)

5.2.2.1 3,5-dinitroaniline (1)[127,128]

A solution of 3,5-dinitrobenzoic acid (50 g, 0.23 mol) in a mixture of 20% oleum (80 mL) and concentrated sulfuric acid (5 mL) was prepared in a three-neck round bottom flask equipped with reflux condenser. After stirring for 10 min., chloroform (160 mL) was added and the temperature was raised to 35 °C. With rapid stirring, sodium azide (17.6 g, 0.27 mol) was added in small portions, maintaining the temperature at 35-45 °C. Reaction was accompanied by foaming, and be sure not to add at the start until nuclei of white foam had disappeared. After all the sodium azide had been added, the mixture was heated to 80 °C for 4 hr. The resultant red solution was cooled to r.t., poured onto ice (1000 g). After standing for at least 10 min., the fine yellow precipitate was separated by filtration, washed thoroughly with cold water. The yellow crystalline solid was vacuum dried at 50 °C to afford 3,5-dinitroanilne (40.75 g, 94.4%). m.p. 162-163 °C(lit.); ^{1}H NMR (400 MHz, DMSO-d_6) δ 7.87 (t, 1H, aromatic-*H*) 7.72 (d, 2H aromatic-*H*), 6.51 (br s, 2H, N*H*$_2$); ^{13}C NMR (100 MHz, DMSO-d_6) δ 151.15 (Ar$_1$-*C*), 148.77 (Ar$_{3,5}$-*C*), 112.34 (Ar$_{2,6}$-*C*), 103.67 (Ar$_4$-*C*).

5.2.2.2 1,3,5-triaminobenzene (2)[126]

A batch reaction vessel (Parr Co.) was charged with 3,5-dinitroaniline (1.83 g, 0.01 mol) containing 10% Pd/C (0.06 g), and degassed ethyl acetate (80 mL). The hydrogenation was carried at r.t. and a hydrogen pressure of 60 psi for 72 hr, then the catalyst was filtered off on pad of Celite. After the filtrate was stored in freezer for 3 hr, the colorless precipitate was isolated by filtration and washed with cold ethyl acetate. The solid was dried at r.t. under vacuum over P_2O_5 for 24 hr to provide 1,3,5-triaminobenzene as a pink needle. Purification of 1,3,5-triaminobenzene was performed by vacuum sublimation at 100 °C,

10 mtorr. The resultant white powder was stored under nitrogen atmosphere because of the instability in oxygen. (0.95 g, 76.9%). m.p. 120 °C (dec.); ^{1}H NMR (400 MHz, DMSO-d_6) δ 5.14 (s, 1H, aromatic-*H*), 4.31 (s, 2H, N*H*$_2$); ^{13}C NMR (100 MHz, DMSO-d_6) δ 149.33 (Ar$_{1,3,5}$-*C*), 90.83 (Ar$_{2,4,6}$-*C*).

5.2.2.3 1,3,5-triamino-2,4,6-trithiocyanatobenzene (3)[124]

A three-neck round-bottom flask was charged with ammonium thiocyanate (13.70 g, 0.18 mol) and 1,3,5-triaminobenzene (3.69 g, 0.03 mol) in degassed methanol (100 mL). The resulting solution was maintained under a positive pressure of argon for the duration of the reaction. The reaction mixture was cooled in an ice bath, and a solution of 4.62 mL (0.09 mmol) of bromine in 20 mL of degassed methanol was added dropwise with stirring to the reaction vessel at a rate. A reddish precipitate was observed to form as the addition progressed. The reaction mixture was stirred in the ice bath for an additional 2 hr and then diluted with 200 mL of 10 % (v/v) K_2CO_3 solution. After 5 min, the off-white precipitate was collected by vacuum filtration and washed with H_2O. The yield of the off-white crude was 7.06 g (80%). The crude product was recrystallized from acetonitrile and dried under vacuum. The yield of off-white crystals was 6.44 g (73%). m.p. 227°C (dec.); ^{1}H NMR (400 MHz, DMSO-d_6) δ 6.73 (s, N*H*$_2$); ^{13}C NMR (100 MHz, DMSO-d_6) δ 156.26 (Ar$_{1,3,5}$-*C*), 111.70 (S*C*N) 74.45 (Ar$_{2,4,6}$-*C*). IR (KBr pellet): ν (cm^{-1}) 3472, 3354, 3198, 2155 (S-C≡N), 1604, 1524, 1434, 750. Anal. Calcd. for $C_9H_6N_6S_3$: C, 36.72; H, 2.05; N, 28.55; S, 32.67; Found: C, 36.38; H, 2.05; N, 29.19; S, 32.38%.

5.2.2.4 2,5,8-triaminobenzo[1,2-d:3,4-d':5,6-d"]tris(thiazole) (TBT) (4)[125]

A round-bottom flask was charged with 1,3,5-triamino-2,4,6-trithiocyanatobenzene (1 g, 3.39 mmol) in 50 mL of concentrated HCl in nitrogen atmosphere. The reaction mixture was changed to off-white slurry after 10 min. and it was stirred for 30 min. at r.t while monitoring with TLC. The resultant yellowish solid was diluted with 500 ml of cold water, separated by filtration and washed with hot water until yellow precipitant was removed. The light pink solid was treated with 1 M NH_4OH to neutralize the salt. The off-white solid is collected by filtration, washed with water and vacuum dried to provide 0.806 g (80.6%) of 2,5,8-triaminobenzo[1,2-d:3,4-d':5,6-d"]tris(thiazole) as an off-white solid. ^{1}H NMR (400 MHz, DMSO-d_6) δ 7.56 (br s, N*H*$_2$); ^{13}C NMR (100 MHz, DMSO-d_6) δ 167.24 (Ar$_{2,5,8}$-*C*), 143.98 (Ar$_{1,4,7}$-*C*) 111.59 (Ar$_{3,6,9}$-*C*). IR (KBr pellet): ν (cm^{-1}) 3315, 3190 1626, 1528, 1384, 1316.

5.2.3 Synthesis of TBT-PMDA-COF

5.2.3.1 General synthetic procedures

Transfer of all reagents was performed in an ambient air atmosphere with no precautions taken to exclude oxygen or atmospheric moisture. Pyrex glass ampoule charged with reagents and freeze-vacuum-thaw cycle with LN_2 were evacuated using a Schlenk line by fitting the short length of standard

butyl rubber horse and further affixed to a ground glass tap and another short length of standard butyl rubber horse which could be closed to isolate this assembly from the dynamic vacuum when the desired internal pressure was reached. Ampoule was then sealed under this desired vacuum using a propane torch.[24]

5.2.3.2 TBT-PMDA-COF

A 50 mL pyrex tube was charged with TBT (0.117 g, 0.4 mmol) and PMDA (0.1309 g, 0.6 mmol) in a solution of NMP/ODCB (5 mL, 3/7 by vol.), and the mixture was sonicated for two minutes. After adding isoquinoline (0.1 mL) as catalyst, the tube was degassed through the freeze-vacuum-thaw cycles, flame sealed under vacuum and heated at 180 °C for 5 days. The mixture was cooled to room temperature and the precipitate was isolated by filtration over a medium glass frit and washed with acetone for several times. The product was immersed in acetone for 24 h, then the solvent was removed under vacuum at 80 °C to afford TBT-PMDA-COF as an orange powder (0.208 g, 91.6%).

5.2.4 Physical characterization

Fourier transform infrared (FT-IR) spectra were recorded on a Perkin-Elmer Spectrum 100 in transmission with KBr pellets. Thermogravimetric analysis (TGA) measurements was conducted on a TA Q600 (TA Instrument). The samples were heated from room temperature to 900 °C under air and nitrogen atmosphere at a heating rate of 10 °C min^{-1}. Powder X-ray diffraction data were collected using a Rigaku D/Max 2500 rotating anode X-ray powder diffractometer using Cu Kα radiation (λ = 1.5406 Å) operated at 1600 W (40 kV, 40 mA) power and equipped with a position sensitive detector with at 6.0 mm radiation entrance slit. Samples were mounted on zero background sample holders by dropping powders from a spatula and then fixed the samples onto holders with a glass slit. Data were collected in the range of 2θ = 2 to 50° with a step size 0.02° and a scan speed of 1° min^{-1}. Model structures for samples were generated in BIOVIA Materials Studio 7.0 (Accelrys Inc.) Pawley refinement was performed to optimize the lattice parameter iteratively. The Pseudo-Voigt function was used for whole profile fitting and Berrar-Baldinozzi function was used for asymmetry correction during the refinement processes until the R_p and R_{wp} values converge. SEM images were obtained by field-emission scanning electron microscopy (FE-SEM, FEI Nanonova 230) with accelerating voltage of 10 kV with a working distance of 5 mm equipped with an energy dispersive spectrometer. Samples were deposited onto a conductive carbon tape and treated through Pt sputtering before observation. Elemental analysis (EA) was conducted on a Thermo Scientific Flash 2000. The nitrogen sorption isotherms were recorded on a BELSORP-max at 77 K in a pressure range from P/P_0 = 0.0001 to 0.99. Prior to the measurement of the sorption isotherm the samples were degassed for 24 h at 150 °C under high vacuum. For the evaluation of the surface area the Brunauer-Emmett-Teller (BET) model was

applied between 0.06 and 0.16 P/P_0. The calculations of the pore size distribution were performed using the nonlocal density functional theory (NLDFT) adsorption model with a carbon kernel for cylindrical pores.

5.3 Results and discussions

5.3.1 Design of imide-linked COFs

Inspired by the success of imide-linked COFs by previous reports,[119,120] whose linkages are composed of aromatic triamine or tetramine building blocks and dianhydride building units, we identified benzothiazole contained triamine as an attractive target for the imidization. Benzothiazole itself is a rigid and has aromaticity, hence making amine more stable than other typical aromatic triamine. On the basis of imidization.[129] the C_2-symmetric linear building block, pyromellitic dianhydride (PMDA), reacts with the C_3-symmetric triangular building block 2,5,8-triaminobenzo[1,2-d:3,4-d':5,6-d"]tris(thiazole) (TBT) to produce the extended 2D porous imide-linked COF, TBT-PMDA-COF (scheme 5.2).

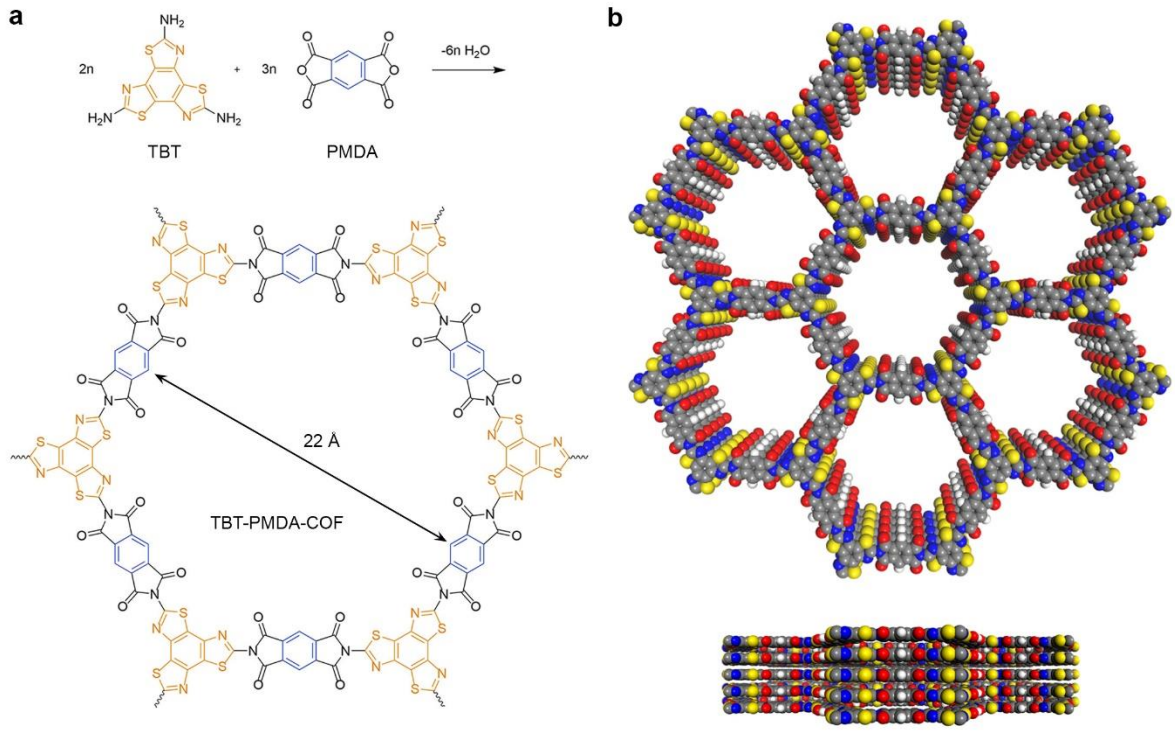

Scheme 5.2 | Strategy for preparing imide-linked COF. a, Schematic representation of the synthesis of the crystalline porous imide-linked COF (TBT-PMDA-COF) with extended triangular triamine and extended linear dianhydride. **b**, Space filling diagram of TBT-PMDA-COF. Carbon, nitrogen, oxygen, sulfur and hydrogen atoms are represented as grey, blue, red, yellow and white spheres, respectively.

5.3.2 Synthesis and structural characterization of imide-linked COFs

Specifically, TBT-PMDA-COF was synthesized by reacting TBT and PMDA in mixed solution of *N*-methyl-2-pyrrolidone (NMP), 1,2-dichlorobenzene (ODCB) and isoquinoline followed by heating at 180 °C for 5 days, giving crystalline solid at yields of 80%. The resultant product was insoluble in water and common organic solvents including acetone, THF, DMF and *m*-cresol.

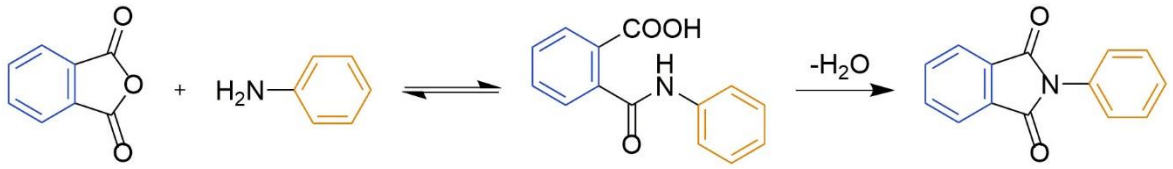

Scheme 5.3 | Mechanism of imide linkage. Schematic representation of the synthesis of imide linkage by two-step imidization.

Typically, the most common method for synthesis of polyimide is “two-step” method, including formation of poly(amic acid) intermediate *via* a reaction of amine with anhydride before cyclizing to imide linkage. The formation of poly(amic acid) is reversible reaction. However, the rate of forward reaction is several orders of magnitude larger than the backward reaction, thus strategy for rate control of poly(amic acid) formation must be considered to improve the crystallinity(scheme 5.3). Such low degree of reversibility of amic acid reaction hinder the preparation of crystalline imide-linked COF compared to other types of reported COFs. To enhance the crystallinity, we optimized the reaction by changing some parameters such as the ratio of the mixed solvents, using isoquinoline as catalyst for imidization. The mixed solvent used here (NMP and ODCB) controls the solubility of the monomers. Especially, the nonpolar solvent acts as an azeotroping solvent, which enables to remove the water formed during the reaction and drive the reaction to completion.[130] Furthermore, isoquinoline promote the speed of imidization in solution.

Table 5.1 | Synthesis of **TBT-PMDA-COF** under variable solvothermal conditions

Name	Condition	Temperature (°C)	Reaction time (day)	Yield (%)
TBT-PMDA-1.5N3.5O	NMP (1.5 mL)/ODCB (3.5 mL)/isoquinoline (0.1 mL)	180	5	91.6
TBT-PMDA-2N3O	NMP (2 mL)/ODCB (3 mL)/isoquinoline (0.1 mL)	180	5	63.9
TBT-PMDA-1N4O	NMP (1 mL)/ODCB (4 mL)/isoquinoline (0.1 mL)	180	5	102.2

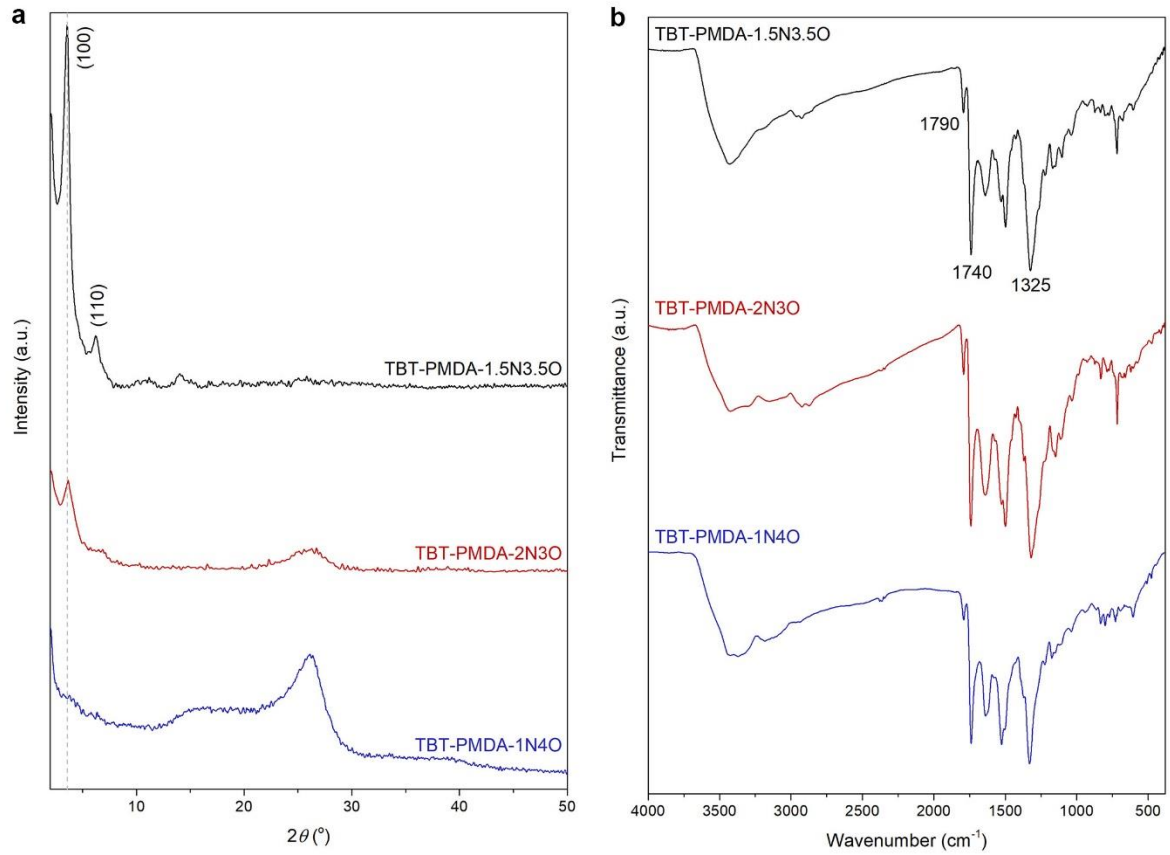

Figure 5.1 | **Optimization of imide-linked COF. a**, FT-IR spectra of TBT-PMDA-COF synthesized at different solvent ratio. **b**, PXRD pattern of TBT-PMDA-COF synthesized at different solvent ratio.

According to our experimental experience, crystallinity is highly depending on the ratio of solvent. As seen in Figure 5.1a, the obtained TBT-PMDA-COF displays similar characteristic peaks in the

Fourier transform infrared (FT-IR) spectra, indicating the formation of the imide linkages in the skeleton. However, the polymerization conditions such as solubility strongly influence their crystallinity. As increasing amount of nonpolar solvent, an orderliness was confirmed by PXRD, while other obtained polymers exhibit lack of crystallinity (Figure 5.1b). These observations illustrate the importance of optimizing synthetic conditions for increased imide reversibility.

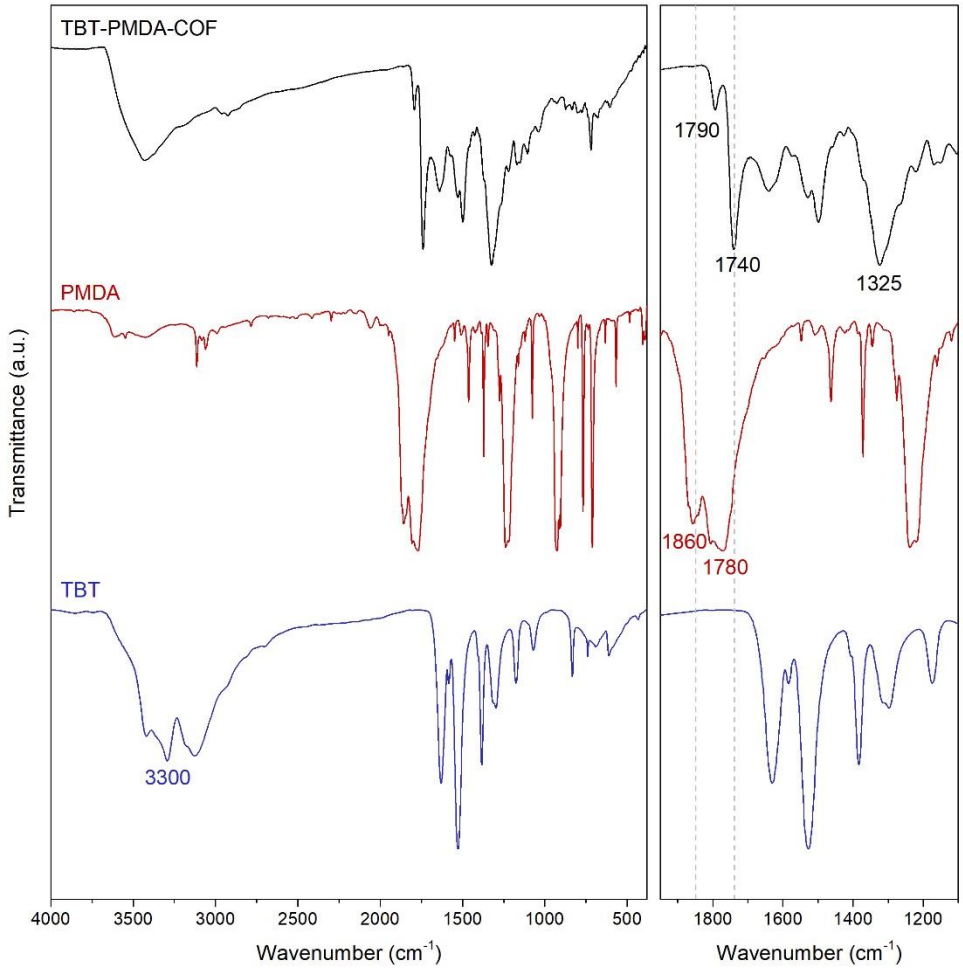

Figure 5.2 | FT-IR spectra of imide-linked COF. Full FT-IR spectra (KBr pellets) (left); magnification of the fingerprint region between 1100 cm^{-1} and 1950 cm^{-1} showing the signals of the characteristic C=O stretching vibration and C–N-C stretching vibration (right).

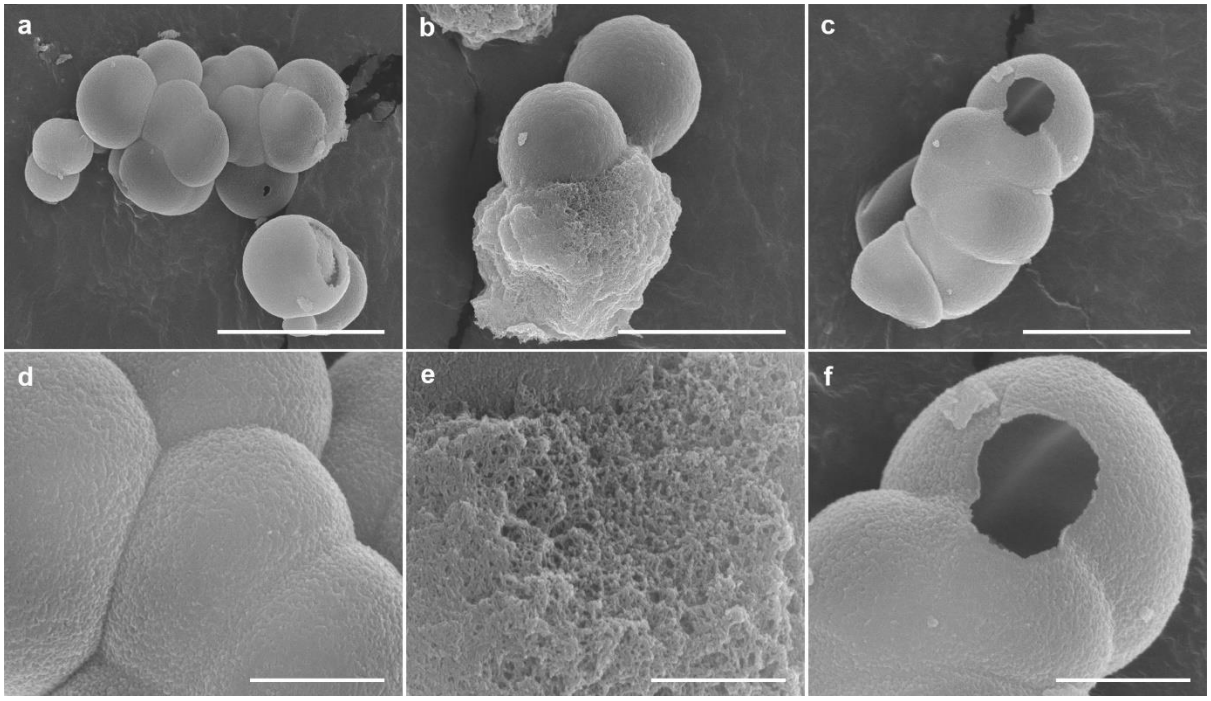

Figure 5.3 | **Morphologies of imide-linked COF. a-c**, SEM images of TBT-PMDA-COF. Scale bars are 5 μm. **d-f**, Magnification of SEM images. Scale bars are 1 μm.

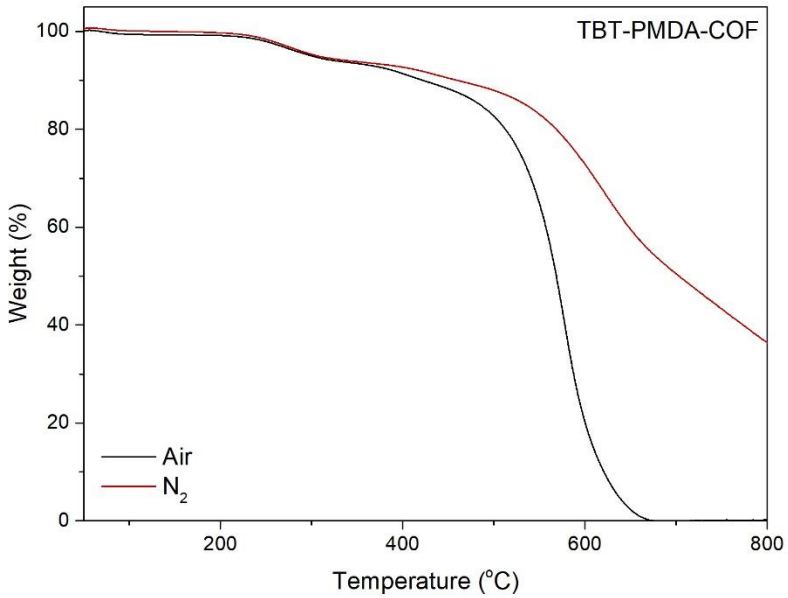

Figure 5.4 | **TGA thermograms of TBT-PMDA-COF.** The samples were heated at 10 °C min^{-1} in a constant flow of nitrogen.

Progress of the imidization reaction was monitored by FT-IR spectroscopy (Figure 5.2). Absorptions at 1790 and 1740 cm^{-1} for TBT-PMDA-COF are assigned to asymmetric and symmetric stretching vibrations, respectively, of C=O groups of the imide moieties.[129] Compared with the signals for carbonyl

of the reactant dianhydride, those of the TBT-PMDA-COF shift toward lower wavenumber, which indicates the formation of polyimide backbone. The absorption at 1325 cm^{-1} for TBT-PMDA-COF are attributed to the stretching vibration of C-N-C moieties, manifests the generation of the five-membered rings.[123] No bands corresponding to the starting monomers (amine around 3300 cm^{-1} and anhydride around 1780 and 1860 cm^{-1}) or amic acid (amide around 1650) appeared, demonstrating that the resultant COF composed of fully imidized network. Field-emission scanning electron microscopy (FE-SEM) micrographs of TBT-PMDA-COF show spherical particles of ~4 μm in diameter that are agglomerated by microcrystallities of ~50 nm. No other structures were observed from SEM images taken through the material. (Figure 5.3) Similar to amorphous porous PIs, TBT-PMDA-COF also exhibited high thermal stability as determined by thermogravimetric analysis (TGA), up to 500 °C under nitrogen (Figure 5.4).

5.3.3 Crystallinity of imide-linked COF

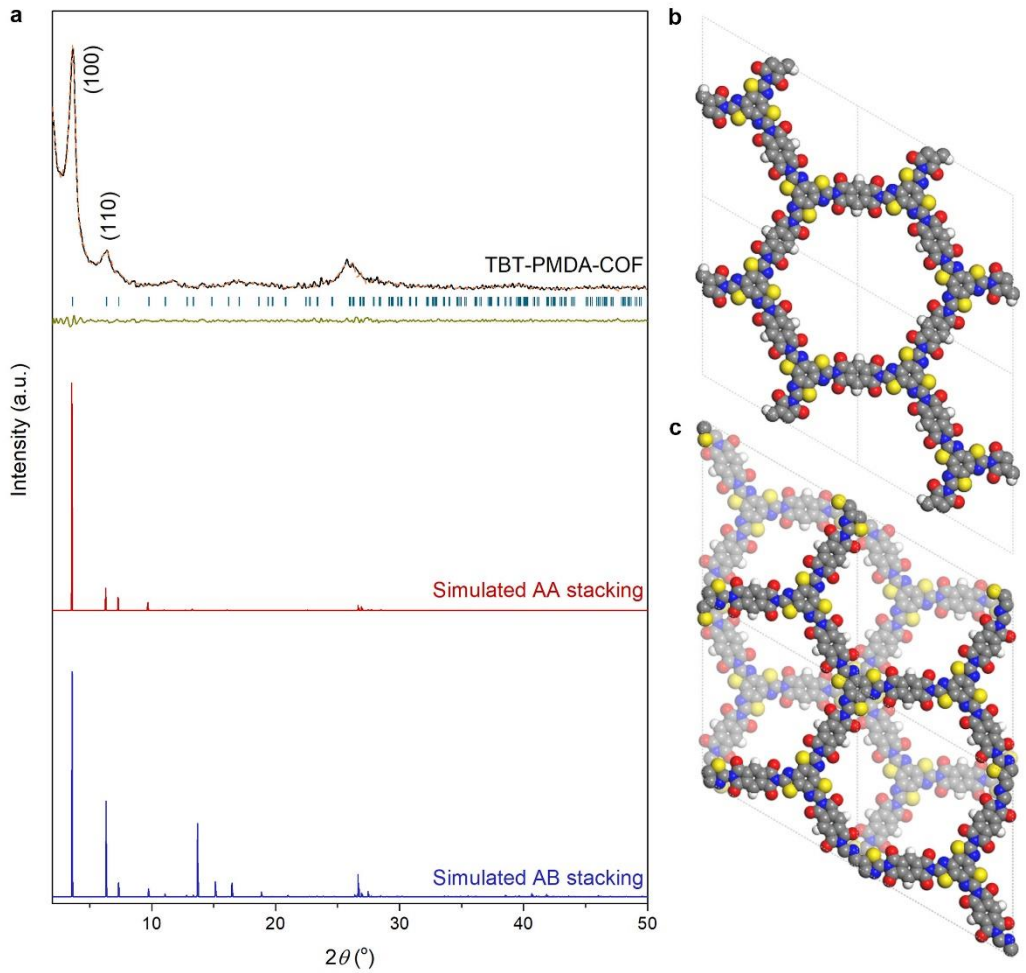

Figure 5.5 | PXRD pattern of imide-linked COF. a, Experimental (black line), Pawley-refined PXRD pattern (orange line), Bragg position (green dot), the difference plot (olive line), simulated with the AA-staking model (red line) and AB-stacking model (blue line). **b**, Simulated unit cell structure of the AA-

stacking mode (C, grey; N, blue; O, red; S, yellow; H, white). **c**, Simulated unit cell structure of the AB-stacking mode (C, grey; N, blue; O, red; S, yellow; H, white; cyan, a further layer).

The crystallinity of TBT-PMDA-COF was measured by powder X-ray diffraction (PXRD) (Figure 5.5). Extended structure based on a hexagonal lattice in the space group P6/M (No. 175) were modeled for TBT-PMDA-COF by using the Materials Studio software package. After a geometrical energy minimization by using the universal force field, the unit cell parameters and simulated PXRD patterns of TBT-PMDA- COF were obtained ($a = b = 27.32$ Å, $c = 3.421$ Å). The obtained powder pattern for TBT-PMDA-COF is in good agreement with the expected imide-linked structure. Furthermore, full profile pattern matching (Pawley) refinements were carried out on the experimental PXRD patterns. Peaks at 3.56 and 6.28° for TBT-PMDA-COF correspond to the (100) and (110) Bragg peaks of hexagonal lattice. The refinement results yield unit cell parameters nearly equivalent to the predictions with good agreement factors ($a = b = 27.32$ Å, c = 6.842 Å, $\alpha = \beta = 90°$ and $\gamma = 120°$, $wR_p = 9.35\%$, $R_p = 5.50\%$). We also considered alternative structures wherein adjacent sheets are staggered based on the space group of P63/M (no.176). For the staggered structures, the simulated PXRD patterns did not match the experimental data.

5.3.4 Porosity of imide-linked COF

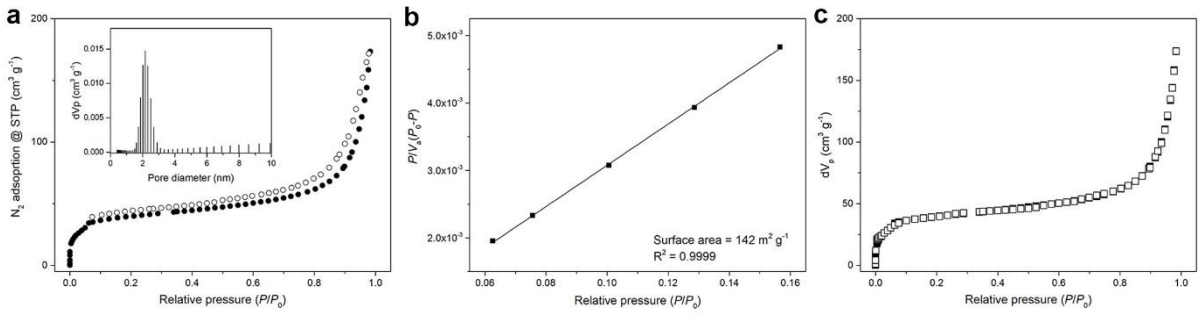

Figure 5.6 | Porosity of imide-linked COF. a, Nitrogen sorption isotherms of TBT-PMDA-COF. Solid and open circles represent the adsorption and desorption branches, respectively. Inset is corresponding pore size distribution of TBT-PMDA-COF from fitting the NLDFT model to the adsorption data. **b**, Simulated BET surface area plot of TBT-PMDA-COF at 77 K using nitrogen as adsorbate. **c**, Nitrogen isotherm measured at 77 K used for NLDFT modeling and pore size distribution calculations. The calculated NLDFT isotherm (cylindrical pore model) is overlaid as open square and fitting error indicated.

The permanent porosity of the TBT-PMDA-COF was determined by measuring N_2 adsorption at 77 K, revealing reversible type-IV isotherms with a sharp uptake below $P/P_0 = 0.05$ (Figure 5.6a). The significant adsorption at low pressure supports the presence of micropores (pore size less than 2 nm),

whereas the step observed at P/P_0 = 0.05–0.20 indicates pore condensation in mesopores (pore size between 2 and 50 nm) with a narrow distribution. The absence of hysteresis during desorption is a common feature of materials containing hexagonally aligned 1D mesopores. Pore size distributions of TBT-PMDA-COF were calculated on the basis of nonlocal density functional theory (NLDFT). The pore size of TBT-PMDA-COF was estimated to be 2.16 nm (Figure 5.6a, inset) with a low fitting error (Figure 5.6c), which is good agreement with the theoretical pore size (2.20 nm, see Scheme 5.2). The Brunauer-Emmett-Teller (BET) model was applied over the $0.06 < P/P_0 < 0.16$ range of the isotherm, yielding BET surface areas of 142 $m^2\ g^{-1}$ with total pore volume of 0.27 $cm^3\ g^{-1}$ (P/P_0 = 0.98, Figure 5.6b)

5.3.5 Chemical stability of imide-linked COF

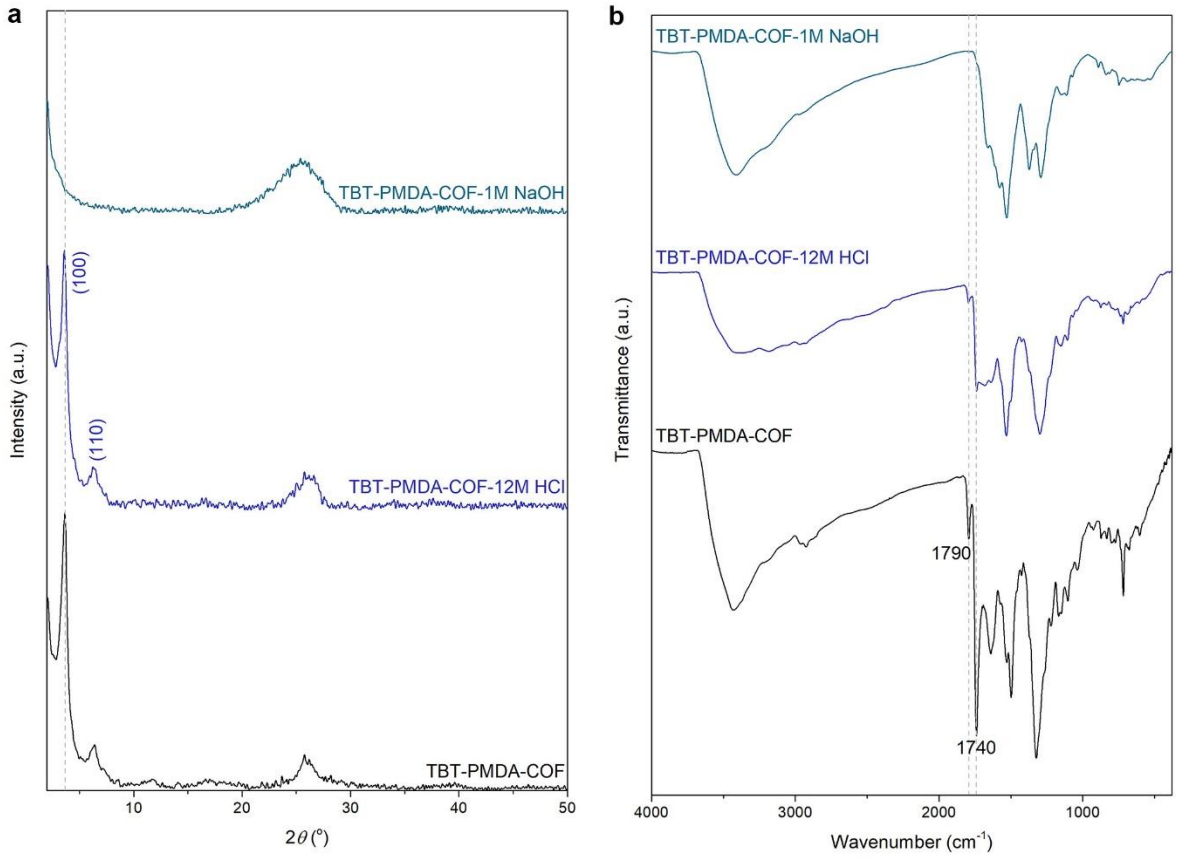

Figure 5.7 | Chemical stability of imide-linked COF. a,**b**, (**a**) PXRD patterns and (**b**) Full IR spectra showing retention of crystallinity of TBT-PMDA-COF after treatment for 24 h in different chemical conditions.

To investigate the chemical stability of TBT-PMDA-COF, we dispersed samples for 24 h in various solvents, including aqueous HCl (12 M) and aqueous NaOH (1 M) solutions (Figure 5.7). Under a harsh condition of a strong acid (12 M HCl), the TBT-PMDA-COF retains its crystallinity and imide linkage,

while remaining material is rendered amorphous and hydrolyzed into amic acid linkage under basic conditions (1 M NaOH).

5.4 Conclusion

We have demonstrated the synthesis of imide-linked COF under *in-situ* imidization reaction. The imide-linked COF shows both crystallinity and permanent porosity. This material also exhibits thermal and chemical stability in acidic media. The imide-linked COF prepared in this work may provide a promising energy-storage system as a cathode material for Li-ion batteries.

Chapter 6 Conclusion

In this thesis the synthesis and modification of 2D layered materials was investigated to enhance its processability for practical applications. Preparation of various 2D layered materials such as graphene nanoplatelets and covalent organic frameworks have been studied based on two synthetic standpoints, including top-down and bottom-up approaches.

In chapter 2 and 3, I demonstrated postsynthetic modification of graphite into graphene nanoplatelets *via* solvent-free Diels-Alder reaction. The solvent-free Diels-Alder reaction of pristine graphite enables to functionalize dienophiles especially at the edge of graphite. Also, this top-down approach can employ exfoliation of graphite into graphene nanoplatelets by dispersing them into common organic solvent. The organic functionality acts as a stabilizer of solvent-dispersed graphene nanoplatelets, which finally hinders to reaggregate them in solution to get a better processability. Moreover, chemical properties of graphene nanoplatelets can be tailored depending on the dienophiles. For example, maleic anhydride functionalized graphene nanoplatelets denoted as MA-GnP or MAG exhibited better dispersibility in polar organic solvent than maleimide functionalized graphene nanoplatelets denoted as MI-GnP or MIG, due to the carboxylic acid group at the MA-GnP and MAG. To demonstrate the reactivity depending on synthetic approaches, two approaches were selected. The one is Diels-Alder reaction of graphite *via* mechanochemical approach which described in chapter 2, the other is solvothermal approach discussed in chapter 3. The resultant product made by mechanochemical approach has higher degree of functionalization than the other one produced by solvothermal approach, hence mechanochemical approaches is more powerful than solvothermal approaches in graphene chemistry.

In chapter 4, I demonstrated synthesis and presynthetic modification of imine-linked COF with high crystallinity and porosity. To improve the reactivity of COF, I designed small-pore crystalline COF using specific triamine building block including hydroxy groups. The resultant imine-linked COF showed high crystallinity and microporosity, and it exhibited high thermal stability. To improve the chemical stability of COF, I studied synthesis of imide-linked COF in chapter 5. Because of the irreversible second step imidization, the imide-linked COF showed high thermal stability and chemical stability along with the 1D polyimide analogues. Also, imide-linked COF exhibited good crystallinity and mesoporosity.

References

1. Xie, C.; Mak, C.; Tao, X. M.; Yan, F., Photodetectors Based on Two-Dimensional Layered Materials Beyond Graphene. *Adv. Funct. Mater.* **2017**, *27*, 1603886.

2. Miro, P.; Audiffred, M.; Heine, T., An atlas of two-dimensional materials. *Chem. Soc. Rev.* **2014**, *43*, 6537-6554.

3. Geim, A. K.; Novoselov, K. S., The rise of graphene. *Nat. Mater.* **2007**, *6*, 183-191.

4. Ding, S. Y.; Wang, W., Covalent organic frameworks (COFs): from design to applications. *Chem. Soc. Rev.* **2013**, *42*, 548-568.

5. Tan, C. L.; Cao, X. H.; Wu, X. J.; He, Q. Y.; Yang, J.; Zhang, X.; Chen, J. Z.; Zhao, W.; Han, S. K.; Nam, G. H., et al., Recent Advances in Ultrathin Two-Dimensional Nanomaterials. *Chem. Rev.* **2017**, *117*, 6225-6331.

6. Ciesielski, A.; Samor, P., Supramolecular Approaches to Graphene: From Self-Assembly to Molecule-Assisted Liquid-Phase Exfoliation. *Adv. Mater.* **2016**, *28*, 6030-6051.

7. Gupta, A.; Sakthivel, T.; Seal, S., Recent development in 2D materials beyond graphene. *Prog. Mater Sci.* **2015**, *73*, 44-126.

8. Zhang, H., Ultrathin Two-Dimensional Nanomaterials. *ACS Nano* **2015**, *9*, 9451-9469.

9. Boott, C. E.; Nazemi, A.; Manners, I., Synthetic Covalent and Non-Covalent 2D Materials. *Angew. Chem. Int. Ed.* **2015**, *54*, 13876-13894.

10. Chhowalla, M.; Shin, H. S.; Eda, G.; Li, L. J.; Loh, K. P.; Zhang, H., The chemistry of two-dimensional layered transition metal dichalcogenide nanosheets. *Nat. Chem.* **2013**, *5*, 263-275.

11. Allen, M. J.; Tung, V. C.; Kaner, R. B., Honeycomb Carbon: A Review of Graphene. *Chem. Rev.* **2010**, *110*, 132-145.

12. Hirsch, A., The era of carbon allotropes. *Nat. Mater.* **2010**, *9*, 868-871.

13. Stolyarova, E.; Rim, K. T.; Ryu, S. M.; Maultzsch, J.; Kim, P.; Brus, L. E.; Heinz, T. F.; Hybertsen, M. S.; Flynn, G. W., High-resolution scanning tunneling microscopy imaging of mesoscopic graphene sheets on an insulating surface. *Proc. Natl. Acad. Sci. U. S. A.* **2007**, *104*, 9209-9212.

14. Novoselov, K. S.; Geim, A. K.; Morozov, S. V.; Jiang, D.; Zhang, Y.; Dubonos, S. V.; Grigorieva, I. V.; Firsov, A. A., Electric field effect in atomically thin carbon films. *Science* **2004**, *306*, 666-669.

15. Novoselov, K. S.; Fal'ko, V. I.; Colombo, L.; Gellert, P. R.; Schwab, M. G.; Kim, K., A roadmap for graphene. *Nature* **2012**, *490*, 192-200.

16. Ferrari, A. C.; Bonaccorso, F.; Fal'ko, V.; Novoselov, K. S.; Roche, S.; Boggild, P.; Borini, S.; Koppens, F. H. L.; Palermo, V.; Pugno, N., et al., Science and technology roadmap for graphene, related two-dimensional crystals, and hybrid systems. *Nanoscale* **2015**, *7*, 4598-4810.

17. Bonaccorso, F.; Lombardo, A.; Hasan, T.; Sun, Z. P.; Colombo, L.; Ferrari, A. C., Production and processing of graphene and 2d crystals. *Mater. Today* **2012**, *15*, 564-589.

18. Eigler, S.; Hirsch, A., Chemistry with Graphene and Graphene Oxide-Challenges for Synthetic Chemists. *Angew. Chem. Int. Ed.* **2014**, *53*, 7720-7738.

19. Georgakilas, V.; Otyepka, M.; Bourlinos, A. B.; Chandra, V.; Kim, N.; Kemp, K. C.; Hobza, P.; Zboril, R.; Kim, K. S., Functionalization of Graphene: Covalent and Non-Covalent Approaches, Derivatives and Applications. *Chem. Rev.* **2012**, *112*, 6156-6214.

20. Waller, P. J.; Gandara, F.; Yaghi, O. M., Chemistry of Covalent Organic Frameworks. *Acc. Chem. Res.* **2015**, *48*, 3053-3063.

21. Huang, N.; Wang, P.; Jiang, D. L., Covalent organic frameworks: a materials platform for structural and functional designs. *Nat. Rev. Mater.* **2016**, *1*.

22. Rowan, S. J.; Cantrill, S. J.; Cousins, G. R. L.; Sanders, J. K. M.; Stoddart, J. F., Dynamic covalent chemistry. *Angew. Chem. Int. Ed.* **2002**, *41*, 898-952.

23. Feng, X.; Ding, X. S.; Jiang, D. L., Covalent organic frameworks. *Chem. Soc. Rev.* **2012**, *41*, 6010-6022.

24. Cote, A. P.; Benin, A. I.; Ockwig, N. W.; O'Keeffe, M.; Matzger, A. J.; Yaghi, O. M., Porous, crystalline, covalent organic frameworks. *Science* **2005**, *310*, 1166-1170.

25. Das, S.; Heasman, P.; Ben, T.; Qiu, S. L., Porous Organic Materials: Strategic Design and Structure-Function Correlation. *Chem. Rev.* **2017**, *117*, 1515-1563.

26. Yi, M.; Shen, Z., A review on mechanical exfoliation for the scalable production of graphene. *J. Mater. Chem. A* **2015**, *3*, 11700-11715.

27. Lu, X. K.; Yu, M. F.; Huang, H.; Ruoff, R. S., Tailoring graphite with the goal of achieving single sheets. *Nanotechnology* **1999**, *10*, 269-272.

28. Novoselov, K. S.; Jiang, D.; Schedin, F.; Booth, T. J.; Khotkevich, V. V.; Morozov, S. V.; Geim, A. K., Two-dimensional atomic crystals. *Proc. Natl. Acad. Sci. U. S. A.* **2005**, *102*, 10451-10453.

29. Suslick, K. S., SONOCHEMISTRY. *Science* **1990**, *247*, 1439-1445.

30. Ciesielski, A.; Samori, P., Graphene via sonication assisted liquid-phase exfoliation. *Chem. Soc. Rev.* **2014**, *43*, 381-398.

31. Hernandez, Y.; Nicolosi, V.; Lotya, M.; Blighe, F. M.; Sun, Z. Y.; De, S.; McGovern, I. T.; Holland, B.; Byrne, M.; Gun'ko, Y. K., et al., High-yield production of graphene by liquid-phase exfoliation of graphite. *Nat. Nanotechnol.* **2008**, *3*, 563-568.

32. Coleman, J. N., Liquid Exfoliation of Defect-Free Graphene. *Acc. Chem. Res.* **2013**, *46*, 14-22.

33. Coleman, J. N.; Lotya, M.; O'Neill, A.; Bergin, S. D.; King, P. J.; Khan, U.; Young, K.; Gaucher, A.; De, S.; Smith, R. J., et al., Two-Dimensional Nanosheets Produced by Liquid Exfoliation of Layered Materials. *Science* **2011**, *331*, 568-571.

34. Nicolosi, V.; Chhowalla, M.; Kanatzidis, M. G.; Strano, M. S.; Coleman, J. N., Liquid Exfoliation of Layered Materials. *Science* **2013**, *340*, 1420-+.

35. Hummers, W. S.; Offeman, R. E., PREPARATION OF GRAPHITIC OXIDE. *J. Am. Chem. Soc.*

1958, *80*, 1339-1339.

36. Stankovich, S.; Dikin, D. A.; Piner, R. D.; Kohlhaas, K. A.; Kleinhammes, A.; Jia, Y.; Wu, Y.; Nguyen, S. T.; Ruoff, R. S., Synthesis of graphene-based nanosheets via chemical reduction of exfoliated graphite oxide. *Carbon* **2007**, *45*, 1558-1565.

37. Dimiev, A. M.; Tour, J. M., Mechanism of Graphene Oxide Formation. *ACS Nano* **2014**, *8*, 3060-3068.

38. Compton, O. C.; Nguyen, S. T., Graphene Oxide, Highly Reduced Graphene Oxide, and Graphene: Versatile Building Blocks for Carbon-Based Materials. *Small* **2010**, *6*, 711-723.

39. Li, X. S.; Cai, W. W.; An, J. H.; Kim, S.; Nah, J.; Yang, D. X.; Piner, R.; Velamakanni, A.; Jung, I.; Tutuc, E., et al., Large-Area Synthesis of High-Quality and Uniform Graphene Films on Copper Foils. *Science* **2009**, *324*, 1312-1314.

40. Zhang, Y.; Zhang, L. Y.; Zhou, C. W., Review of Chemical Vapor Deposition of Graphene and Related Applications. *Acc. Chem. Res.* **2013**, *46*, 2329-2339.

41. Liu, K. K.; Zhang, W. J.; Lee, Y. H.; Lin, Y. C.; Chang, M. T.; Su, C.; Chang, C. S.; Li, H.; Shi, Y. M.; Zhang, H., et al., Growth of Large-Area and Highly Crystalline MoS2 Thin Layers on Insulating Substrates. *Nano Lett.* **2012**, *12*, 1538-1544.

42. Lee, Y. H.; Zhang, X. Q.; Zhang, W. J.; Chang, M. T.; Lin, C. T.; Chang, K. D.; Yu, Y. C.; Wang, J. T. W.; Chang, C. S.; Li, L. J., et al., Synthesis of Large-Area MoS2 Atomic Layers with Chemical Vapor Deposition. *Adv. Mater.* **2012**, *24*, 2320-2325.

43. McCreary, K. M.; Hanbicki, A. T.; Robinson, J. T.; Cobas, E.; Culbertson, J. C.; Friedman, A. L.; Jernigan, G. G.; Jonker, B. T., Large-Area Synthesis of Continuous and Uniform MoS2 Monolayer Films on Graphene. *Adv. Funct. Mater.* **2014**, *24*, 6449-6454.

44. Tan, C. L.; Zhang, H., Wet-chemical synthesis and applications of non-layer structured two-dimensional nanomaterials. *Nat. Commun.* **2015**, *6*.

45. Gersten, B., Solvothermal synthesis of nanoparticles. *Chemfiles* **2005**, *5*, 11-12.

46. Xie, J. F.; Zhang, H.; Li, S.; Wang, R. X.; Sun, X.; Zhou, M.; Zhou, J. F.; Lou, X. W.; Xie, Y., Defect-Rich MoS2 Ultrathin Nanosheets with Additional Active Edge Sites for Enhanced Electrocatalytic Hydrogen Evolution. *Adv. Mater.* **2013**, *25*, 5807-5813.

47. Wang, Y. W.; He, J. T.; Liu, C. C.; Chong, W. H.; Chen, H. Y., Thermodynamics versus Kinetics in Nanosynthesis. *Angew. Chem. Int. Ed.* **2015**, *54*, 2022-2051.

48. Colson, J. W.; Dichtel, W. R., Rationally synthesized two-dimensional polymers. *Nat. Chem.* **2013**, *5*, 453-465.

49. Zhu, L. J.; Zhang, Y. B., Crystallization of Covalent Organic Frameworks for Gas Storage Applications. *Molecules* **2017**, *22*.

50. Piradashvili, K.; Alexandrino, E. M.; Wurm, F. R.; Landfester, K., Reactions and Polymerizations at the Liquid-Liquid Interface. *Chem. Rev.* **2016**, *116*, 2141-2169.

51. Kambe, T.; Sakamoto, R.; Hoshiko, K.; Takada, K.; Miyachi, M.; Ryu, J. H.; Sasaki, S.; Kim, J.; Nakazato, K.; Takata, M., et al., pi-Conjugated Nickel Bis(dithiolene) Complex Nanosheet. *J. Am. Chem. Soc.* **2013**, *135*, 2462-2465.

52. Kambe, T.; Sakamoto, R.; Kusamoto, T.; Pal, T.; Fukui, N.; Hoshiko, K.; Shimojima, T.; Wang, Z. F.; Hirahara, T.; Ishizaka, K., et al., Redox Control and High Conductivity of Nickel Bis(dithiolene) Complex pi-Nanosheet: A Potential Organic Two-Dimensional Topological Insulator. *J. Am. Chem. Soc.* **2014**, *136*, 14357-14360.

53. Huang, X.; Sheng, P.; Tu, Z. Y.; Zhang, F. J.; Wang, J. H.; Geng, H.; Zou, Y.; Di, C. A.; Yi, Y. P.; Sun, Y. M., et al., A two-dimensional pi-d conjugated coordination polymer with extremely high electrical conductivity and ambipolar transport behaviour. *Nat. Commun.* **2015**, *6*.

54. Matsuoka, R.; Sakamoto, R.; Hoshiko, K.; Sasaki, S.; Masunaga, H.; Nagashio, K.; Nishihara, H., Crystalline Graphdiyne Nanosheets Produced at a Gas/Liquid or Liquid/Liquid Interface. *J. Am. Chem. Soc.* **2017**, *139*, 3145-3152.

55. Dey, K.; Pal, M.; Rout, K. C.; Kunjattu H, S.; Das, A.; Mukherjee, R.; Kharul, U. K.; Banerjee, R., Selective Molecular Separation by Interfacially Crystallized Covalent Organic Framework Thin Films. *J. Am. Chem. Soc.* **2017**, *139*, 13083-13091.

56. Kissel, P.; Murray, D. J.; Wulftange, W. J.; Catalano, V. J.; King, B. T., A nanoporous two-dimensional polymer by single-crystal-to-single-crystal photopolymerization. *Nat. Chem.* **2014**, *6*, 774-778.

57. Bhola, R.; Payamyar, P.; Murray, D. J.; Kumar, B.; Teator, A. J.; Schmidt, M. U.; Hammer, S. M.; Saha, A.; Sakamoto, J.; Schluter, A. D., et al., A Two-Dimensional Polymer from the Anthracene Dimer and Triptycene Motifs. *J. Am. Chem. Soc.* **2013**, *135*, 14134-14141.

58. Kissel, P.; Erni, R.; Schweizer, W. B.; Rossell, M. D.; King, B. T.; Bauer, T.; Gotzinger, S.; Schluter, A. D.; Sakamoto, J., A two-dimensional polymer prepared by organic synthesis. *Nat. Chem.* **2012**, *4*, 287-291.

59. Kory, M. J.; Worle, M.; Weber, T.; Payamyar, P.; van de Poll, S. W.; Dshemuchadse, J.; Trapp, N.; Schluter, A. D., Gram-scale synthesis of two-dimensional polymer crystals and their structure analysis by X-ray diffraction. *Nat. Chem.* **2014**, *6*, 779-784.

60. Bekyarova, E.; Sarkar, S.; Wang, F. H.; Itkis, M. E.; Kalinina, I.; Tian, X. J.; Haddon, R. C., Effect of Covalent Chemistry on the Electronic Structure and Properties of Carbon Nanotubes and Graphene. *Acc. Chem. Res.* **2013**, *46*, 65-76.

61. Sarkar, S.; Bekyarova, E.; Haddon, R. C., Chemistry at the Dirac Point: Diels-Alder Reactivity of Graphene. *Acc. Chem. Res.* **2012**, *45*, 673-682.

62. Khayum, M. A.; Kandambeth, S.; Mitra, S.; Nair, S. B.; Das, A.; Nagane, S. S.; Mukherjee, R.; Banerjee, R., Chemically Delaminated Free-Standing Ultrathin Covalent Organic Nanosheets. *Angew. Chem. Int. Ed.* **2016**, *55*, 15604-15608.

63. Gao, J.; Li, B. C.; Tan, J. W.; Chow, P.; Lu, T. M.; Koratkar, N., Aging of Transition Metal Dichalcogenide Monolayers. *ACS Nano* **2016**, *10*, 2628-2635.

64. Waller, P. J.; Lyle, S. J.; Popp, T. M. O.; Diercks, C. S.; Reimer, J. A.; Yaghi, O. M., Chemical Conversion of Linkages in Covalent Organic Frameworks. *J. Am. Chem. Soc.* **2016**, *138*, 15519-15522.

65. Iijima, S., HELICAL MICROTUBULES OF GRAPHITIC CARBON. *Nature* **1991**, *354*, 56-58.

66. Hersam, M. C., The Reemergence of Chemistry for Post-Graphene Two-Dimensional Nanomaterials. *ACS Nano* **2015**, *9*, 4661-4663.

67. Hirsch, A., Functionalization of single-walled carbon nanotubes. *Angew. Chem. Int. Ed.* **2002**, *41*, 1853-1859.

68. Hirsch, A.; Englert, J. M.; Hauke, F., Wet Chemical Functionalization of Graphene. *Acc. Chem. Res.* **2013**, *46*, 87-96.

69. Bahr, J. L.; Yang, J. P.; Kosynkin, D. V.; Bronikowski, M. J.; Smalley, R. E.; Tour, J. M., Functionalization of carbon nanotubes by electrochemical reduction of aryl diazonium salts: A bucky paper electrode. *J. Am. Chem. Soc.* **2001**, *123*, 6536-6542.

70. Sinitskii, A.; Dimiev, A.; Corley, D. A.; Fursina, A. A.; Kosynkin, D. V.; Tour, J. M., Kinetics of Diazonium Functionalization of Chemically Converted Graphene Nanoribbons. *ACS Nano* **2010**, *4*, 1949-1954.

71. Georgakilas, V.; Kordatos, K.; Prato, M.; Guldi, D. M.; Holzinger, M.; Hirsch, A., Organic functionalization of carbon nanotubes. *J. Am. Chem. Soc.* **2002**, *124*, 760-761.

72. Georgakilas, V.; Bourlinos, A. B.; Zboril, R.; Steriotis, T. A.; Dallas, P.; Stubos, A. K.; Trapalis, C., Organic functionalisation of graphenes. *Chem. Commun.* **2010**, *46*, 1766-1768.

73. Kim, K. S.; Bae, D. J.; Kim, J. R.; Park, K. A.; Lim, S. C.; Kim, J. J.; Choi, W. B.; Park, C. Y.; Lee, Y. H., Modification of electronic structures of a carbon nanotube by hydrogen functionalization. *Adv. Mater.* **2002**, *14*, 1818-1821.

74. Ryu, S.; Han, M. Y.; Maultzsch, J.; Heinz, T. F.; Kim, P.; Steigerwald, M. L.; Brus, L. E., Reversible Basal Plane Hydrogenation of Graphene. *Nano Lett.* **2008**, *8*, 4597-4602.

75. Mickelson, E. T.; Huffman, C. B.; Rinzler, A. G.; Smalley, R. E.; Hauge, R. H.; Margrave, J. L., Fluorination of single-wall carbon nanotubes. *Chem. Phys. Lett.* **1998**, *296*, 188-194.

76. Robinson, J. T.; Burgess, J. S.; Junkermeier, C. E.; Badescu, S. C.; Reinecke, T. L.; Perkins, F. K.; Zalalutdniov, M. K.; Baldwin, J. W.; Culbertson, J. C.; Sheehan, P. E., et al., Properties of Fluorinated Graphene Films. *Nano Lett.* **2010**, *10*, 3001-3005.

77. Krueger, A., Carbon Nanotubes. In *Carbon Materials and Nanotechnology*, Wiley-VCH Verlag GmbH & Co. KGaA: 2010; pp 123-281.

78. Krueger, A., Fullerenes – Cages Made from Carbon. In *Carbon Materials and Nanotechnology*, Wiley-VCH Verlag GmbH & Co. KGaA: 2010; pp 33-122.

79. Sarkar, S.; Bekyarova, E.; Niyogi, S.; Haddon, R. C., Diels-Alder Chemistry of Graphite and

Graphene: Graphene as Diene and Dienophile. *J. Am. Chem. Soc.* **2011**, *133*, 3324-3327.

80. Murata, Y.; Kato, N.; Fujiwara, K.; Komatsu, K., Solid-state 4+2 cycloaddition of fullerene C-60 with condensed aromatics using a high-speed vibration milling technique. *J. Org. Chem.* **1999**, *64*, 3483-3488.

81. Stolle, A.; Szuppa, T.; Leonhardt, S. E. S.; Ondruschka, B., Ball milling in organic synthesis: solutions and challenges. *Chem. Soc. Rev.* **2011**, *40*, 2317-2329.

82. Jeon, I. Y.; Shin, Y. R.; Sohn, G. J.; Choi, H. J.; Bae, S. Y.; Mahmood, J.; Jung, S. M.; Seo, J. M.; Kim, M. J.; Chang, D. W., et al., Edge-carboxylated graphene nanosheets via ball milling. *Proc. Natl. Acad. Sci. U. S. A.* **2012**, *109*, 5588-5593.

83. Jeon, I. Y.; Choi, H. J.; Jung, S. M.; Seo, J. M.; Kim, M. J.; Dai, L. M.; Baek, J. B., Large-Scale Production of Edge-Selectively Functionalized Graphene Nanoplatelets via Ball Milling and Their Use as Metal-Free Electrocatalysts for Oxygen Reduction Reaction. *J. Am. Chem. Soc.* **2013**, *135*, 1386-1393.

84. Clar, E.; Zander, M., 927. Syntheses of coronene and 1 : 2-7 : 8-dibenzocoronene. *J. Chem. Soc.* **1957**, *0*, 4616-4619.

85. Khan, M. N., KINETICS AND MECHANISM OF THE ALKALINE-HYDROLYSIS OF MALEIMIDE. *J. Pharm. Sci.* **1984**, *73*, 1767-1771.

86. Kwart, H.; Burchuk, I., ISOMERISM AND ADDUCT STABILITY IN THE DIELS ALDER REACTION .1. THE ADDUCTS OF FURAN AND MALEIMIDE. *J. Am. Chem. Soc.* **1952**, *74*, 3094-3097.

87. Schneider, B.; Hennemann, O. D.; Possart, W., The adhesion of maleic anhydride on native aluminum oxide: An approach by infrared spectroscopy and quantum mechanical modeling. *J. Adhes.* **2002**, *78*, 779-797.

88. Ulbricht, H.; Moos, G.; Hertel, T., Physisorption of molecular oxygen on single-wall carbon nanotube bundles and graphite. *Phys. Rev. B* **2002**, *66*.

89. Giannozzi, P.; Car, R.; Scoles, G., Oxygen adsorption on graphite and nanotubes. *J. Chem. Phys.* **2003**, *118*, 1003-1006.

90. Wang, Y.; Shao, Y. Y.; Matson, D. W.; Li, J. H.; Lin, Y. H., Nitrogen-Doped Graphene and Its Application in Electrochemical Biosensing. *ACS Nano* **2010**, *4*, 1790-1798.

91. Sheng, Z. H.; Shao, L.; Chen, J. J.; Bao, W. J.; Wang, F. B.; Xia, X. H., Catalyst-Free Synthesis of Nitrogen-Doped Graphene via Thermal Annealing Graphite Oxide with Melamine and Its Excellent Electrocatalysis. *ACS Nano* **2011**, *5*, 4350-4358.

92. Ferrari, A. C., Raman spectroscopy of graphene and graphite: Disorder, electron-phonon coupling, doping and nonadiabatic effects. *Solid State Commun.* **2007**, *143*, 47-57.

93. Shih, C. J.; Vijayaraghavan, A.; Krishnan, R.; Sharma, R.; Han, J. H.; Ham, M. H.; Jin, Z.; Lin, S. C.; Paulus, G. L. C.; Reuel, N. F., et al., Bi- and trilayer graphene solutions. *Nat. Nanotechnol.* **2011**,

6, 439-445.

94. Sun, Y.-P.; Fu, K. F.; Lin, Y.; Huang, W. J., Functionalized carbon nanotubes: Properties and applications. *Acc. Chem. Res.* **2002**, *35*, 1096-1104.

95. Vázquez, E.; Giacalone, F.; Prato, M., Non-conventional methods and media for the activation and manipulation of carbon nanoforms. *Chem. Soc. Rev.* **2014**, *43*, 58-69.

96. Datsyuk, V.; Kalyva, M.; Papagelis, K.; Parthenios, J.; Tasis, D.; Siokou, A.; Kallitsis, I.; Galiotis, C., Chemical oxidation of multiwalled carbon nanotubes. *Carbon* **2008**, *46*, 833-840.

97. Strano, M. S.; Dyke, C. A.; Usrey, M. L.; Barone, P. W.; Allen, M. J.; Shan, H. W.; Kittrell, C.; Hauge, R. H.; Tour, J. M.; Smalley, R. E., Electronic structure control of single-walled carbon nanotube functionalization. *Science* **2003**, *301*, 1519-1522.

98. Bekyarova, E.; Itkis, M. E.; Ramesh, P.; Berger, C.; Sprinkle, M.; de Heer, W. A.; Haddon, R. C., Chemical Modification of Epitaxial Graphene: Spontaneous Grafting of Aryl Groups. *J. Am. Chem. Soc.* **2009**, *131*, 1336-1337.

99. Nicolaou, K. C.; Snyder, S. A.; Montagnon, T.; Vassilikogiannakis, G., The Diels-Alder reaction in total synthesis. *Angew. Chem. Int. Ed.* **2002**, *41*, 1668-1698.

100. Hirsch, A.; Brettreich, M., Cycloadditions. In *Fullerenes: Chemistry and Reactions*, Wiley-VCH Verlag GmbH & Co. KGaA: Weinheim, FRG, 2005; pp 101-183.

101. Tasis, D.; Tagmatarchis, N.; Bianco, A.; Prato, M., Chemistry of carbon nanotubes. *Chem. Rev.* **2006**, *106*, 1105-1136.

102. Cao, Y.; Osuna, S.; Liang, Y.; Haddon, R. C.; Houk, K. N., Diels-Alder Reactions of Graphene: Computational Predictions of Products and Sites of Reaction. *J. Am. Chem. Soc.* **2013**, *135*, 17643-17649.

103. Denis, P. A., Organic Chemistry of Graphene: The Diels-Alder Reaction. *Chem. Eur. J.* **2013**, *19*, 15719-15725.

104. Pollet, P.; Davey, E. A.; Ureña-Benavides, E. E.; Eckert, C. A.; Liotta, C. L., Solvents for sustainable chemical processes. *Green Chem.* **2014**, *16*, 1034-1055.

105. Dyke, C. A.; Tour, J. M., Solvent-free functionalization of carbon nanotubes. *J. Am. Chem. Soc.* **2003**, *125*, 1156-1157.

106. Basiuk, E. V.; Monroy-Peláez, M.; Puente-Lee, I.; Basiuk, V. A., Direct solvent-free amination of closed-cap carbon nanotubes: A link to fullerene chemistry. *Nano Lett.* **2004**, *4*, 863-866.

107. Seo, J.-M.; Jeon, I.-Y.; Baek, J.-B., Mechanochemically driven solid-state Diels-Alder reaction of graphite into graphene nanoplatelets. *Chem. Sci.* **2013**, *4*, 4273-4277.

108. Hontoria-Lucas, C.; López-Peinado, A. J.; López-González, J. D. D.; Rojas-Cervantes, M. L.; Martín-Aranda, R. M., STUDY OF OXYGEN-CONTAINING GROUPS IN A SERIES OF GRAPHITE OXIDES - PHYSICAL AND CHEMICAL CHARACTERIZATION. *Carbon* **1995**, *33*, 1585-1592.

109. Gaboury, S. R.; Urban, M. W., MICROWAVE PLASMA REACTIONS OF SOLID MONOMERS WITH SILICONE ELASTOMER SURFACES - A SPECTROSCOPIC STUDY. *Langmuir* **1993**, *9*, 3225-3233.

110. Yung, K. C.; Zeng, D. W.; Yue, T. M., XPS investigation of Upilex-S polyimide ablated by 355 nm Nd : YAG laser irradiation. *Appl. Surf. Sci.* **2001**, *173*, 193-202.

111. Du, Y.; Mao, K. M.; Kamakoti, P.; Ravikovitch, P.; Paur, C.; Cundy, S.; Li, Q. C.; Calabro, D., Experimental and computational studies of pyridine-assisted post-synthesis modified air stable covalent-organic frameworks. *Chem. Commun.* **2012**, *48*, 4606-4608.

112. Lanni, L. M.; Tilford, R. W.; Bharathy, M.; Lavigne, J. J., Enhanced Hydrolytic Stability of Self-Assembling Alkylated Two-Dimensional Covalent Organic Frameworks. *J. Am. Chem. Soc.* **2011**, *133*, 13975-13983.

113. Segura, J. L.; Mancheno, M. J.; Zamora, F., Covalent organic frameworks based on Schiff-base chemistry: synthesis, properties and potential applications. *Chem. Soc. Rev.* **2016**, *45*, 5635-5671.

114. Straessler, N. A., SYNTHESIS OF TRINITROAROMATICS USING ALTERNATIVE MIXED ACID NITRATION CONDITIONS. *Synth. Commun.* **2010**, *40*, 2513-2519.

115. Quadbeck, G.; Rohm, E., ZUR SYNTHESE VON AMINOCYCLITEN. *Chem. Ber. Recl.* **1956**, *89*, 1645-1648.

116. McMurry, J., *Organic Chemistry*. 8 ed.; Cengage Learning: USA, 2012; p 1376.

117. Fang, Q. R.; Gu, S.; Zheng, J.; Zhuang, Z. B.; Qiu, S. L.; Yan, Y. S., 3D Microporous Base-Functionalized Covalent Organic Frameworks for Size-Selective Catalysis. *Angew. Chem. Int. Ed.* **2014**, *53*, 2878-2882.

118. Fang, J. H.; Kita, H.; Okamoto, K., Hyperbranched polyimides for gas separation applications. 1. Synthesis and characterization. *Macromolecules* **2000**, *33*, 4639-4646.

119. Fang, Q. R.; Zhuang, Z. B.; Gu, S.; Kaspar, R. B.; Zheng, J.; Wang, J. H.; Qiu, S. L.; Yan, Y. S., Designed synthesis of large-pore crystalline polyimide covalent organic frameworks. *Nat. Commun.* **2014**, *5*.

120. Fang, Q. R.; Wang, J. H.; Gu, S.; Kaspar, R. B.; Zhuang, Z. B.; Zheng, J.; Guo, H. X.; Qiu, S. L.; Yan, Y. S., 3D Porous Crystalline Polyimide Covalent Organic Frameworks for Drug Delivery. *J. Am. Chem. Soc.* **2015**, *137*, 8352-8355.

121. Wang, Z. G.; Zhang, B. F.; Yu, H.; Sun, L. X.; Jiao, C. L.; Liu, W. S., Microporous polyimide networks with large surface areas and their hydrogen storage properties. *Chem. Commun.* **2010**, *46*, 7730-7732.

122. Luo, Y. L.; Li, B. Y.; Liang, L. Y.; Tan, B. E., Synthesis of cost-effective porous polyimides and their gas storage properties. *Chem. Commun.* **2011**, *47*, 7704-7706.

123. Tian, D.; Zhang, H. Z.; Zhang, D. S.; Chang, Z.; Han, J.; Gao, X. P.; Bu, X. H., Li-ion storage and gas adsorption properties of porous polyimides (PIs). *RSC Adv.* **2014**, *4*, 7506-7510.

124. Thomaides, J.; Maslak, P.; Breslow, R., ELECTRON-RICH HEXASUBSTITUTED BENZENE-DERIVATIVES AND THEIR OXIDIZED CATION RADICALS, DICATIONS WITH POTENTIAL TRIPLET GROUND-STATES, AND POLYCATIONS. *J. Am. Chem. Soc.* **1988**, *110*, 3970-3979.

125. Grandolini, G.; Martani, A., Trirodanazione della m-fenilendiammina e del triamminobenzolo simmetrico. Sintesi di derivati tiazolici e chetotiazinici dalla diammino- e triamminotritiofloroglucina. *Gazz. Chim. Ital.* **1962**, *92*, 1150-1167.

126. Gill, J. E.; Macgillivray, R.; Munro, J., THE PREPARATION OF SYMMETRICAL AROMATIC TRIAMINES AND TRIISOCYANATES. *J. Chem. Soc.* **1949**, 1753-1754.

127. Thottempudi, V.; Forohor, F.; Parrish, D. A.; Shreeve, J. M., Tris(triazolo)benzene and Its Derivatives: High-Density Energetic Materials. *Angew. Chem. Int. Ed.* **2012**, *51*, 9881-9885.

128. Lothrop, W. C.; Handrick, G. R.; Hainer, R. M., THE STRUCTURE AND INFRARED ABSORPTION SPECTRA OF POLYNITROPHENYLMETHYLNITRAMINES AND POLYNITROANILINES. *J. Am. Chem. Soc.* **1951**, *73*, 3581-3584.

129. Kimura, K., SYNTHESIS AND CHARACTERIZATION OF NOVEL POLY(BENZOBISTHIAZOLE-IMIDE)S. *J. Polym. Sci. Pol. Chem.* **1994**, *32*, 181-185.

130. Ratta, V. Crystallization, morphology, thermal stability and adhesive properties of novel high performance semicrystalline polyimides. Doctoral thesis, Virginia Polytechnic Institute and State University USA, 1999.

Acknowledgement

2011년, 학부를 졸업하고 대학원을 진학한 뒤 기나긴 시간 끝에 박사 학위의 여정을 마치게 되었습니다. 부족한 저에게 연구 방향을 지도해주시고 진로에 대해 진심어린 조언을 해주신 백종범 지도 교수님께 가장 먼저 감사의 말씀을 드립니다. 치열하게 연구하는 사람들 속에서 끊임없는 관심과 지도 덕에 동기부여를 받으며 고난과 역경들을 잘 넘겨온 것 같습니다. 그리고 결정 분석에 도움을 주신 나명수 교수님, 바쁘신 시간에도 불구하고 박사학위 심사를 맡아주신 박노정 교수님, 유정우 교수님, 정후영 교수님께 감사의 말씀 전합니다.

7년 동안 저와 함께 같이 지냈던 CDCOF 멤버들, 내 곁에서 든든히 버팀목이 되어 준 고마운 선민이, 학부생 때부터 훈훈함을 잃지 않고 연구하고 있는 석진이, 실험실 구성원을 위해 항상 희생해온 랩장 윤광씨, 밝은 모습으로 묵묵히 연구를 수행하는 수영이, 언제나 웃으며 자기 일에 최선을 다하는 선희, 실험실의 재간둥이 혁준이, 자유로운 영혼 성욱이, 사랑꾼 도형이, 박학다식 종필이, 108동을 든든히 관리하고 있는 부재씨, 앞으로 우리 실험실에서 연구를 수행하게 될 영현이, it was honor to work with Javeed, Ishfaq, Feng and Gaofeng! 그리고 우리 모두가 쾌차하시길 바라는 주명종 교수님께도 감사의 말씀을 드립니다.

끝으로 지금까지 믿고 기다려주신 부모님과 제 동생 민경이, 개차반 친구들에게 그 동안 잘 보살펴줘서 든든했다고 이 글로 전하고 싶습니다.

사전에 나온 박사의 정의는 학문 연구와 학술 진흥을 위하여 일정한 능력을 갖춘 자 또는 업적이 있는 자에 대해 수여하는 최고의 학위라고 합니다. 제가 감히 이 학위를 받을 자격이 있는지 두렵기도 했고 부족한 점이 많았지만, 이제 당당히 박사로서 그동안 쌓아온 지식과 조언들을 토대로 좋은 연구 성과를 내며 감사를 표하도록 하겠습니다.

Publications

Representative papers

1. Seo, J.-M.; Jeon, I.-Y.; Baek, J.-B., Mechanochemically driven solid-state Diels-Alder reaction of graphite into graphene nanoplatelets. *Chem. Sci.* **2013**, *4*, 4273-4277.

2. Seo, J.-M.; Baek, J.-B., A solvent-free Diels-Alder reaction of graphite into functionalized graphene nanosheets. *Chem. Commun.* **2014**, *50*, 14651-14653.

3. Seo, J. M.; Tan, L. S.; Baek, J. B., Defect/Edge-Selective Functionalization of Carbon Materials by "Direct" Friedel-Crafts Acylation Reaction. *Adv. Mater.* **2017**, *29*, 1606327.

Other papers

1. Jeon, I.-Y.; Shin, Y.-R.; Sohn, G.-J.; Choi, H.-J.; Bae, S.-Y.; Mahmood, J.; Jung, S.-M.; Seo, J.-M.; Kim, M.-J.; Chang, D. W.; Dai, L.; Baek, J.-B., Edge-carboxylated graphene nanosheets via ball milling. *Proc. Natl. Acad. Sci. U. S. A.* **2012**, *109*, 5588-5593.

2. Choi, H.-J.; Jung, S.-M.; Seo, J.-M.; Chang, D. W.; Dai, L.; Baek, J.-B., Graphene for energy conversion and storage in fuel cells and supercapacitors. *Nano Energy* **2012**, *1*, 534-551.

3. Jeon, I.-Y.; Choi, H.-J.; Jung, S.-M.; Seo, J.-M.; Kim, M.-J.; Dai, L.; Baek, J.-B., Large-Scale Production of Edge-Selectively Functionalized Graphene Nanoplatelets via Ball Milling and Their Use as Metal-Free Electrocatalysts for Oxygen Reduction Reaction. *J. Am. Chem. Soc.* **2013**, *135*, 1386-1393.

4. Jeon, I.-Y.; Choi, H.-J.; Choi, M.; Seo, J.-M.; Jung, S.-M.; Kim, M.-J.; Zhang, S.; Zhang, L.; Xia, Z.; Dai, L.; Park, N.; Baek, J.-B., Facile, scalable synthesis of edge-halogenated graphene nanoplatelets as efficient metal-free eletrocatalysts for oxygen reduction reaction. *Sci. Rep.* **2013**, *3*.

5. Jeon, I.-Y.; Choi, H.-J.; Ju, M. J.; Choi, I. T.; Lim, K.; Ko, J.; Kim, H. K.; Kim, J. C.; Lee, J.-J.; Shin, D.; Jung, S.-M.; Seo, J.-M.; Kim, M.-J.; Park, N.; Dai, L.; Baek, J.-B., Direct nitrogen fixation at the edges of graphene nanoplatelets as efficient electrocatalysts for energy conversion. *Sci. Rep.* **2013**, *3*.

6. Jeon, I.-Y.; Zhang, S.; Zhang, L.; Choi, H.-J.; Seo, J.-M.; Xia, Z.; Dai, L.; Baek, J.-B., Edge-Selectively Sulfurized Graphene Nanoplatelets as Efficient Metal-Free Electrocatalysts for Oxygen Reduction Reaction: The Electron Spin Effect. *Adv. Mater.* **2013**, *25*, 6138-6145.

7. Jung, S.-M.; Lee, E. K.; Choi, M.; Shin, D.; Jeon, I.-Y.; Seo, J.-M.; Jeong, H. Y.; Park, N.; Oh, J. H.; Baek, J.-B., Direct Solvothermal Synthesis of B/N-Doped Graphene. *Angew. Chem. Int. Ed.* **2014**, *53*, 2398-2401.

8. Kim, M.-J.; Jean, I.-Y.; Seo, J.-M.; Dai, L.; Baek, J.-B., Graphene Phosphonic Acid as an Efficient Flame Retardant. *ACS Nano* **2014**, *8*, 2820-2825.

9. Filer, A.; Choi, H.-J.; Seo, J.-M.; Baek, J.-B., Two and three dimensional network polymers for electrocatalysis. *Phys. Chem. Chem. Phys.* **2014**, *16*, 11150-11161.

10. Chang, D. W.; Choi, H.-J.; Jeon, I.-Y.; Seo, J.-M.; Dai, L.; Baek, J.-B., Solvent-free mechanochemical reduction of graphene oxide. *Carbon* **2014**, *77*, 501-507.

11. Xu, J.; Shui, J.; Wang, J.; Wang, M.; Liu, H.-K.; Dou, S. X.; Jeon, I.-Y.; Seo, J.-M.; Baek, J.-B.; Dai, L., Sulfur-Graphene Nanostructured Cathodes via Ball-Milling for High-Performance Lithium Sulfur Batteries. *ACS Nano* **2014**, *8*, 10920-10930.

12. Xu, J.; Jeon, I.-Y.; Seo, J.-M.; Dou, S.; Dai, L.; Baek, J.-B., Edge-Selectively Halogenated Graphene Nanoplatelets (XGnPs, X = Cl, Br, or I) Prepared by Ball-Milling and Used as Anode Materials for Lithium-Ion Batteries. *Adv. Mater.* **2014**, *26*, 7317-7323.

13. Jeon, I.-Y.; Ju, M. J.; Xu, J.; Choi, H.-J.; Seo, J.-M.; Kim, M.-J.; Choi, I. T.; Kim, H. M.; Kim, J. C.; Lee, J.-J.; Liu, H.-K.; Kim, H. K.; Dou, S.; Dai, L.; Baek, J.-B., Edge-Fluorinated Graphene Nanoplatelets as High Performance Electrodes for Dye-Sensitized Solar Cells and Lithium Ion Batteries. *Adv. Funct. Mater.* **2015**, *25*, 1170-1179.

14. Mahmood, J.; Lee, E. K.; Jung, M.; Shin, D.; Jeon, I.-Y.; Jung, S.-M.; Choi, H.-J.; Seo, J.-M.; Bae, S.-Y.; Sohn, S.-D.; Park, N.; Oh, J. H.; Shin, H.-J.; Baek, J.-B., Nitrogenated holey two-dimensional structures. *Nat. Commun.* **2015**, *6*.

15. Jeon, I.-Y.; Choi, M.; Choi, H.-J.; Jung, S.-M.; Kim, M.-J.; Seo, J.-M.; Bae, S.-Y.; Yoo, S.; Kim, G.; Jeong, H. Y.; Park, N.; Baek, J.-B., Antimony-doped graphene nanoplatelets. *Nat. Commun.* **2015**, *6*.

16. Jeon, I.-Y.; Bae, S.-Y.; Seo, J.-M.; Baek, J.-B., Scalable Production of Edge-Functionalized Graphene Nanoplatelets via Mechanochemical Ball-Milling. *Adv. Funct. Mater.* **2015**, *25*, 6961-6975.

17. Jeon, I. Y.; Kim, H. M.; Kweon, D. H.; Jung, S. M.; Seo, J. M.; Shin, S. H.; Choi, I. T.; Eom, Y. K.; Kang, S. H.; Kim, H. K.; Ju, M. J.; Baek, J. B., Metalloid tellurium-doped graphene nanoplatelets as ultimately stable electrocatalysts for cobalt reduction reaction in dye-sensitized solar cells. *Nano Energy* **2016**, *30*, 867-876.

18. Xu, J. T.; Jeon, I. Y.; Ma, J. M.; Dou, Y. H.; Kim, S. J.; Seo, J. M.; Liu, H. K.; Dou, S. X.; Baek, J. B.; Dai, L. M., Understanding of the capacity contribution of carbon in phosphorus-carbon composites for high-performance anodes in lithium ion batteries. *Nano Res.* **2017**, *10*, 1268-1281.

19. Zhao, X. L.; Li, F.; Wang, R. N.; Seo, J. M.; Choi, H. J.; Jung, S. M.; Mahmood, J.; Jeon, I. Y.; Baek, J. B., Controlled Fabrication of Hierarchically Structured Nitrogen-Doped Carbon Nanotubes as a Highly Active Bifunctional Oxygen Electrocatalyst. *Adv. Funct. Mater.* **2017**, *27*, 1605717.

Proceedings

1. Seo, J.-M.; Baek, J.-B., A solvent-free Diels–Alder reaction of graphite into functionalized graphene nanoplatelets. *IUPAC 2015*, Busan, Korea, **2015**. (Poster presentation)

2. Seo, J.-M.; Baek, J.-B., Solvent-free reaction of graphene nanosheets: [4+2] cycloaddition, *252nd ACS National Meeting & Exposition*, Philadelphia, USA, **2016**. (Oral presentation)

3. Seo, J.-M.; Mahmood, J.; Lee, E. K.; Jung, M.; Shin, D.; Jeon, I.-Y.; Jung, S.-M.; Choi, H.-J.; Bae, S.-Y.; Sohn, S.-D.; Park, N.; Oh, J. H.; Shin, H.-J.; Baek, J.-B., Nitrogenated Two-dimensional Structure, a Semiconducting Covalent-organic Framework, *PSK 40*, Jeju, Korea, **2016**. (Poster presentation)